

X-ray Thomson scattering in high energy density plasmas

Siegfried H. Glenzer

L-399, Lawrence Livermore National Laboratory, University of California, P.O. Box 808, Livermore, California 94551, USA

Ronald Redmer

Institut für Physik, Universität Rostock, Universitätsplatz 3, D-18051 Rostock, Germany

(Published 1 December 2009)

Accurate x-ray scattering techniques to measure the physical properties of dense plasmas have been developed for applications in high energy density physics. This class of experiments produces short-lived hot dense states of matter with electron densities in the range of solid density and higher where powerful penetrating x-ray sources have become available for probing. Experiments have employed laser-based x-ray sources that provide sufficient photon numbers in narrow bandwidth spectral lines, allowing spectrally resolved x-ray scattering measurements from these plasmas. The backscattering spectrum accesses the noncollective Compton scattering regime which provides accurate diagnostic information on the temperature, density, and ionization state. The forward scattering spectrum has been shown to measure the collective plasmon oscillations. Besides extracting the standard plasma parameters, density and temperature, forward scattering yields new observables such as a direct measure of collisions and quantum effects. Dense matter theory relates scattering spectra with the dielectric function and structure factors that determine the physical properties of matter. Applications to radiation-heated and shock-compressed matter have demonstrated accurate measurements of compression and heating with up to picosecond temporal resolution. The ongoing development of suitable x-ray sources and facilities will enable experiments in a wide range of research areas including inertial confinement fusion, radiation hydrodynamics, material science, or laboratory astrophysics.

DOI: [10.1103/RevModPhys.81.1625](https://doi.org/10.1103/RevModPhys.81.1625)

PACS number(s): 52.25.Os, 52.35.Fp, 52.50.Jm

CONTENTS

I. Introduction	1625	D. Detectors	1650
A. Overview	1625	E. Photometrics	1650
B. Historical development	1627	V. X-ray Thomson Scattering Experiments	1651
C. Physical properties of dense plasmas	1628	A. Isochorically heated matter	1651
D. X-ray scattering regimes	1629	B. Matter heated by supersonic heat waves	1654
E. Sensitivity of scattering spectra to plasma parameters	1629	C. Shock-compressed matter	1655
II. Facilities for X-Ray Thomson Scattering Experiments	1632	D. Coalescing shocks	1657
III. Theory of the Dynamic Structure Factor	1634	VI. Summary and Outlook	1658
A. General expressions	1634	List of Acronyms and Definitions	1659
B. Application to Thomson scattering	1635	Acknowledgments	1659
C. Elastic scattering feature	1637	References	1660
D. Free-electron feature	1637		
1. Two-component screening	1637		
2. Ionic correlations and electronic screening	1638		
E. Bound-free transitions	1638		
F. Numerical results	1639		
1. Collision frequency	1639		
2. Electron feature of the dynamic structure factor	1639		
3. Bound-free spectrum	1641		
4. Ion feature	1641		
G. Theoretical spectra	1642		
IV. Experimental Techniques	1643		
A. Design of scattering experiments	1643		
B. X-ray probe requirements	1645		
C. Spectrometers	1648		

I. INTRODUCTION

A. Overview

Accurate measurements of the plasma conditions including temperature, density, and ionization state in dense plasmas are important for understanding and modeling high energy density physics experiments. For applications in this regime, new scattering techniques have been developed by [Glenzer, Gregori, Lee, *et al.* \(2003\)](#) and [Glenzer, Landen, *et al.* \(2007\)](#) that make use of x rays to penetrate dense or compressed matter. This capability is particularly important for laboratory astrophysics and inertial confinement fusion (ICF) experiments ([Lindl *et al.*, 2004](#); [Remington *et al.*, 2006](#)), and is broadly applicable in the dense plasma community. Examples of important applications include the measurement of compression and heating of shock-compressed

matter and the fundamental characterization of thermodynamic properties including phase transitions (Beule *et al.*, 1999, 2001; Fortov *et al.*, 2007) and new states of matter (Bonev, Schwegler, *et al.*, 2004). Specifically, x-ray scattering is applicable as a tool to resolve fundamental physics questions such as the equation of state of dense matter (Collins *et al.*, 1988; Young and Corey, 1995), structure factors in two-component plasmas (Hansen and McDonald, 2006), limits of the validity of the random phase approximation (RPA) (Pines and Bohm, 1952; Bohm and Pines, 1953), and the role of collisions (Reinholz *et al.*, 2000; Redmer *et al.*, 2005).

The spectrally resolving x-ray scattering technique is now widely applied in many large (Gregori *et al.*, 2004; Gregori, Glenzer, Chung, *et al.*, 2006; Sawada *et al.*, 2007) and medium-size laboratories (Ravasio *et al.*, 2007; Kritcher, Neumayer, Castor, *et al.*, 2008; Garcia Saiz, Gregori, Gericke, *et al.*, 2008) to study dense plasma properties. Accurate and precise data are obtained similar to data from low density plasmas when optical Thomson scattering was first introduced to study plasmas in the 1960s. Powerful x-ray sources (Landen, Farley, *et al.*, 2001; Lee *et al.*, 2003) take the place of optical lasers to penetrate through dense or compressed matter and to access the dense plasma physics regime with electron densities of solid and above. These x-ray sources must fulfill the stringent requirements (Urry *et al.*, 2006) on photon numbers and bandwidth for spectrally resolved x-ray Thomson scattering measurements in single-shot experiments (Landen, Glenzer, *et al.*, 2001).

X-ray Thomson scattering was first demonstrated employing laser-produced He- α x-ray sources to perform scattering measurements in isochorically heated solid-density matter (Glenzer, Gregori, Lee, *et al.*, 2003; Glenzer, Gregori, Rogers, 2003). Measurements in backscatter geometry have accessed the Compton scattering regime where the scattering process is noncollective and the spectrum shows the Compton downshifted line that is broadened by the thermal motion of the electrons. Thus, the inelastic scattering spectrum reflects the electron velocity distribution function, and for a Maxwell-Boltzmann distribution function, yields the electron temperature with high accuracy. For Fermi-degenerate states of matter, on the other hand, the Compton scattering spectrum provides the Fermi energy and thus the electron density. Experiments observing these distributions have been interpreted employing first-principles methods (Pines and Bohm, 1952; Gregori, Glenzer, Rozmus, *et al.*, 2003; Redmer *et al.*, 2005) that includes degeneracy effects and provide the plasma conditions with high accuracy.

In addition to the Compton scattering feature from inelastic scattering by free and weakly bound electrons, the noncollective scattering spectrum shows the unshifted Rayleigh scattering component from elastic scattering by tightly bound electrons. The latter occupy quantum states with ionization energy larger than the Compton energy deep in the Fermi sea that cannot be excited, e.g., due to the Pauli exclusion principle. Thus, the intensity of the elastic scattering feature is propor-

tional to the number of tightly bound electrons as well as the static structure factor. The latter takes into account the dependence on the ion-ion correlations. For the noncollective scattering conditions where the static structure factor approaches 1, the intensity of the elastic scattering feature provides an accurate measure of the ionization state. Absolute calibration is provided by comparing with the inelastic scattering component whose intensity is well known from the sum rules (Kohn and Sham, 1965). For isochorically heated matter where the ion density is known *a priori*, the ionization state inferred from the ratio of the inelastic Compton to the elastic Rayleigh scattering components yields the electron density.

The collective properties of the dense plasmas can be accessed by the proper choice of the scattering angle and x-ray probe energy. In the forward scattering regime, collective plasmon (Langmuir) oscillations (Tonks and Langmuir, 1929) have been observed by Glenzer, Landen, *et al.* (2007). The plasmon frequency shift from the incident x-ray probe energy directly provides the local electron density via the Bohm-Gross (Bohm and Gross, 1949) dispersion relation. Besides well-known thermal corrections, the dispersion relation in dense plasmas includes additional terms for degeneracy and quantum diffraction. Experiments in isochorically heated solid-density plasmas show that the density from downshifted plasmons agrees with the values inferred from noncollective scattering. In addition, forward scattering on plasmons is not dependent on knowledge of the ion density and is thus directly applicable to characterize compressed matter and to determine the optical properties.

Plasmons are affected by Landau damping as well as electron-ion collisions. Thus, a consistent description of the plasmon spectrum describing both the frequency shift and the spectral shape requires a theory beyond the RPA. Experiments have been successfully described with the Mermin approach (Mermin, 1970; Höll *et al.*, 2004; and Thiele *et al.*, 2006) that takes into account the dynamic collision frequency for calculating damping. In cases where collisional damping is not the dominant mechanism, the Born approximation has been shown to be sufficient. In future studies of cold plasmas with small Landau damping, plasmon measurements will provide an experimental test on the theory of collisions yielding conductivity (Röpke, 1998; Redmer *et al.*, 2003; Kuhlbrodt *et al.*, 2005; Höll *et al.*, 2007), which is an important dense plasma property for radiation-hydrodynamic modeling of high energy density physics experiments.

Besides observing plasmons, collective scattering provides information on the structure of dense plasmas. In this regime, the elastic scattering intensity includes additional dependency on the density fluctuations associated with electrons in the screening cloud around the ion. The latter is sensitive to both the ion-ion and electron-ion structure factors, and no simple approximations are applicable. In addition, the interaction is dependent on electron and ion temperatures. Hypernetted chain (HNC) equations with quantum potentials or density-

functional theory (DFT) have been successfully applied to describe experiments (Schwarz *et al.*, 2007; Wünsch *et al.*, 2008), but only few well-characterized conditions exist where the plasma conditions have been determined by noncollective scattering. Ultimately, the study of structure factors in the collective scattering regime will provide the means to determine the thermodynamic properties and the atomic structure in dense plasmas.

The outline of this review is as follows. After a historical review, Sec. I provides an introduction to the properties of dense plasmas and to the scattering regimes and plasma parameters accessible by spectrally resolved x-ray Thomson scattering experiments. Section II describes the facilities with the x-ray and plasma driver capabilities to produce and probe dense plasmas in the high energy density physics regime. A comprehensive theory of the dynamic structure factor of the x-ray Thomson scattering spectrum is given in Sec. III. The experimental techniques and requirements to perform x-ray Thomson scattering measurements are discussed in Sec. IV. Section V describes the proof-of-principle experiments and highlights present state of the art experimental work. A summary is given in Sec. VI that includes an outlook to future experiments and physics issues where the x-ray Thomson scattering measurements will be required to enhance our knowledge of high-energy density plasmas. A list of acronyms and symbols used in this review is also provided.

B. Historical development

Scattering experiments have played a central role in all areas of modern physics to study the microscopic structure and the state of matter. The discovery of x rays by Wilhelm Röntgen in 1895 and their first use in spectrally resolved scattering experiments are closely connected to the emergence of quantum mechanics and statistical physics in the beginning of the last century. The scattering of optical light from free electrons was first observed in 1906 and is referred to Thomson scattering (Thomson, 1906). For geometries, where no component of the electron velocity is probed, the frequency of the scattered optical radiation is unchanged and observations have been explained by the classical theory of electromagnetic waves scattered by charged particles. It was Arthur Holly Compton (1923) who applied x rays for scattering experiments on solid-density materials observing the redshifted Compton line referred to as the Compton effect or Compton scattering. The frequency shift has been explained by the momentum transfer of light quanta to the electrons of the material and has provided direct evidence for the quantum nature of light.

In 1928, spectrally resolved x-ray scattering measurements of the Compton redshifted line provided a direct measurement of a parabolic distribution function reflecting the Fermi energy distribution of electrons in solids (Dumond, 1929). These measurements were performed with week-long exposures of x-ray film and have verified the statistical model for electrons developed in

the same year by Chandrasekhar. At that time, it was thought impossible to observe the broadening of the Compton scattering feature for the ranges of temperatures available in the laboratory (cf. Chandrasekhar, 1929). Scattering experiments on cold solids, however, have continued throughout the last century with improved x-ray sources including synchrotrons. For example, these experiments have investigated the wave functions of bound electrons, x-ray Raman scattering, and collective long-range structure effects (Schülke, 1991).

In the late 1940s, low density laboratory plasma physics experiments began to study hot matter. Magnetically confined plasmas with the goal to perform thermonuclear fusion experiments have accessed matter at unprecedented high temperatures. However, accurate temperature measurements using scattering required the development of powerful light sources due to the small cross section for Thomson scattering,

$$\sigma_{\text{Th}} = \frac{8\pi}{3} r_0^2 = 0.665 \times 10^{-24} \text{ cm}^2, \quad (1)$$

where $r_0 \approx 2.8 \times 10^{-15} \text{ m}$ is the classical electron radius. For the photon energies and applications of interest in this review, the cross section is not dependent on energy. For high energy gamma-ray photons, very strong magnetic fields, or extremely intense radiation, the cross section is modified (Bethe and Guth, 1994). After the introduction of the ruby laser by Maiman (1960) and the first scattering experiments in hot plasmas by Funfer *et al.* (1963) and Kunze *et al.* (1964), Thomson scattering has become a powerful plasma diagnostic technique that is widely employed to measure noncollective and collective features of laboratory plasmas. A large body of theoretical (Dougherty and Farley, 1960; Fejer, 1960; Renau, 1960; Salpeter, 1960) and experimental studies (Kunze, 1968; Evans and Katzenstein, 1969; Sheffield, 1975) was performed, principally oriented to low density plasmas ranging from magnetically confined fusion research plasmas (Peacock *et al.*, 1969) to ICF hohlraums (Glenzer, Alley, *et al.*, 1999; Glenzer, Rozmus, *et al.*, 1999). These studies are limited to electron densities of 10^{21} cm^{-3} and below where ultraviolet probe lasers propagate through the plasma.

With the advent of the field of high energy density physics (Drake, 2006) in this millennium, the need for accurate measurements of the conditions, physical properties, and structure of dense plasmas has emerged. Typically conditions with pressures above 1 Mbar = $10^2 \text{ GPa} = 10^5 \text{ J cm}^{-3}$ are of interest with densities approaching solid density or higher and with temperatures above several eV. Powerful x-ray sources enable these measurements with spectrally resolved x-ray Thomson scattering. They require a large photon flux in a short x-ray burst with high spectral purity to resolve the Compton and plasmon features in short-lived states of matter. Experiments have employed He- α and Ly- α sources to demonstrate Compton and plasmon measurements in isochorically heated beryllium. These proof-of-principle experimental studies have been extended to

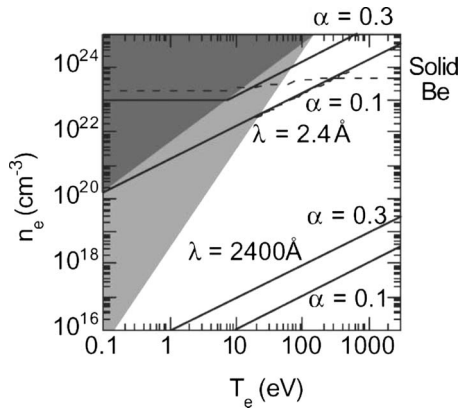


FIG. 1. Density-temperature phase space indicating areas of Fermi-degenerate matter (dark gray area), strongly coupled plasmas (light gray area), and the ideal plasma regime (white area). The solid lines indicate the scattering parameter α from Eq. (5) for backscattering at $\theta=180^\circ$ and ultraviolet and x-ray probes. Also shown is the ionization balance for solid density beryllium (dashed curve). From Landen, Glenzer, *et al.*, 2001.

shock-compressed matter and the characterization of shocks with picosecond temporal resolution employing $K\text{-}\alpha$ x rays. In parallel with the experimental demonstration, the theory of x-ray scattering has been developed including an appropriate description of the inelastic scattering component beyond the random phase approximation with the Mermin approach and close coupling corrections. Also, density-functional theory has been applied for calculating the elastic scattering component.

The experimental and theoretical investigations in this field are reviewed in the following sections. They include observations of the scattering spectrum in both forward and backscatter directions covering a large range of energy shifts. These conditions result in scattering spectra where the Compton effect dominates the frequency of the inelastic scattering component to plasmons scattering where the Compton effect is small compared to the plasma frequency. Hence the term x-ray Thomson scattering is used throughout this review to describe the wide range of plasma conditions and scattering features accessed in the high energy density physics regime.

C. Physical properties of dense plasmas

Figure 1 shows the density-temperature phase space indicating the range of parameters accessed in high energy density physics experiments. X-ray Thomson scattering has been developed to probe conditions approaching solid densities and higher and with temperatures of several eV. These systems span the full range of plasmas from Fermi degenerate to strongly coupled and to high temperature ideal gas plasmas. Scattering experiments have been demonstrated for plasmas with electron densities of up to $n_e=10^{24}\text{ cm}^{-3}$, but experiments at even higher densities will become possible in future ICF capsule implosion experiments. Electron densities approaching $n_e=10^{26}\text{ cm}^{-3}$ are expected, which

are comparable to conditions of the interior of stars, brown dwarfs, and Jovian planets.

In addition to accessing dense plasmas, x-ray Thomson scattering is also important for the characterization of warm dense states of matter at lower densities. It has been a long-standing goal to study the microscopic properties in the regime where the transition from an ideal plasma to a degenerate strongly coupled plasma occurs. In this regime, conventional diagnostic techniques and standard plasma theory, which treat the interactions between particles as a small correction, are often not applicable. In particular, transient plasma behavior at these conditions is observed in dynamical experiments, like laser and particle-solid interactions or Z -pinch experiments, and are of particular importance for ICF experiments. This regime is defined by the degeneracy and coupling parameters.

The degeneracy parameter Θ defines the Fermi-degenerate regime by estimating the role of quantum statistical effects in the system. The parameter is defined by the ratio of the thermal energy and the Fermi energy ϵ_F ,

$$\Theta = \frac{k_B T_e}{\epsilon_F}, \quad \epsilon_F = \frac{\hbar^2}{2m_e} (3\pi^2 n_e)^{2/3}, \quad (2)$$

with k_B the Boltzmann constant, T_e the electron temperature, n_e the electron density, $h=2\pi\hbar$ the Planck's constant, and m_e the mass of the electron. In a degenerate plasma, the Fermi energy is larger than the thermal energy, i.e., $\Theta < 1$, and most electrons populate states inside the Fermi sea where quantum effects are of importance.

The coupling parameter Γ is defined as the ratio of the Coulomb energy between two charged particles at a mean particle distance \bar{d} and the thermal energy (Ichimaru, 1973). Using the Wigner-Seitz radius for \bar{d} , we find an expression for the electron coupling parameter,

$$\Gamma_{ee} = \frac{e^2}{4\pi\epsilon_0 \bar{d} k_B T_e}, \quad \bar{d} = \left(\frac{4\pi n_e}{3} \right)^{-1/3}. \quad (3)$$

Here e is the electric charge and ϵ_0 is the permittivity of free space. For $\Gamma < 1$ the plasma is weakly coupled, and $\Gamma \ll 1$ denotes the ideal plasma regime. Correlations become more important in the coupled plasma regime, where $\Gamma \gtrsim 1$.

In Fig. 1 the regions of strongly coupled plasma and Fermi-degenerate regimes ($\Gamma_{ee} > 1$ and $T_e < \epsilon_F$) are separated by the $\Gamma_{ee}=1$ and $\Theta=1$ curves in electron density–electron temperature phase space. For a given density at the lowest temperatures, the plasmas are either Fermi degenerate or only partially ionized, and hence in a sense only weakly coupled. At higher temperatures, they behave as ideal gases with insignificant inter-particle coupling. In between, the ideal gas approximation for plasma behavior breaks down.

In the strongly coupled plasma regime, various statistical mechanics models predict electron-ion collisionalities that differ by factors of 2–5. Material properties

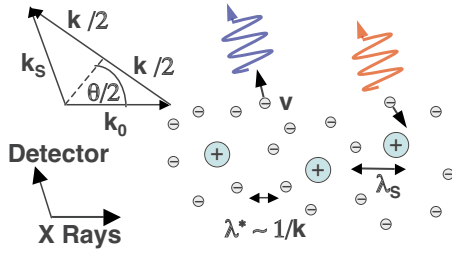


FIG. 2. (Color online) Scattering geometry indicating the length of the scattering vector \mathbf{k} and the relation to the screening length λ_S of the plasma.

such as electrical and thermal conductivity, opacity, and equation of state have been studied in this regime to attempt to resolve theoretical and calculational uncertainties. However, the usefulness of such measurements has been impaired because of the lack of an independent measurement of temperature and density.

D. X-ray scattering regimes

Figure 2 shows the geometry and \mathbf{k} vectors for a back-scattering experiment. The plasma is irradiated either by nonpolarized x rays from a laser-plasma source or by a linearly polarized free electron x-ray laser beam along the direction of the incident wave vector \mathbf{k}_0 with $k_0 = 2\pi/\lambda_0$. The detector observes the scattered radiation at the scattering angle θ in the direction of the scattered wave vector \mathbf{k}_S at a distance much larger than the plasma extension.

During the scattering process, the incident photon transfers on average momentum $\hbar\mathbf{k}$ and the Compton energy $\hbar\omega = \hbar^2 k^2 / 2m_e = \hbar\omega_0 - \hbar\omega_1$ to the electron, where ω_1 is the frequency of the scattered radiation. In the nonrelativistic limit ($\hbar\omega \ll \hbar\omega_0$) and for small momentum transfers we have $\mathbf{k} = 2\mathbf{k}_0 \sin(\theta/2)$; cf. Fig. 2. Thus, the scattering geometry and the probe energy determine the scattering vector \mathbf{k} through

$$k = |\mathbf{k}| = 4\pi \frac{E_0}{hc} \sin(\theta/2). \quad (4)$$

Equation (4) determines the scale length $\lambda^* \approx 2\pi/k$ of the electron density fluctuations measured in the scattering experiment. Comparison with the screening length λ_S determines the scattering regime. The dimensionless scattering parameter α ,

$$\alpha = \frac{1}{k\lambda_S}, \quad (5)$$

with λ_S^{-2} ,

$$\lambda_S^{-2} = \kappa_e^2 = \frac{n_e e^2}{\epsilon_0 k_B T} \frac{F_{-1/2}(\eta_e)}{F_{1/2}(\eta_e)}, \quad (6)$$

is used. Here $\alpha > 1$ defines the collective scattering regime. Density fluctuations at a scale larger than the screening length are observed, while at $\alpha < 1$, i.e., in the

noncollective scattering regime, the density fluctuations of individual electrons are resolved.

In Eq. (6), the inverse electron screening length κ_e is written in terms of Fermi integrals

$$F_\nu(y) = \frac{1}{\Gamma(\nu+1)} \int_0^\infty \frac{dx x^\nu}{\exp(x-y)+1}, \quad (7)$$

where $\Gamma(\nu)$ is the gamma function (Zimmerman, 1987). Equation (6) is valid for any degeneracy via the parameter $\eta_e = \mu_e / k_B T_e$ with μ_e the chemical potential. The usual Debye screening length in the nondegenerate case ($\Theta \gg 1$) gives

$$\lim_{\eta_e \rightarrow -\infty} \kappa_e(\eta_e) = \lambda_D^{-1} = \left(\frac{n_e e^2}{\epsilon_0 k_B T_e} \right)^{1/2}, \quad (8)$$

and the Thomas-Fermi screening length for degenerate systems ($\Theta \leq 1$),

$$\lim_{\eta_e \gg 1} \kappa_e(\eta_e) = \lambda_{TF}^{-1} = \sqrt{\frac{m_e e^2}{\pi \epsilon_0 \hbar^2} \left(\frac{3n_e}{\pi} \right)^{1/3}}. \quad (9)$$

Analytically the screening length with appropriate limits can also be calculated using the effective temperature $T_{cf} = (T_e^2 + T_q^2)^{1/2}$ in Eq. (8). Here $T_q = \epsilon_F / (1.3251 - 0.1779\sqrt{r_s})$, $r_s = \bar{d}/a_B$, and a_B is the Bohr radius (Groni, Glenzer, Rozmus, et al., 2003). This corrected temperature is chosen such that the temperature of an electron liquid obeying classical statistics gives exactly the same correlation energy of a degenerate quantum fluid at $T_e = 0$ obtained from quantum Monte Carlo calculations (Dharma-wardana and Perrot, 2000). This approach was shown to reproduce finite-temperature static response of an electron fluid, valid for arbitrary degeneracy.

As seen from Eqs. (8) and (9), λ_S is determined by the plasma conditions, density, and temperature, while $\lambda^* = 2\pi/k$ is primarily determined by the x-ray probe energy and the scattering angle [i.e., by the setup of the scattering experiment, Eq. (4)]. The latter statement is only approximately fulfilled. When appropriate, well-known corrections to the length of the scattering vector for the finite frequency shift of the scattered radiation and due to the dispersion of the radiation in the dense plasma need to be included. In particular the latter is important in case of soft x-ray or vacuum-ultraviolet probe radiation employed by free-electron lasers (Höll et al., 2007). Finally, for extremely dense states of matter encountered in ICF research, high x-ray probe energies of $E \geq 10$ keV are required to penetrate through the dense plasma of up to 10^{26} cm^{-3} . This case results in large \mathbf{k} vectors limiting scattering experiments at the highest densities to the noncollective regime.

E. Sensitivity of scattering spectra to plasma parameters

With the scattering vector \mathbf{k} defined by Eq. (4), the scattered power P_S from N electrons into a frequency interval $d\omega$ and solid angle $d\Omega$, i.e., the scattering spectrum (Sheffield, 1975), is determined by

$$P_S(\mathbf{R}, \omega) d\Omega d\omega = \frac{P_0 r_0^2 d\Omega}{2\pi A} NS(\mathbf{k}, \omega) d\omega \times |\hat{\mathbf{k}}_S \times (\hat{\mathbf{k}}_S \times \hat{\mathbf{E}}_0)|^2. \quad (10)$$

In Eq. (10), P_0 denotes the incident x-ray power, A is the plasma area irradiated by the probe x rays, and $S(\mathbf{k}, \omega)$ is the total electron dynamic structure factor. The polarization term reflects the dependence of the scattered power on the polarization of the incident radiation; for linearly polarized light, e.g., from a free-electron laser (FEL), $|\hat{\mathbf{k}}_S \times (\hat{\mathbf{k}}_S \times \hat{\mathbf{E}}_0)|^2 = (1 - \sin^2 \theta \cos^2 \varphi)$. The electric field direction of the incident radiation is given by \mathbf{E}_0 with the hat denoting unit vectors, and φ determining the angle between the plane of the scattering vectors and \mathbf{E}_0 . On the other hand, for unpolarized light, e.g., from a laser-plasma source, $|\hat{\mathbf{k}}_S \times (\hat{\mathbf{k}}_S \times \hat{\mathbf{E}}_0)|^2 = (1 - \frac{1}{2} \sin^2 \theta) = \frac{1}{2}(1 + \cos^2 \theta)$. Clearly, for linearly polarized laser sources, a detector at $\varphi = \pi/2$ will measure the maximum scattered light signal. Generally, this term must be included for measurements with absolutely calibrated detectors.

By multiplying Eq. (10) with the length of the scattering volume ℓ it can be seen that the scattered power depends on the setup of the scattering experiment (initial probe power, scattering angle, probe wavelength, probe polarization, and detector solid angle), the electron density, the plasma length, and the total dynamic structure factor $S(\mathbf{k}, \omega)$. The structure factor is defined as the Fourier transform of the electron-electron density fluctuations, containing the details of the correlated many-particle system; cf. Ichimaru (1994). Section III is devoted to the theory of $S(\mathbf{k}, \omega)$ including the elastic and inelastic scattering components in the collective and noncollective regimes. In this section, some approximations are discussed, demonstrating the fundamental principles probed with spectrally resolved x-ray scattering. These relations illustrate the dependence of the measured scattering spectra on the dense plasma conditions.

The frequency shift of a scattered photon by a free electron is determined by the Compton and Doppler effects,

$$\omega = -\hbar k^2/2m_e \pm \mathbf{k} \cdot \mathbf{v}. \quad (11)$$

The former is due to the transfer of momentum from the incident photon to the electron during the scattering process resulting in the Compton downshift of the scattered radiation to lower x-ray energies. This term defines the inelastic scattering component in fully noncollective x-ray Thomson scattering experiments. The Compton shift contains no diagnostic information about the dense plasma. The intensity of this feature, however, indicates the number of electrons and states available for inelastic scattering processes. On the other hand, the spectrum of the Compton-downshifted line reflects the velocity component of the electron in the direction of the scattering vector \mathbf{k} . This fact has been explored in the late 1920s when the spectrum from solids have shown the Fermi velocity distribution function.

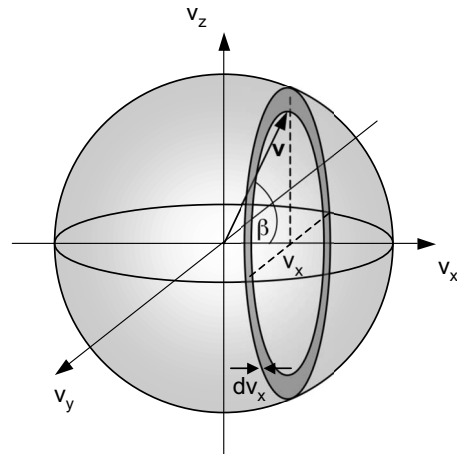


FIG. 3. Volume element in three-dimensional velocity space that determines the number of electrons contributing to the velocity component v_x .

To calculate the number of electrons that contribute to the Doppler broadening via Eq. (11), the three-dimensional velocity space is considered in Fig. 3. The number of electrons within the velocity interval v_x and $v_x + dv_x$ is proportional to the volume described by an annulus around v_x that must be integrated to include all possible projections of velocity vectors \mathbf{v} onto v_x .

From Fig. 3 and with β the angle between \mathbf{v} and the v_x axis the number of electrons is given by

$$f(v_x) dv_x = \int_{v_x}^{v=\infty} n(v) 2\pi \sqrt{v^2 - v_x^2} \frac{dv}{\sin \beta} dv_x. \quad (12)$$

The first term in the integral is the occupation number, described by either Fermi-Dirac or Maxwell-Boltzmann statistics, the second term is the circumference, the third is the annulus width, and the last term is the thickness.

With $v_x = v \cos \theta$, we find

$$f(v_x) dv_x = \int_0^{\pi/2} n\left(\frac{v_x}{\cos \beta}\right) \frac{v_x^2}{\cos^2 \beta} \tan \beta d\beta. \quad (13)$$

Thus, x-ray scattering in the noncollective regime will probe the distribution function. For a Fermi degenerate plasma the width of the downshifted peak is proportional to the Fermi energy. With the Fermi distribution function applied for weakly degenerate plasmas, $k_B T_e < \epsilon_F$, where $v_F = (2\epsilon_F/m_e)^{1/2}$ is the Fermi velocity, Landen, Glenzer, et al. (2001) showed

$$f\left(\frac{v_x}{v_F}\right) \propto \int_0^{\pi/2} \frac{(v_x/v_F \cos \beta)^2 \tan \beta d\beta}{e^{[(v_x/v_F \cos \beta)^2 - \eta]/(T_e/\epsilon_F)} + 1}, \quad (14)$$

with η obtained according to the Sommerfeld expansion,

$$\eta = 1 - \left(\frac{\pi^2}{12}\right) \left(\frac{T_e}{\epsilon_F}\right)^2. \quad (15)$$

The second term accounts for the fact that the chemical potential in the expression for the occupation of states for fermions, $[\exp(E - \mu)/k_B T_e + 1]^{-1}$, has some temperature dependence at finite temperature.

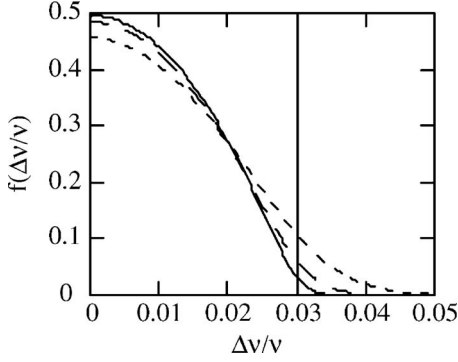


FIG. 4. Calculated Thomson backscattered spectra for various ratios of $k_B T_e / \epsilon_F$ and for $\epsilon_F = 15$ eV. Solid, long dashed, and short dashed correspond to $k_B T_e / \epsilon_F = 0.1, 0.2,$ and $0.4,$ respectively. The spectral shift corresponding to an electron velocity component equal to the Fermi velocity is denoted by a vertical line. Note that only one side of spectrum is shown, and that $\Delta\nu=0$ corresponds to the Compton shifted frequency. From Landen, Glenzer, *et al.*, 2001.

Figure 4 shows the calculated profiles, indicating that the shape and width of the velocity distribution are probed. In a degenerate system, applying Eqs. (14) and (15) will provide the spectrum of the Compton line with the width proportional to $(\epsilon_F)^{1/2}$ and hence to $(n_e)^{1/3}$, yielding the density of the system. In a nondegenerate plasma, on the other hand, the Compton scattering spectrum will reflect a Maxwell-Boltzmann distribution, providing a measure of the electron temperature. In addition to the Compton scattering component, elastic scattering at the incident x-ray energy as well as possible contributions of bound electrons to the inelastic scattering component will also need to be taken into account. The general structure factor of Sec. III includes these effects for the full range of temperatures accessible in experiments and further accounts for finite values of α and effects of collisions.

With decreasing scattering angle and with moderate x-ray probe energies, the scattering length increases and $\alpha > 1$ results in collective scattering. In this case, collective plasmon oscillations have been observed. The plasmon frequency shift from E_0 is determined by the plasmon dispersion relation and the width is determined by Landau damping and collisional damping processes. While these damping processes are treated in Sec. III, we note here that the plasmon frequency shift can be approximated for small values of k using an inversion of Fermi integrals given by Zimmerman (1987) that results in a modified Bohm-Gross dispersion relation (Höll *et al.*, 2007; Thiele *et al.*, 2008)

$$\omega_{\text{pl}}^2 = \omega_p^2 + 3k^2 v_{\text{th}}^2 (1 + 0.088 n_e \Lambda_e^3) + \left(\frac{\hbar k^2}{2m_e} \right)^2, \quad (16)$$

where $\omega_p = \sqrt{n_e e^2 / \epsilon_0 m_e}$ is the plasma frequency, $v_{\text{th}} = \sqrt{k_B T_e / m_e}$ is the thermal velocity, and $\Lambda_e = h / \sqrt{2\pi m_e k_B T_e}$ is the thermal wavelength.

In Eq. (16) the first term is a result of electron oscillations in the plasma (Tonks and Langmuir, 1929), the

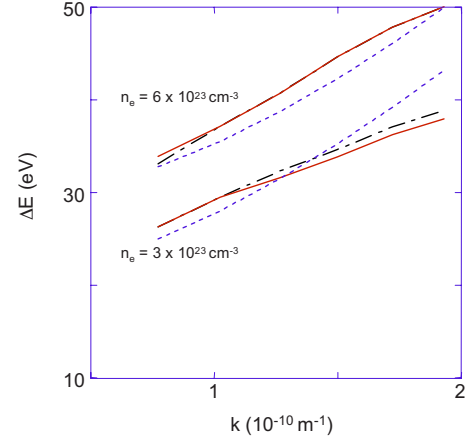


FIG. 5. (Color online) The plasmon dispersion with the plasmon energy shift from the incident x-ray energy E_0 vs k . The calculations are for beryllium plasmas with $T_e = 12$ eV, $Z = 2.5$, $E_0 = 4.75$ keV, $n_e = 3 \times 10^{23}$ cm $^{-3}$, and $n_e = 6 \times 10^{23}$ cm $^{-3}$. Solid, long dashed, and short dashed correspond to calculations with Born-Mermin theory, the random phase approximation, and with Eq. (16), respectively. From Thiele *et al.*, 2008.

second term represents the effect on propagation of the oscillation from thermal pressure. The third term includes degeneracy effects from Fermi pressure, and the last term is the quantum shift (Haas *et al.*, 2000). The quantum shift and the electron oscillation terms are temperature independent, and, for the partially degenerate plasmas of interest here, the thermal pressure is weakly dependent on T_e . Therefore, for small temperatures, no accurate knowledge of the temperature is required, and the plasmon energy provides a sensitive measure of the plasma electron density.

Figure 5 shows the energy shift of the plasmon versus the length of the scattering vector \mathbf{k} for a dense beryllium plasma. The conditions are chosen such that the scattering is collective with $\alpha > 1$ spanning the range of scattering angles between 30° and 90° . These calculations show that the random phase approximation agrees closely with the Born-Mermin theory for a wide range of conditions; discrepancies observed for $k > 10^{-10}$ m $^{-1}$ and $n_e = 3 \times 10^{23}$ cm $^{-3}$ are smaller than 1 eV, which is difficult to resolve with present experimental capabilities. This study shows that error bars in the measurement of the density from the plasmon dispersion can be expected to be of order 5% or less when applying these theories. On the other hand, Eq. (16) shows deviations from the Born-Mermin theory of order 2 eV, indicating that the analytical approximation needs to be applied with caution.

The relation that demonstrates the fundamental principles probed with spectrally resolved x-ray scattering is derived from the fluctuation-dissipation theorem. The density fluctuations in the plasma, described by the dynamic structure factor, are related to the dissipation of energy, described by the dielectric function $\epsilon(\mathbf{k}, \omega)$,

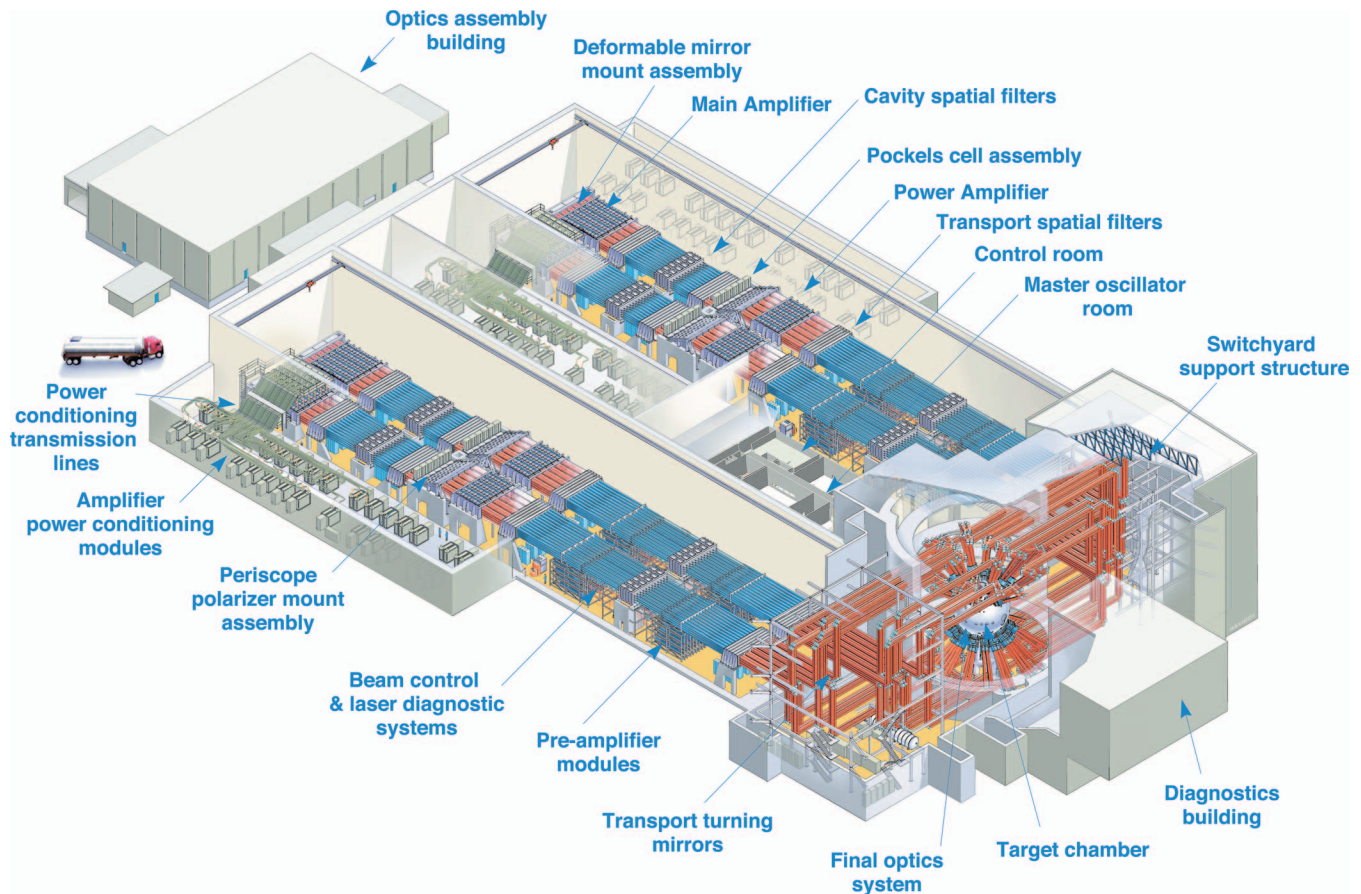


FIG. 6. (Color) Schematic view of the National Ignition Facility (NIF) showing the main components of the laser system (Moses and Wuest, 2005).

$$S(\mathbf{k}, \omega) = \frac{\varepsilon_0 \hbar k^2}{\pi e^2 n_e} \frac{1}{1 - e^{\hbar\omega/k_B T_e}} \text{Im} \varepsilon^{-1}(\mathbf{k}, \omega). \quad (17)$$

Independent of evaluating the dielectric function, the shape of the structure factor, and modeling collisional effects, the dielectric function fulfills the requirement

$$\frac{S(\mathbf{k}, \omega)}{S(-\mathbf{k}, -\omega)} = e^{-\hbar\omega/k_B T_e}. \quad (18)$$

This relation is referred to as the detailed balance relation. As a general consequence, the structure factor shows an asymmetry with respect to \mathbf{k} and ω that has been observed in many experiments. In principle, this relation could also be used to infer the temperature since, when applied to plasmons, it provides the electron temperature independent of a detailed formulation of dissipative processes in the plasma. However, conditions with sufficiently high temperatures and small noise amplitudes are required to reliably measure the upshifted plasmon. This measurement has recently been demonstrated by Döppner *et al.* (2009).

II. FACILITIES FOR X-RAY THOMSON SCATTERING EXPERIMENTS

With the completion of the National Ignition Facility (NIF) (Moses and Wuest, 2005) at the Lawrence Liver-

more National Laboratory in the United States and the Laser Megajoule (Cavailler, 2005) in France, two premier laser facilities for accessing the high energy density physics regime are becoming available. The NIF will include both the capability for high energy and ultrashort-pulse laser-produced x-ray probings of unprecedented x-ray fluence and energy. A total of 192 beamlets arranged in 48 quads of beams will deliver a total energy of 1.8 MJ in 500 TW for up to 30 ns long laser pulses, cf. Fig. 6. A quad of four beams, entering the target chamber through one port, will exceed the laser energy used in present experiments at the Omega laser facility (Soures *et al.*, 1993; Boehly *et al.*, 1997), providing sufficient energy for x-ray probing with scattering or radiography. A quad of four beamlets operating at 351 nm can provide up to 40 kJ at 351 nm, or 84 kJ at 526 nm in several nanosecond long pulses. The laser intensity on target is tailored using continuous phase plates (Dixit *et al.*, 1996), spanning the range of intensities of 10^{14} – 10^{16} W cm $^{-2}$ per quad of beams where optimum conversion efficiency for thermal laser-produced He- α and Ly- α x-ray sources have been demonstrated; cf. Sec. IV.B.

Experiments on NIF with the first quad have begun in 2003 and results on laser-plasma interaction instabilities, hydrodynamics instabilities and radiation hydrodynamics have been reported by Glenzer *et al.* (2004), Blue *et*

al. (2005), Dewald *et al.* (2005), Landen *et al.* (2006), and Glenzer, Froula, *et al.* (2007). The goal of NIF experiments is to show the feasibility of inertial confinement fusion, perform high energy density physics experiments, and study astrophysics processes in the laboratory. These studies share the need to prepare materials at extreme conditions accessing the high energy density physics regime for which accurate probing with x-ray scattering will be an important diagnostic for measuring the conditions and properties.

In addition to the long-pulse laser beams, the NIF will also provide an ultrashort-pulse laser capability (ARC) (Barty *et al.*, 2004). In one NIF beamlet aperture, it is planned to deliver a total energy between 1 and 3 kJ in ~ 1 to 50 ps long pulses at the fundamental laser wavelength of 1053 nm. Up to eight short-pulse beams in four NIF apertures with 10 kJ in 10 ps will provide a capability greatly surpassing present ultrashort-pulse laser parameters where laser-produced $K\text{-}\alpha$ x rays are applied for x-ray probing (Kritcher, Neumayer, Castor, *et al.*, 2008). The intensity on target per short-pulse beam will reach $\sim 10^{18}$ W cm $^{-2}$ for 10 ps long pulses that can be independently timed with up to 20 ns delay with respect to the long-pulse beams. As discussed in Sec. IV.B, at these intensities $K\text{-}\alpha$ probe radiation is efficiently produced.

The Omega laser facility at the Laboratory for Laser Energetics (Soures *et al.*, 1993; Boehly *et al.*, 1997) has been the first facility where x-ray Thomson scattering measurements have been successfully performed. This is a 60-beam facility delivering routinely 500 J energy per beam on target at 351 nm wavelength and in a 1 ns long flat-top pulse. The single beam laser pulse duration can be varied over 0.1–4 ns, and can be flat-topped, Gaussian, or custom-designed shapes. Typically 3.5 to 12 kJ of laser energy has been employed for producing chlorine Ly- α at 2.96 keV, titanium He- α at 4.75 keV, and zinc He- α at 9 keV. These x-ray scattering probes have been successfully fielded for single-shot experiments. These sources have provided 10^{14} photons at the dense plasma sample with appropriate bandwidth for spectrally resolving Compton and plasmon spectral features.

The Omega enhanced performance upgrade described by Stoeckl *et al.* (2006) has added energetic ultrashort-pulse laser capability to nanosecond laser beams. This facility uses a similar architecture of chirped pulse amplification (Strickland and Mourou, 1985) as that on NIF. When completed, two short-pulse beams can be combined collinearly and routed into the 60-beam target chamber delivering up to 2.6 kJ at 10 ps pulse length or 1 kJ at 1 ps pulse length in one beam. The other beam can deliver up to 2.6 kJ at pulse lengths of ≥ 80 ps. Alternatively, the short-pulse laser beams can also be combined with up to four 10 ns, 6.5 kJ beams of NIF-type architecture into a separate target chamber. In this case, the short-pulse beams can be operated with up to 2.6 kJ at ≥ 10 ps or 1 kJ at 1 ps.

These kilojoule laser facilities allow experiments where both the x-ray probe and high energy density

plasma conditions are produced with energetic laser beams. This is accomplished by individually pointing the beams to various targets and by timing and pulse shaping the laser pulses to effectively produce the x-ray probe and the dense plasma. An alternative approach is to employ pulsed power to create the latter. For example, the Z machine at Sandia National Laboratory can generate a current of 20 MA and has been refurbished to increase the current to 30 MA (Matzen *et al.*, 2005). The discharge through a wire array allows pulse shaping control and efficient multi-keV x-ray production. Plasmas have been produced with x-ray energies approaching 2 MJ at powers of >200 TW for inertial confinement fusion and high energy density physics (HEDP) experiments. In addition, shock strength above 1 Mbar and plasma jets have been produced.

These conditions can be probed with a large-aperture (30-cm) kilojoule-class Nd:glass laser system, the Z beamlet (Rambo *et al.*, 2005). The laser, operating with typical pulse durations from 0.3 to 1.5 ns, employs a sequence of successively larger multipass amplifiers to achieve up to 3 kJ energy at a wavelength of 1054 nm. Large-aperture frequency conversion and long-distance beam transport can provide on-target energies of up to 1.5 kJ at 527 nm. Although less energy than employed at Omega, this capability significantly exceeds the energy for x-ray probing that is available at medium-sized laser facilities.

On several medium-sized lasers, namely the LULI 2000 laser at the Ecole Polytechnique, the Vulcan laser at the Rutherford Appleton Laboratory, and the Titan laser at the Lawrence Livermore National Laboratory, x-ray Thomson scattering experiments have been successfully fielded. While the scattering experiments on the former two facilities by Riley *et al.* (2000) and Ravasio *et al.* (2007) have primarily investigated diffraction on warm dense matter, experiments with the Titan laser have demonstrated inelastic x-ray Thomson scattering on plasmons with 10^{12} x-ray probe photons at the dense plasma. The Titan laser beams, which originate from the Janus laser, consist of one 300-J petawatt-class beam together with a second nanosecond laser that can operate independently from each other. While the short pulse beam provides 0.7–50 ps long pulses with intensities up to 10^{18} W cm $^{-2}$, the long-pulse beam employs NIF-like pulse shaping capable of producing multiple shock waves with pressures of 3–4 Mbar. The x-ray Thomson scattering experiments by Kritcher, Neumayer, Castor, *et al.* (2008) probed multiple coalescing shock waves with 10 ps temporal resolution via short-pulse laser-produced Ti $K\text{-}\alpha$ radiation.

In addition, there are several medium-size laser facilities with laser energy and power capabilities in the appropriate range for producing powerful laser-produced x-ray probes. Among those are the Trident laser (Montgomery *et al.*, 2001; Froula *et al.*, 2002; Niemann *et al.*, 2004) at the Los Alamos National Laboratory, the LIL laser in France (Eyharts *et al.*, 2006), the Xingguang II laser facility (Bai *et al.*, 2001), and the Gekko laser

(Kodama *et al.*, 2001; Snavely *et al.*, 2007). In addition, new laser facilities will come online in the near future, e.g., the Fast Ignition Realization Experiment (Azechi and Project, 2006; Mima *et al.*, 2007) or the Phelix laser at the Gesellschaft für Schwerionenforschung, Germany (Neumayer *et al.*, 2005). In addition, soft x-ray laser facilities (Klisnick *et al.*, 2006; Rus *et al.*, 2007) with energies of $10 \mu\text{J}$ – 1 mJ at 13.9 nm have also been considered for scattering experiments in the extreme ultraviolet spectral range by Baldis *et al.* (2002).

A powerful alternative to long-pulse laser-produced He- α and Ly- α or short-pulse laser-produced K- α probe x rays are FELs [see, e.g., Lee *et al.* (2003)]. They provide new x-ray capabilities suited to fulfill the stringent simultaneous requirements on photon flux, energy, and bandwidth for x-ray scattering experiments in the high energy density physics regime (Höll *et al.*, 2007). The Free-Electron Laser at Hamburg (Ackermann *et al.*, 2007) delivers pulses with on-target energies of approximately $50 \mu\text{J}$ with 10^{12} – 10^{13} photons in the extreme ultraviolet spectral range between about 6.5 and 40 nm . The temporal pulse width of $\sim 20 \text{ fs}$ and the bandwidth of $\Delta E/E = 0.5\%$ is suitable for x-ray probing, capable of resolving rapidly changing hydrodynamic conditions. The complete transverse coherence results in diffraction limited spots with a focal spot size as low as $2 \mu\text{m}$ diameter and intensities approaching $10^{17} \text{ W cm}^{-2}$. These properties together with the high repetition rate of 10^4 pulses per second allows scattering experiments with femtosecond temporal and micrometer spatial resolutions on dense plasmas. For example, cryogenic hydrogen or helium targets that can be heated by an optical ultra short-pulse laser beam have been proposed by Höll *et al.* (2007) to study matter at electron densities of $\geq 10^{22} \text{ cm}^{-3}$, cf. Tschentscher and Toleikis (2005).

With the construction of the Linac Coherent Light Source in the USA and the X-ray Free-Electron Laser projects in Germany and Japan, x-ray energies of 10 keV and an order of magnitude larger photon flux will become available to probe dense plasmas produced in compressed matter experiments. First results on the former injector have recently been reported by Akre (2008). In particular, higher photon flux in short pulses will allow resolving smaller plasma regions than current experiments, eliminating the need to produce large homogeneous plasma samples. This capability will allow for the first time the measurement of the dynamics of dense matter thermal equilibration rates and the formation of thermal equilibrium.

III. THEORY OF THE DYNAMIC STRUCTURE FACTOR

A. General expressions

The dynamic structure factor $S(\mathbf{k}, \omega)$ is directly related to the spectrally resolved Thomson scattering signal via Eq. (10) and contains, as the spectral function of the electron-electron density fluctuations, important information on the correlated many-particle system. This quantity is, therefore, of paramount importance for the

development of a consistent quantum statistical theory for strongly correlated systems (Ichimaru, 1973; Kremp *et al.*, 2005). X-ray Thomson scattering offers the possibility to test various concepts of many-particle theory for strongly coupled plasmas and the validity of standard approximations in a conclusive way.

The dynamic structure factor $S(\mathbf{k}, \omega)$ is related to the imaginary part of the inverse dielectric function $\varepsilon^{-1}(\mathbf{k}, \omega)$ via the fluctuation-dissipation theorem (Kubo, 1966) [see Eq. (17)]. The (longitudinal) dielectric function $\varepsilon(\mathbf{k}, \omega)$ is connected with the polarization function $\Pi(\mathbf{k}, \omega)$ and the dynamic conductivity $\sigma(\mathbf{k}, \omega)$ via

$$\varepsilon(\mathbf{k}, \omega) = 1 - \frac{1}{\varepsilon_0 k^2} \Pi(\mathbf{k}, \omega) = 1 + \frac{i}{\varepsilon_0 \omega} \sigma(\mathbf{k}, \omega). \quad (19)$$

The dielectric or polarization function have to be calculated for the many-particle system under consideration in order to derive the dynamic structure factor or other physical quantities. For example, the long-wavelength limit of the transverse dielectric function yields optical properties such as the index of refraction $n(\omega)$ and the absorption coefficient $\alpha(\omega)$ according to

$$\lim_{k \rightarrow 0} \varepsilon_{tr}(\mathbf{k}, \omega) = \left(n(\omega) + \frac{ic}{2\omega} \alpha(\omega) \right)^2, \quad (20)$$

while the longitudinal dielectric function is related to the stopping power and the transport properties [see Zwirknagel *et al.* (1999) and Reinholz (2005)].

Quantum effects and strong correlations in solid-density plasmas require the application of consistent quantum statistical methods which is still an issue of ongoing research. The various sum rules

$$\int_{-\infty}^{+\infty} \frac{d\omega}{\pi} \omega^n \text{Im } \varepsilon^{\pm 1}(\mathbf{k}, \omega) = C_n^{\pm}(\mathbf{k}) \quad (21)$$

have to be fulfilled when constructing approximate solutions for the dielectric function [see Röpke and Wierling (1998) and Reinholz *et al.* (2000)]. For example, the f -sum rule $C_1^- = -\omega_{pl}^2$ follows from particle conservation and describes the sum of oscillator strengths for transitions from the ground to excited states. The conductivity sum rule $C_1^+ = \omega_{pl}^2$ results from the integral over the dissipative part of the dielectric function, the dynamic conductivity $\sigma(\mathbf{k}, \omega)$ [see Eq. (19)].

Approximate expressions for the dielectric function of strongly correlated plasmas are usually expressed by means of the known result for an ideal collisionless plasma, the RPA [see Eq. (38) below]. Extensions for strongly correlated plasmas have been developed within the concept of dynamical local field corrections (LFC) (Ichimaru *et al.*, 1982),

$$\varepsilon(\mathbf{k}, \omega) = 1 - \frac{\Pi^{\text{RPA}}(\mathbf{k}, \omega)/\varepsilon_0 k^2}{1 + G(\mathbf{k}, \omega)\Pi^{\text{RPA}}(\mathbf{k}, \omega)/\varepsilon_0 k^2}. \quad (22)$$

A first simple expression for the static LFC $G(k)$ was derived by Hubbard (1958), accounting for the exchange-correlation hole in a dense electron gas. Singwi *et al.* (1968) developed a self-consistent scheme

for calculating the dynamic LFC by accounting for the sum rules mentioned above. [Ichimaru *et al.* \(1984\)](#) extended this approach by treating the ionic correlations within classical HNC calculations and treating screening effects within linear response theory. They were able to construct interpolation formulas for the static LFC $G(k)$ ([Ichimaru *et al.*, 1982](#)) which have found wide application since then.

Alternatively, collisions between the electrons and ions represent important correlations and the dominating dissipation mechanism in dense plasmas which can be treated systematically within an effective linear response theory ([Röpke, 1998](#)). As a result, a generalized expression for the dielectric function accounting for collisions in terms of force-force correlation functions can be derived which is applicable in the entire (\mathbf{k}, ω) space. The expression can also be related to the classical [Drude \(1890\)](#) formula,

$$\varepsilon(\mathbf{k}, \omega) = 1 - \frac{\omega_{\text{pl}}^2}{\omega[\omega + i\nu(\mathbf{k}, \omega)]}, \quad (23)$$

where the dynamic collision frequency $\nu(\mathbf{k}, \omega)$ represents the damping of plasma oscillations due to collisions in

$$\varepsilon^{\text{M}}(\mathbf{k}, \omega) - 1 = \frac{[1 + i\nu(\omega)/\omega][\varepsilon^{\text{RPA}}(\mathbf{k}, \omega + i\nu(\omega)) - 1]}{1 + i[\nu(\omega)/\omega][\varepsilon^{\text{RPA}}(\mathbf{k}, \omega + i\nu(\omega)) - 1]/[\varepsilon^{\text{RPA}}(\mathbf{k}, 0) - 1]}, \quad (25)$$

which is exact in the long-wavelength limit $k \rightarrow 0$ and also serves as a good approximation for finite transfer momenta k . It is still an open question whether or not the concept of dynamic LFC, Eq. (22), or the extended Mermin ansatz, Eq. (25), is able to describe strongly coupled plasmas with $\Gamma \gg 1$ and $\Theta \ll 1$ correctly (see Fig. 1).

While short-range correlations such as exchange interactions are well described within the concept of LFC, long-range correlations such as screening and collisions are effectively accounted for by means of a collision frequency. Both concepts are closely related as can be seen from Eqs. (22) and (23),

$$\nu(\omega) = -i \frac{\omega_{\text{pl}}^2}{\omega} G(0, \omega). \quad (26)$$

An alternative promising approach to determine the full wave vector and frequency-dependent correlation functions in strongly correlated plasmas is to calculate the density-density autocorrelation function via time-averaged *ab initio* molecular dynamics simulations and to perform an ensemble average over a sufficient number of different runs with varying initial microscopic configurations. However, this scheme requires long simulation times τ and a large number of particles N so that it has been implemented up to now only within classical molecular dynamics simulations with effective pair

the system. Note that the original Drude ansatz contained only a constant collision frequency ν . The dynamic collision frequency directly determines the dynamic conductivity via Eq. (19),

$$\sigma(\mathbf{k}, \omega) = \frac{\varepsilon_0 \omega_{\text{pl}}^2}{i\omega + \nu(\mathbf{k}, \omega)}, \quad (24)$$

and is, therefore, a key quantity in this context. It can directly be related to the electrical conductivity in the plasma, e.g., the Ziman or Spitzer formula ([Röpke, 1998](#)). [Mermin \(1970\)](#) constructed a generalized dielectric function by adopting the original Drude ansatz for the whole dynamics of the RPA dielectric function and by exploiting local particle conservation. This has been extended further by accounting for local energy conservation ([Röpke *et al.*, 1999](#); [Selchow *et al.*, 2002](#)) so that the following expression using the dynamic collision frequency $\nu(\omega)$ was derived:

interactions [see [Selchow *et al.* \(2001\)](#) and [Morozov *et al.* \(2005\)](#)].

B. Application to Thomson scattering

For the analysis of the respective Thomson scattering signal, we need the total electronic dynamic structure factor or the inverse total electronic dielectric function $\varepsilon^{-1}(\mathbf{k}, \omega)$ via the fluctuation-dissipation theorem [see Eq. (17)]. We introduce the density-density response function $\chi_{cd}(\mathbf{k}, \omega)$ between particles of species c and d according to [Ichimaru \(1973\)](#),

$$\frac{1}{\varepsilon(\mathbf{k}, \omega)} = 1 + \frac{1}{\varepsilon_0 k^2} \sum_{cd} \chi_{cd}(\mathbf{k}, \omega), \quad (27)$$

which describes the induced density fluctuations of species c due to the influence of an external field on particles of species d . It measures the polarization of the system (i.e., the induced charge density) in terms of the external field

$$\sum_{cd} \chi_{cd}(\mathbf{k}, \omega) = \frac{\Pi(\mathbf{k}, \omega)}{\varepsilon(\mathbf{k}, \omega)}. \quad (28)$$

The total electronic dynamic structure factor is then given by

$$S_{ee}(\mathbf{k}, \omega) = -\frac{\hbar}{\pi n_e^{\text{tot}}} \frac{1}{1 - e^{-\beta\hbar\omega}} \text{Im} \chi_{ee}^{\text{tot}}(\mathbf{k}, \omega), \quad (29)$$

with n_e^{tot} being the total electron density defined below.

The total electron density-density response function χ_{ee}^{tot} can be given as (Salpeter, 1960; Selchow *et al.*, 2001)

$$\chi_{ee}^{\text{tot}}(\mathbf{k}, \omega) = \Omega_0 \frac{i}{\hbar} \int_0^{+\infty} dt e^{i(\omega+i\delta)t} \times \langle [\delta n_e^{\text{tot}}(\mathbf{k}, t), \delta n_e^{\text{tot}}(-\mathbf{k}, 0)] \rangle, \quad (30)$$

with $\delta n_e^{\text{tot}} = n_e^{\text{tot}} - \langle n_e^{\text{tot}} \rangle$ the density fluctuations of all electrons relative to the average density and the brackets denoting the ensemble average; the normalization volume is Ω_0 . The limit $\delta \rightarrow 0$ has to be taken after the thermodynamic limit.

The solution of Eq. (30) for a two-component electron-ion plasma accounting for bound states is a nontrivial problem [see Röpke and Der (1979)]. Here we follow the idea of Chihara (1987, 2000) who applied a chemical picture and decomposed the electrons into free and bound (i.e., core) electrons of density n_e and n_e^b , respectively. With Z_f free and Z_b bound electrons per nucleus, n_e and n_e^b are related to the ion density n_i according to $n_e = Z_f n_i$ and $n_e^b = Z_b n_i$. Writing the total electron density $n_e^{\text{tot}} = n_e + n_e^b$, we can decompose the total density response function in Eq. (30) according to

$$\chi_{ee}^{\text{tot}} = \chi_{ff} + \chi_{bb} + \chi_{bf} + \chi_{fb} = \chi_{ff} + \chi_{bb} + 2\chi_{bf}, \quad (31)$$

with the electron density response functions of the free-free, bound-bound, bound-free, and free-bound systems χ_{ff} , χ_{bb} , χ_{bf} , and χ_{fb} , respectively. The response functions are defined as in Eq. (30) with the corresponding electron densities. We also used $\chi_{bf} = \chi_{fb}$. Note that Z_f includes both the truly free (removed from the atom by ionization) and the valence (delocalized) electrons.

Assuming the system is isotropic, as in the case of interest here (liquid metals or plasmas), the dynamic structure factor depends only on the magnitude of $k = |\mathbf{k}|$, not on its direction. The next step consists in separating the total density fluctuations between the free (Z_f) and bound (Z_b) electron contributions, and separating the motion of the electrons from the motion of the ions. The details of this procedure are given by Chihara (1987, 2000), thus obtaining for the total electron dynamic structure factor

$$S_{ee}(k, \omega) = |f_f(k) + q(k)|^2 S_{ii}(k, \omega) + Z_f S_{ee}^0(k, \omega) + Z_b \int d\omega' \tilde{S}_{ce}(k, \omega - \omega') S_S(k, \omega'). \quad (32)$$

The first term in Eq. (32) accounts for the density correlations of electrons that dynamically follow the ion motion. This includes both the bound electrons, represented by the ion form factor $f_f(k)$, and the screening cloud of free (and valence) electrons that surround the ion, represented by $q(k)$. The ion-ion density correlation function $S_{ii}(k, \omega)$ reflects the thermal motion of the ions and/or the ion plasma frequency. Gregori, Glenzer, Roz-

mus, *et al.* (2003) showed that the following approximation is sufficient, $S_{ii}(k, \omega) = S_{ii}(k) \delta(\omega)$, thus calculating the static structure factor for ion-ion correlations, $S_{ii}(k)$ (see Sec. III.C). In case of a mixture of several ionic species, the scattering contributions from all species as well as their mutual correlations have to be included: cf. Gregori, Glenzer, and Landen (2006).

The second term in Eq. (32) gives the scattering contribution from the free electrons that do not follow the ion motion. Here $S_{ee}^0(k, \omega)$ is the high frequency part of the electron-electron correlation function (Ichimaru, 1973) and it reduces to the usual electron feature (Salpeter, 1960) in the case of an optical probe. Assuming that interparticle interactions are weak, so that the non-linear interaction between different density fluctuations is negligible, the dielectric function can be derived in RPA (Pines and Bohm, 1952; Pines and Nozieres, 1990). In the classical limit, it reduces to the usual Vlasov equation. In the limit of the RPA, strong coupling effects are not accounted for, thus limiting the model validity to plasma conditions in the range of the nonideality parameter of $\Gamma \sim N_s^{-2/3} < 2$, where N_s is the number of electrons inside the Debye sphere.

In the limit $T_e \rightarrow 0$, which corresponds to an electron gas in the ground state, the dielectric function takes the Lindhard-Sommerfeld form [see Pines and Nozieres (1990)]. In the case of scattering from uncorrelated electrons, the form of the dynamic structure factor follows the electron velocity distribution function (Dumond, 1929) showing a parabolic Fermi function (Sec. I.E).

The last term of Eq. (32) includes inelastic scattering by strongly bound core electrons, which arises from Raman transitions to the continuum of core electrons within an ion, $\tilde{S}_{ce}(k, \omega)$, modulated by the self-motion of the ions, represented by $S_S(k, \omega)$. For the experimental spectra described in Sec. V, we find that this contribution is quite small compared to the free-electron dynamic structure factor. In addition, the Raman band has a width comparable or larger than the Compton band (Isolah *et al.*, 1991), so we can regard this type of contribution as yielding a contribution to the wing of the free-electron feature.

Treating bound electrons in a simplifying, frozen core approximation, we find from Eq. (31) for a two-component electron-ion plasma

$$\chi_{ff} = \chi_{ee}^{\text{RPA}}, \quad \chi_{bb} = Z_b^2 \chi_{ii}^{\text{RPA}}, \quad \chi_{bf} = Z_b \chi_{ei}^{\text{RPA}}, \quad (33)$$

where the partial response functions are calculated, e.g., in RPA or improved approaches. In order to evaluate the Thomson scattering signal it is helpful to extract the ionic terms from the electron contribution which describe the screening of the ions by quasifree electrons so that Höll *et al.* (2007) derived the following expression from Eq. (31):

$$\chi_{ee}^{\text{tot}} = \chi_{ee}^{\text{RPA}} + \left(Z_b + \frac{\chi_{ei}^{\text{RPA}}}{\chi_{ii}^{\text{RPA}}} \right)^2 \chi_{ii}^{\text{RPA}}. \quad (34)$$

C. Elastic scattering feature

In the frozen core approximation discussed above, see Eq. (34), we neglect bound-free transitions and treat the ions adiabatically, i.e., the frequency dependence is reduced to a delta function,

$$S_i(k, \omega) = |f_i(k) + q(k)|^2 S_{ii}(k, \omega) = \left| Z_b + \sqrt{Z_f} \frac{S_{ei}(k)}{S_{ii}(k)} \right|^2 S_{ii}(k) \delta(\omega). \quad (35)$$

We have $Z_b = \lim_{k \rightarrow 0} f_i(k)$ and the screening function $q(k)$ is extracted from the ionic terms of the RPA response function. $S_{ei}(k)$ and $S_{ii}(k)$ are the static electron-ion and ion-ion structure factors, respectively. Numerical results for $S_{ei}(k)$ and $S_{ii}(k)$ as well as for the total elastic contribution $S_i(k)$ are given in Sec. III.F.4.

Note that Eq. (35) can be improved by calculating the ionic form factor $f_i(k)$ via the wave functions of the bound core electrons using of appropriate methods, e.g., the Hartree-Fock self-consistent field method of James (1962). For low- Z elements such as hydrogen or beryllium, one can use hydrogenic wave functions for the K -shell $1s$ electrons which gives $f_{1,1s}(k) = 1/(1+k^2 a_s^2/4)^2$, with a_s an effective Bohr radius; its size can be found elsewhere (Pauling and Sherman, 1932). The static elastic scattering feature is then given instead of Eq. (35) by Gregori, Glenzer, Rozmus, *et al.* (2003),

$$S_i(k) = \left| Z_b f_{1,1s}(k) + \sqrt{Z_f} \frac{S_{ei}(k)}{S_{ii}(k)} \right|^2 S_{ii}(k). \quad (36)$$

$$\nu^B(\omega) = -i \frac{\varepsilon_0 \Omega_0^2 n_i}{6 \pi^2 e^2 m_e n_e} \int_0^\infty dk k^6 [V_{ei}^S(k)]^2 S_{ii}(k) \frac{1}{\omega} [\varepsilon_e^{\text{RPA}}(k, \omega) - \varepsilon_e^{\text{RPA}}(k, 0)]. \quad (40)$$

$V_{ei}^S(k) = Z_f e^2 / \varepsilon_0 (k^2 + \kappa_{sc}^2)$ is the statically screened potential with the inverse screening length κ_{sc} . $S_{ii}(k)$ is the aforementioned static ion-ion structure factor. Going beyond the Born approximation is, in principle, possible but evaluating multifrequency contributions in a screened ladder T -matrix (TM) equation is rather involved and not solved yet [see Reinholz (2005) for details]. Furthermore, the so-called Gould-DeWitt (GDW) approximation, $\nu(\omega)^{\text{GDW}} \equiv \nu(\omega)^{\text{TM}} + \nu(\omega)^{\text{LB}} - \nu(\omega)^B$ which treats strong collisions on TM level and dynamical screening effects on the level of the Lenard-Balescu (LB) collision term, already requires a self-consistent solution for the dielectric function since dynamic screening effects are considered in the LB collision integral explicitly.

As shown by Redmer *et al.* (1990) the GDW approximation works well for static quantities such as the dc

D. Free-electron feature

The free-electron contribution to the dynamic structure factor $S_e(k, \omega) = Z_f S_{ee}^0(k, \omega)$ is computed via the fluctuation-dissipation theorem, Eq. (29), i.e., the free-electron density response function $\chi_{ee}(k, \omega)$ that was introduced in RPA as first term in Eq. (34). However, for strongly correlated plasmas we have to account for collisions. They are treated within the Mermin ansatz, Eq. (25), so that for the free-electron density response function follows

$$\chi_{ee}^M(k, \omega) = \left(1 - \frac{i\omega}{\nu(\omega)} \right) \times \left(\frac{\chi_e^{\text{RPA}}(k, z) \chi_e^{\text{RPA}}(k, 0)}{\chi_e^{\text{RPA}}(k, z) - [i\omega/\nu(\omega)] \chi_e^{\text{RPA}}(k, 0)} \right), \quad (37)$$

with $z = \omega - \text{Im} \nu(\omega) + i \text{Re} \nu(\omega)$. The collisionless response function $\chi_e^{\text{RPA}}(k, \omega)$ is evaluated in RPA numerically without any further approximation, i.e., for any degeneracy parameter Θ defined in Eq. (2) [see Arista and Brandt (1984)],

$$\chi_e^{\text{RPA}}(k, \omega) = \frac{1}{\Omega_0} \sum_p \frac{f_e(p+k/2) - f_e(p-k/2)}{\Delta E_e(p, k) - \hbar(\omega - i\eta)}, \quad (38)$$

with $\Delta E_e(p, k) = E_e(p+k/2) - E_e(p-k/2) = \hbar \mathbf{k} \cdot \mathbf{p} / m_e$. The Fermi distribution functions are given by

$$f_e(p) = \frac{1}{\exp\{[E_e(p) - \mu_e]/k_B T_e\} + 1}. \quad (39)$$

The collision frequency is taken in Born approximation from Reinholz (2005),

conductivity but is rather involved for the dynamic collision frequency $\nu(\omega)$. Therefore, we restrict all further calculations to the Born-Mermin approximation (BMA) which is valid for strongly coupled plasmas with $\Gamma \geq 1$. Further simplifying assumptions can be made at this level in order to study the influence of different effects.

1. Two-component screening

We first neglect ionic correlations in Eq. (40), i.e., $S_{ii}(k) = 1$, and consider electrons and ions as contributing to the k -independent inverse screening length κ_{sc} ,

$$\kappa_{sc}^2 = \kappa_e^2 + \kappa_i^2. \quad (41)$$

The electronic screening length κ_e is calculated via Eq. (6), i.e., accounting for the full quantum degeneracy of electrons. Ions can be treated classically in all cases, i.e.,

TABLE I. Possible approximations for electronic and ionic correlations in collision integral (40). The ion-ion structure factor is given by $S_{ii}(k)=1$, taken in DH approximation, or calculated by solving the HNC equations numerically. Screening in the potential is considered by both components (TCS) or only by electrons in the other cases; see Eq. (41)

Approx.	$S_{ii}(k)$	κ_{sc}^2
TCS	1	$\kappa_e^2 + \kappa_i^2$
DH	$\frac{k^2}{k^2 + \kappa_i^2}$	κ_e^2
HNC	via HNC eqs.	κ_e^2

the Debye expression $\kappa_i^2 = Z_f \mu_i e^2 / \varepsilon_0 k_B T$ is valid and used [see also Eq. (8) for electrons].

2. Ionic correlations and electronic screening

In this case we consider ionic correlations directly by calculating the ion-ion structure factor $S_{ii}(k)$ either within the simple Debye-Hückel (DH) approximation

$$S_{ii}^{\text{DH}}(k) = \frac{k^2}{k^2 + \kappa_i^2}, \quad (42)$$

or by solving the integral equations for the two-particle correlation function numerically within the HNC approximation. In this way one also takes into account higher-order ionic correlations as in a classical fluid. Because the ionic correlations are treated explicitly, only electronic screening is considered in the potential in order to avoid double counting, i.e., $\kappa_{sc} = \kappa_e$.

It is possible to include the k dependence of electronic screening effects in the inverse screening length via the RPA dielectric function as follows:

$$\kappa_e(k) = k \sqrt{\text{Re} \varepsilon_e^{\text{RPA}}(k, 0) - 1}. \quad (43)$$

In this way, the collision frequency in Born approximation, Eq. (40), converges to the same value as the LB approximation (Reinholz *et al.*, 2000) at vanishing frequency. However, we found that the k dependence is of minor importance for the results and, therefore, neglected in what follows.

The different approximations which are possible within the framework described above are summarized in Table I.

E. Bound-free transitions

In the case of very dense plasmas, the potential distribution of a given ion is influenced not only by its own bound electrons but also by the charges from neighboring atoms. The net effect is a lowering of the ionization potential (*continuum lowering*). Such lowering depends on the total number of ions that participate in the modification of the potential around a test ion, which in turn is a function of the screening distance of the Coulomb forces.

Stewart and Pyatt (1966) calculated the continuum lowering using a finite-temperature Thomas-Fermi model which reproduces both the classical Debye screening length λ_D for low density plasmas and the ion-sphere correlation length \bar{d} for high density strongly coupled systems. In their model, the lowering of the ionization potential is given by

$$\Delta E_B = \frac{Z_f e^2}{4\pi\varepsilon_0\lambda_s}, \quad (44)$$

with the effective screening length

$$\lambda_s = \frac{2}{3} \frac{Z_f^{1/3} \bar{d} (Z_f^{1/3} \bar{d} / \lambda_D)^2}{[(Z_f^{1/3} \bar{d} / \lambda_D)^3 + 1]^{2/3} - 1}. \quad (45)$$

A perturbative treatment of many-particle effects (dynamic screening and self-energy, Pauli blocking, and statistical correlations) on the eigenvalue spectrum of bound states in a plasma applying the Green's function technique, on the other hand, revealed that the continuum is lowered and that the binding energies remain almost constant (Zimmermann *et al.*, 1978). This leads to a respective lowering of the ionization energies with the density and, whenever the bound state energy merges into the continuum, to pressure ionization (Mott effect) [see Rogers *et al.* (1970) and Seidel *et al.* (1995)].

The relativistic correction for a bound-free term for an electron, initially in a state with principal quantum number n and orbital quantum number l , can be calculated analytically assuming that the final state is represented by a plane wave and that the bound states are given by simple Coulomb wave functions. In this form factor approximation, the bound-free term arising from the s th electron in the n, l configuration can then be written as

$$\tilde{S}_{ce}^{nl,s}(k, \omega) = \frac{2^{4(l+1)} n^2 (n-l-1)! (l!)^2 \sqrt{1+p^2} m_e}{2\pi^2 (n+l)! \alpha_f \hbar k Z_{nl,s}} \times [J_{nl}(1+\xi_-^2) - J_{nl}(1+1/\xi_+^2)], \quad (46)$$

where α_f is the fine structure constant, $Z_{nl,s}$ is the effective nuclear charge felt by the s th electron in the n, l shell,

$$p = \sqrt{\left(\frac{\hbar\omega}{m_e c^2} - 1 + \frac{E_{iz}^{nl,s}}{m_e c^2}\right)^2 - 1}, \quad (47)$$

with $E_{iz}^{nl,s}$ the ionization energy for the s th electron, and

$$\xi_- = \frac{n(p - k\hbar/m_e c)}{\alpha_f Z_{nl}}, \quad \xi_+ = \frac{n(p + k\hbar/m_e c)}{\alpha_f Z_{nl}}. \quad (48)$$

The shell function J_{nl} has been explicitly calculated by Schumacher *et al.* (1975), and for K -shell electrons ($n=1, l=0$) can be written as

$$J_{10}(y) = \frac{1}{3y^3}. \quad (49)$$

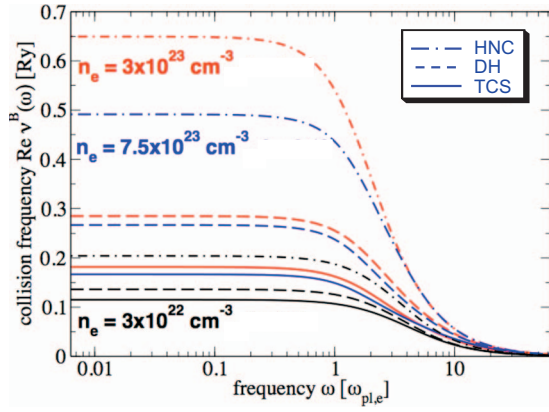


FIG. 7. (Color) Real part of the collision frequency in Born approximation using various approximations for electronic and ionic correlations in the collision integral; see Table I. Results are shown for three different electron densities. The mean ion charge is $Z_f=2$ and the plasma temperature is $T_i=T_e=12$ eV.

The full bound-free term that appears in Eq. (32) is then constructed by adding all bound electron contributions,

$$\tilde{S}_{ce}(k, \omega) = r_k \sum_{nl} \sum_s \tilde{S}_{ce}^{nl,s}(k, \omega). \quad (50)$$

The normalization constant r_k accounts for the possibility of coherent scattering and is given by

$$r_k \sim 1 - \left(\frac{|f_I(k)|}{Z_c} \right)^2. \quad (51)$$

Schumacher *et al.* (1975) showed that in the limit of small binding energies ($E_{iz}^{nl} \rightarrow 0$), the form factor approximation reduces to the well-known impulse approximation (Eisenberger and Platzman, 1970) which has been used to describe Compton scattering from static cold matter (as in synchrotron experiments).

Transitions into the continuum require $\hbar\omega > E_B$ so that the position of the Raman band is independent of k , and the respective threshold measures the ionization energy of K -shell electrons in a dense plasma. Therefore, different models for the continuum lowering ΔE_B in dense plasmas as given by Stewart and Pyatt (1966) or the improved approaches of Rogers *et al.* (1970) and Zimmermann *et al.* (1978) can, in principle, be probed by x-ray Thomson scattering.

F. Numerical results

1. Collision frequency

Figure 7 shows the real part of the dynamical collision frequency in Born approximation, Eq. (40), treating electronic and ionic correlations in the collision frequency in the approximations summarized in Table I [see Thiele *et al.* (2006) and Höll *et al.* (2007)]. Three densities have been investigated. Up to electron densities reaching solid conditions and Fermi degeneracy, the collision frequency increases with the density which is due to increased coupling. However, for the highest den-

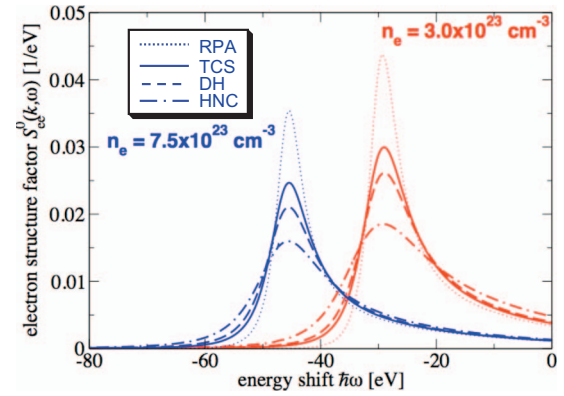


FIG. 8. (Color) Electron feature of the dynamic structure factor for compressed (blue) and uncompressed (red) beryllium. The RPA (collisionless plasma) result is compared to the BMA result by taking into account the ionic structure factor and the inverse screening length according to the models specified in Table I. Further parameters: $Z_f=2$, $T_e=T_i=12$ eV, photon energy $\hbar\omega_0=2960$ eV (Cl-Lyman- α), scattering angle $\theta=40^\circ$ for red curve and $\hbar\omega_0=6180$ eV (Mn-He- α), scattering angle $\theta=25^\circ$ for blue curve.

sity of $n_e=7.5 \times 10^{23} \text{ cm}^{-3}$ that represent conditions reached in experiments with compressed beryllium, a reduction in the collision frequency is observed which is due to Pauli blocking in the expression for the collision frequency, Eq. (40). This is more than balanced by considering ionic correlations in DH and HNC approximations. At frequencies larger than the electron plasma frequency ω_{pl} , collisions become less effective.

In the static limit $\omega \rightarrow 0$, the collision frequency $\nu(\omega)$ is connected with the dc electrical conductivity via Eq. (24),

$$\sigma_{dc} = \frac{\epsilon_0 \omega_{pl}^2}{\nu(\omega=0)}. \quad (52)$$

This quantity can be evaluated beyond the BMA, e.g., in the GDW approximation (see Sec. III.D), so that besides dynamic screening effects in first Born approximation strong collisions are also accounted for with respect to a statically screened potential (Röpke, 1998). However, the consideration of the full dynamics of the collision frequency is an important issue when calculating the dynamic structure factor [see Redmer *et al.* (2005)].

2. Electron feature of the dynamic structure factor

Figure 8 shows the electronic contribution to the dynamic structure factor $S_e(k, \omega) = Z_f S_{ee}^0(k, \omega)$ for uncompressed ($n_e=3 \times 10^{23} \text{ cm}^{-3}$) and compressed ($n_e=7.5 \times 10^{23} \text{ cm}^{-3}$) beryllium, probed with a photon energy of $\hbar\omega_0=2960$ eV (Cl-Lyman- α) at a scattering angle of $\theta=40^\circ$ as a function of the energy shift from the incident photon energy. Results for compressed beryllium are calculated for higher energy x rays and at a scattering angle of 25° . The collisionless (RPA) calculation is shown as a thin dotted line, while the thick full curves show the results obtained using the BMA and TCS as

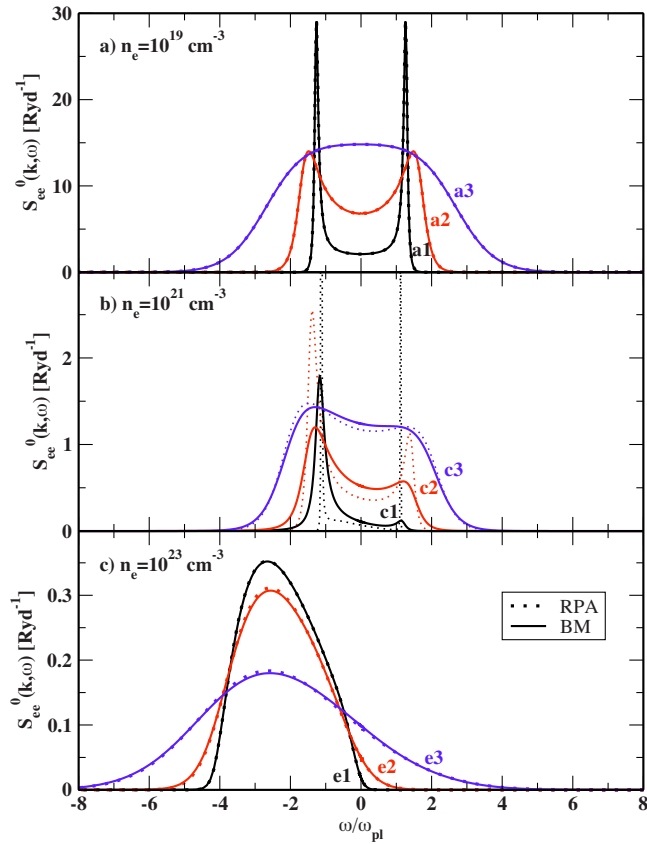


FIG. 9. (Color online) Calculations of the electron feature for the dynamic structure factor according to Gregori, Glenzer, Rozmes, *et al.* (2003) and Redmer *et al.* (2005) shown for various plasma conditions, see Table II. RPA results are compared with the BMA that includes collisions according to TCS.

outlined in Sec. III.D. The dashed and dash-dotted curves correspond to the electronic and ionic correlation models in the collision integral specified in Table I. The energy shift increases with the density independent of the approximation. Inclusion of collisions in BMA leads to significant damping of the plasmon resonance. When

including ion-ion correlations in the DH and HNC models, scattering is increased and the damping is strongest.

The variation in the electron contribution to the dynamic structure factor is shown in Fig. 9 for a wide range of plasma densities and temperatures [see also Gregori, Glenzer, Rozmus, *et al.* (2003) and Redmer *et al.* (2005)]. We consider weakly nonideal ($\Gamma \ll 1$) and nondegenerate ($\Theta \gg 1$) plasmas in sets a_i , the warm dense matter region with strong coupling ($\Gamma \sim 1$) and partial degeneracy ($\Theta \gtrsim 1$) in sets c_i , and the strongly correlated quantum liquid ($\Gamma \gtrsim 1, \Theta \leq 1$) in sets e_i (see Table II).

The parameters a_i are accessible with optical lasers, the parameters c_i with extreme ultraviolet (EUV) light, and the parameters e_i with x-ray sources. Figure 9 shows that for the cases a_i collisions are less important than for higher densities, i.e., the cases c_i and e_i . For the parameter sets c_i , the influence of collisions is largest. Pauli blocking prevents the collisions to have a major influence in the case of highest densities, i.e., sets e_i .

The well-known form for the dynamic structure factor in RPA is recovered by the calculations within the BMA. For small recoil energy (compared to the thermal energy) as in case a_i two symmetric peaks are found which are located slightly above the plasma frequency. With increasing recoil energy, i.e., shorter wavelengths, these peaks become asymmetric and the redshifted peak is most pronounced. This can be used to infer the temperature since the underlying detailed balance relation [see Eq. (18)] is independent of the theoretical approximations made in evaluating the dielectric function and/or the dynamic collision frequency. The influence of collisions is most effective in conditions that can be probed with extreme ultraviolet radiation at densities around $n_e = 10^{21} \text{ cm}^{-3}$, i.e., for sets c_i . For these parameters it can be seen that collisions broaden the structure factor and the position of the peak is redshifted. This domain of nearly solid densities can be probed with FEL facilities [see Höll *et al.* (2007)].

TABLE II. Parameters for the calculation of the electron feature of the dynamic structure factor: Free-electron density n_e , plasma frequency ω_{pl} , probe wave length λ_0 , temperature T_e , coupling (Γ), and degeneracy (Θ) parameter as well as scattering parameter α ; the scattering angle is always $\theta_S = 60^\circ$.

	n_e (cm^{-3})	ω_{pl} (eV)	λ_0 (nm)	T_e (eV)	Θ	Γ	α
a1				200	11800	0.0025	2.5
a2	10^{19}	0.117	532	600	35500	0.0008	1.5
a3				3000	177000	0.0002	0.7
c1				0.5	1.371	4.642	4.0
c2	10^{21}	1.174	4.13	2.0	5.485	1.161	2.0
c3				8.0	21.943	0.290	1.0
e1				0.8	0.10	13.468	2.0
e2	10^{23}	11.742	0.26	3.0	0.38	3.591	1.0
e3				13.0	1.65	0.829	0.5

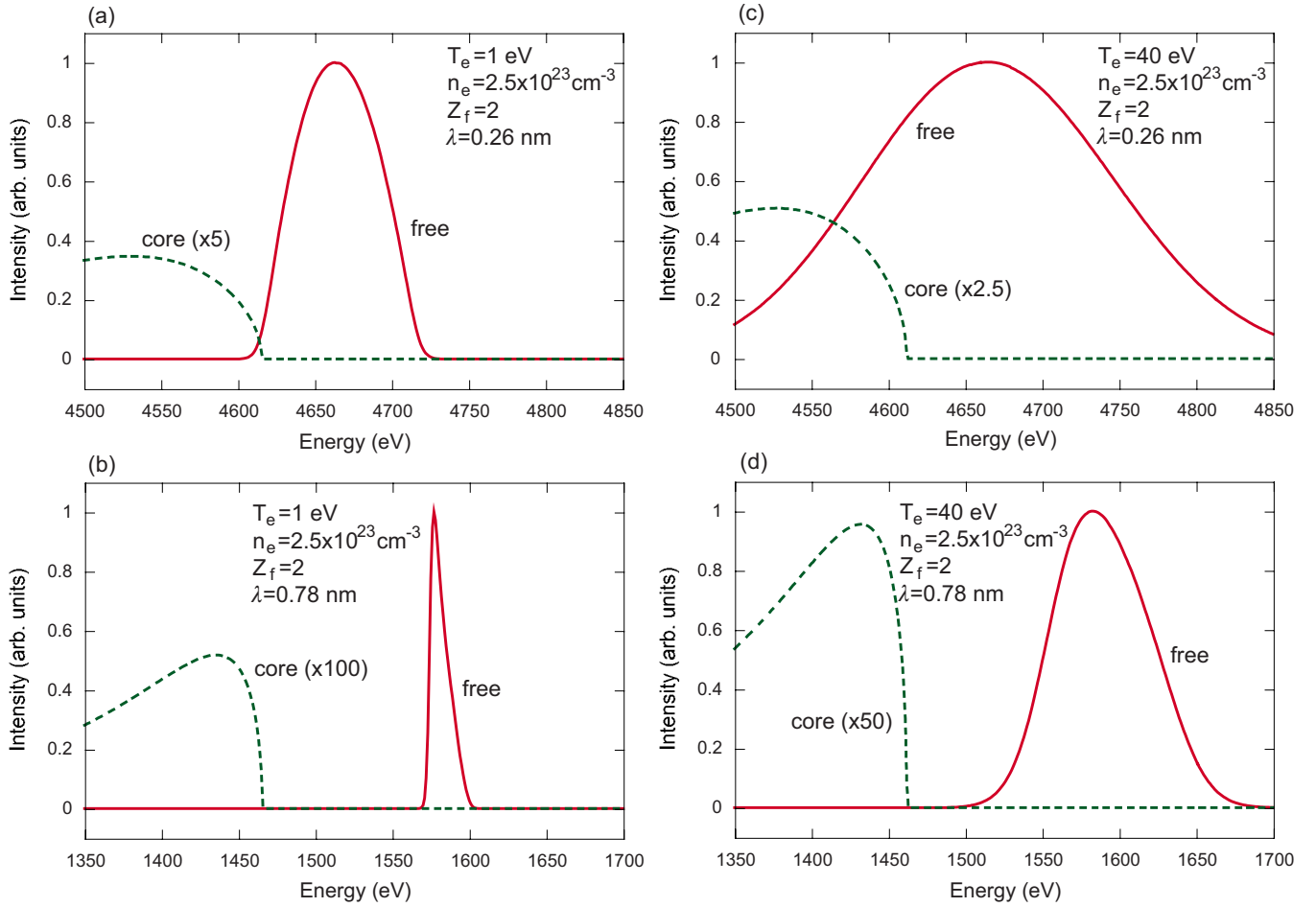


FIG. 10. (Color online) Comparisons between the RPA dynamic structures arising from free and core electrons are shown according to Sec. III.E and [Gregori, Glenzer, Rozmus, et al. \(2003\)](#) for the case of a beryllium plasma. At $T_e=1$ eV, beryllium is assumed in its normal state, Z_f consists only of conduction electrons with a K -shell ionization potential $E_B=111.5$ eV. At $T_e=40$ eV, beryllium is assumed doubly ionized Z_f includes only free electrons with $E_B=159.5$ eV. The scattering angle is $\theta=160^\circ$. The scattering parameter is (a) $\alpha=0.46$, (b) $\alpha=1.36$, (c) $\alpha=0.23$, and (d) $\alpha=0.67$.

3. Bound-free spectrum

Figure 10 displays the contributions of free and core electrons to the dynamic structure factor for a solid-density beryllium plasma as derived by [Gregori, Glenzer, Rozmus, et al. \(2003\)](#). For both x-ray wavelengths ($\lambda_0=0.26$ and 0.78 nm) as well as for both temperatures ($T_e=1$ and 40 eV) considered, the contribution from transitions of core electrons into the continuum is small compared to the scattering signal of free electrons. Furthermore, the width of the respective Raman band is of the order or even larger than the Compton band contributing to its low energy wing.

4. Ion feature

Figure 11 shows the static ion-ion and electron-ion structure factors $S_{ii}(k)$ and $S_{ei}(k)$ for uncompressed and compressed beryllium as function of the wave number k calculated in the HNC scheme as outlined by [Schwarz et al. \(2007\)](#). In addition, the simple DH result for $S_{ii}(k)$ is shown as well as the total elastic contribution S_i to the

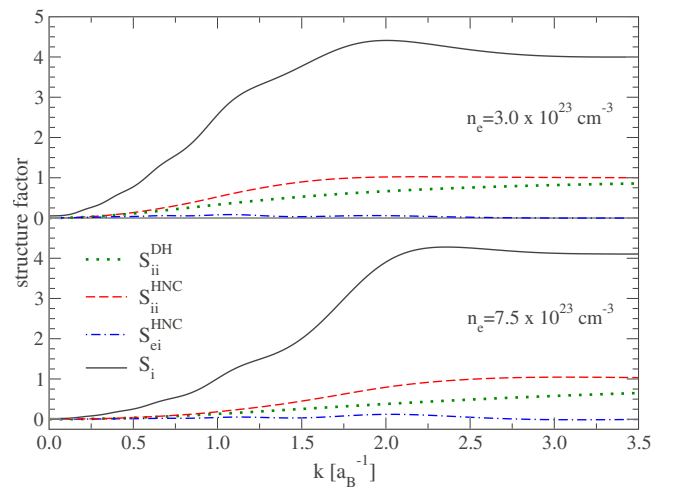


FIG. 11. (Color online) Static ion-ion and electron-ion structure factors for uncompressed ($n_e=3.0 \times 10^{23} \text{ cm}^{-3}$) and compressed beryllium ($n_e=7.5 \times 10^{23} \text{ cm}^{-3}$) calculated in DH (S_{ii}) and HNC approximation (S_{ii} and S_{ei}) for $Z_f=2$ and $T_e=T_i=12$ eV. Curves: Total elastic contribution to the dynamic structure factor $S_i=[Z_b+\sqrt{Z_f}S_{ei}(k)/S_{ii}(k)]^2S_{ii}(k)$ [see Eq. (35)].

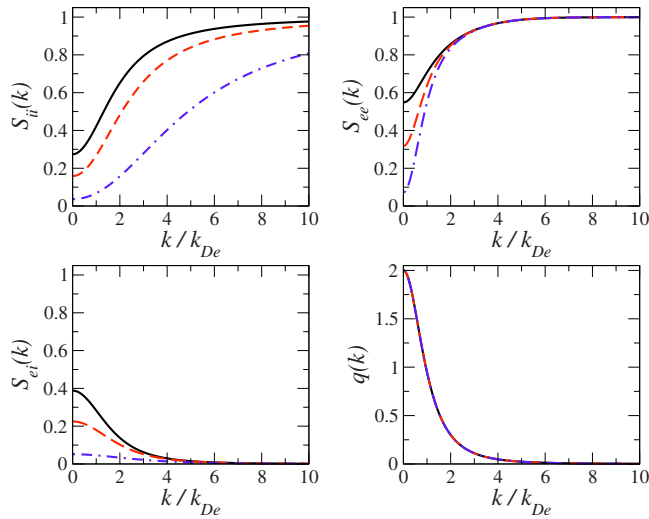


FIG. 12. (Color online) The calculated static structure factors $S_{cd}(k)$ and screening charges $q(k)$ for a beryllium plasma with $Z_A=4$ at $n_e=2.5 \times 10^{23} \text{ cm}^{-3}$, $Z_f=2$, and $T_i/T_e=1$ (solid line), $T_i/T_e=0.5$ (dashed line), $T_i/T_e=0.1$ (dash-dotted line). The transfer momentum k is normalized with respect to the inverse electron Debye screening length $k_{De}=1/\lambda_D$ [see Eq. (8)]. From Gregori, Glenzer, and Landen, 2006.

dynamic structure factor according to Eq. (35). Further parameters are $Z_f=2$ and $T_i=T_e=12 \text{ eV}$.

The HNC approximation also takes into account higher-order ion-ion correlations as in a classical liquid, whereas the DH result is only valid for low densities. Electron-ion correlations become more pronounced with increasing density as expected. The total elastic contribution to the dynamic structure factor is sensitive with respect to an analysis of measured Thomson scattering spectra (see Sec. V.C).

The dependence of the dynamic structure factor and screening function on k is displayed in Fig. 12 from Gregori, Glenzer, and Landen (2003). The ion-ion and electron-electron structure factors approach unity for large k while electron-ion correlations decrease correspondingly. In this limit, the resulting screening function $q(k)$ [see Eq. (35)] is rapidly approaching zero and the ion feature $S_i(k) \sim Z_b^2$. Also shown are the results for nonequilibrium plasmas relevant for ultrashort excitation processes and relaxation phenomena.

The value of $S_{ii}(k)[f_i(k)+q(k)]^2$ at small values of k is small in the limit of a neutralizing electron background such as described by one component plasma (OCP) models or weak electron-ion interaction potentials. In this case, the weak electron-ion interaction is described by small values of $q(k)$. In addition, cold ions in the presence of uniform electron background arrange to minimum electrostatic potential lattice (for ion Debye length smaller than the interparticle spacing) and correlations on spatial scales longer than the interparticle spacing are reduced (see Fig. 12 for small values of k or T_i/T_e). Thus, for latticelike structures the scattering is coherent and spatial uniformity results in weak (elastic) scattering amplitudes with exception of Bragg peaks. On

the other hand, strong interaction potentials enhance correlations over large scales leading to high elastic scattering amplitudes.

The influence of the ion correlations on measured Thomson scattering intensities is further outlined in Fig. 26 for beryllium and Fig. 31 for lithium. Ionic and electronic correlations are connected in the approach of Chihara (1987, 2000) via the screening function $q(k)$ and rely on defining bound and free electrons with a chemical picture model. Future studies will allow a first-principles approach to the ion-ion static structure factor by *ab initio* quantum molecular dynamics simulations which treat electronic and ionic correlations in a strict physical picture by combining finite-temperature DFT for the electrons and classical molecular dynamics for the ions, cf. Desjarlais *et al.* (2002), Bonev, Militzer, and Galli (2004), Garcia Saiz, Gregori, Gericke, *et al.* (2008), Garcia Saiz, Gregori, Khattak, *et al.* (2008), and Wunsch, Vorberger, and Gericke (2009).

G. Theoretical spectra

In order to generate theoretical scattering spectra comparable to the data measured with Thomson scattering experiments, we proceed as follows. First, we calculate the collision frequency in the range $[-100\omega_{pl}, 100\omega_{pl}]$ on a logarithmic grid; see Eq. (40). Second, we generate the free electron contribution $S_e(k, \omega) = Z_f S_{ee}^0(k, \omega)$ in the range $[-10\omega_{pl}, 3\omega_{pl}]$; [see Eqs. (17) and (25)].

Third, we take into account the finite resolution of the detector as well as the finite bandwidth of the probe beam. The calculated spectra have to be convoluted with an appropriate weighting function $g(\omega)$. Here we use a Gaussian of the form

$$g(\omega) = \frac{1}{\sqrt{2\pi}\sigma} \exp\left(-\frac{\omega^2}{2\sigma^2}\right). \quad (53)$$

The variance σ^2 is fixed by $\sigma = 0.425 \times \text{FWHM}_{\text{tot}}$, with the total full width at half maximum FWHM_{tot} given by $\text{FWHM}_{\text{tot}}^2 = \text{FWHM}_{\text{detector}}^2 + \text{FWHM}_{\text{probe}}^2$. Finally, the elastic feature $S_i(k)$ via Eq. (35) and if necessary bound-free transitions are added.

In summary, theoretical spectra result by computing the following expression using Eq. (32):

$$S(k, \omega) = \frac{1}{\sqrt{2\pi}\sigma} \int_{-\infty}^{\infty} S_{ee}(k, \omega') \times \exp\left(-\frac{(\omega - \omega_0 - \omega')^2}{2\sigma^2}\right) d\omega'. \quad (54)$$

Theoretical x-ray Thomson scattering spectra have been calculated by Gregori, Glenzer, Rozmus, *et al.* (2003) with the dynamic structure factor $S(\mathbf{k}, \omega)$ for beryllium targets with $Z_A=4$ at various temperatures, densities, and ionization stages. The results are shown in Fig. 13. The probe radiation is $E=4.75 \text{ keV}$ and the scattering angle is $\theta=160^\circ$.

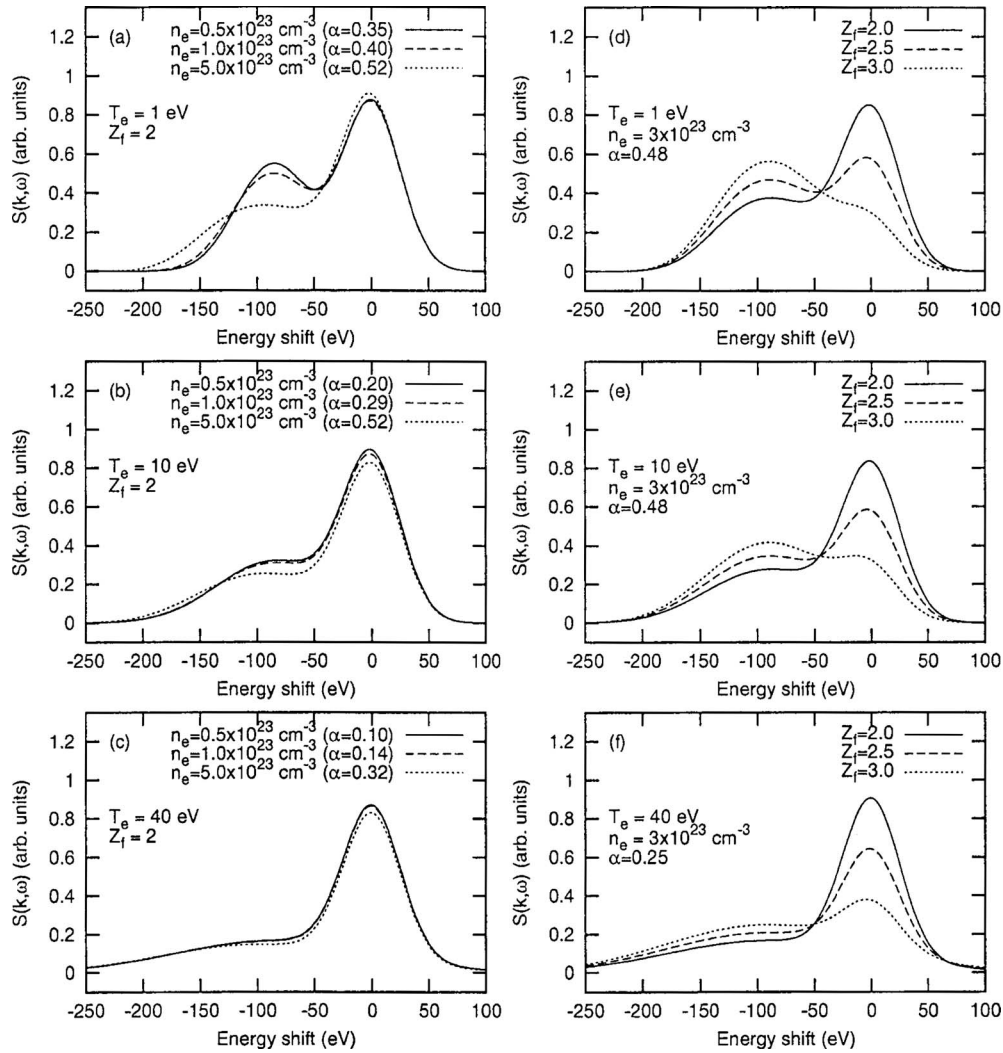


FIG. 13. Theoretical x-ray Thomson scattering spectra calculated with the dynamic structure factor $S(\mathbf{k}, \omega)$ for beryllium targets with $Z_A=4$ at various temperatures, densities, and ionization stages. The probe radiation is $E=4.75$ keV and the scattering angle is $\theta=160^\circ$. From [Gregori, Glenzer, Rozmus, *et al.*, 2003](#).

The temperature and density dependent Thomson scattering spectrum is shown for beryllium in Figs. 13(a)–13(c) for $Z_f=2$. The inelastic Compton scattering feature is strongly broadened with increasing temperature. Figures 13(d)–13(f) show that the elastic scattering feature is strongly reduced relative to the inelastic scattering feature with increasing Z_f . In isochorically heated matter of known mass density, the electron density can be inferred from the intensity ratio. For liquid hydrogen targets a similar analysis has been performed by [Höll *et al.* \(2007\)](#) for x-ray Thomson scattering experiments using FELs.

IV. EXPERIMENTAL TECHNIQUES

A. Design of scattering experiments

In the first x-ray Thomson scattering experiments at the Omega laser, submillimeter scale samples of light elements, e.g., beryllium or carbon, have been heated volumetrically using either multi-keV L -shell x rays

from laser-illuminated solid target plasmas ([Glenzer, Gregori, Lee, *et al.*, 2003](#); [Gregori *et al.*, 2004](#); [Glenzer, Landen, *et al.*, 2007](#)) or by direct-drive compression ([Sawada *et al.*, 2007](#); [Lee, 2008](#)). A separate multi-keV line radiator, with adequate energy to penetrate through the dense sample, has been produced from a second delayed laser plasma providing the spectrally narrow x-ray probe for x-ray Thomson scattering before the plasma sample cools or disassembles. Scattered photons in near forward scattering and near backscattering geometries have been collected and spectrally dispersed by high reflectance crystal spectrometers coupled to a gated framing camera, measuring spectra with a temporal resolution of 80 ps. Approximately 10^{14} x-ray probe photons have been delivered to the sample and $>10^5$ photons have been detected for high-quality single shot experiments. Subsequently, larger curved crystal spectrometers and higher efficiency detectors have been employed at the Titan ([Kritcher, Neumayer, Castor, *et al.*, 2008](#)), LULI 2000 ([Ravasio *et al.*, 2007](#)), or Vulcan ([Garcia Saiz, Gregori, Gericke, *et al.*, 2008](#)) lasers allowing measure-

ments with significantly lower numbers of x-ray photons; at 10^{12} photons at the sample.

The use of unfocussed laser-produced x-ray probe radiation requires that extended fairly homogeneous plasma samples are produced by energetic drivers. Furthermore, the quasimonochromatic x-ray probe must be produced efficiently and placed in close proximity to the sample. At a distance of 0.3–3 mm these two independent laser plasmas will avoid interactions among themselves. At this distance, the sample subtends a solid angle of $10^{-2} \leq d\Omega \leq 2$ sr. Thus, it is necessary to heat or compress a dense plasma sample homogeneously over a surface diameter of $d=0.35$ mm to match the solid angle and to use the maximum amount of x-ray probe photons provided by the laser plasma. Moreover, to maximize the probability for a scattering process and to achieve a high scattering fraction it is advantageous to heat or compress the dense plasma over a length of order of the diameter $\ell=0.4$ mm, resulting into a total volume of the dense plasma of $V=5 \times 10^{-5}$ cm³.

Heating such a volume of solid density matter with a mass density on the order of 1 g cm⁻³ to temperatures of several eV requires a driver that delivers about 10 eV/atom. For example, the total number of atoms in a beryllium sample with mass density of 1.85 g cm⁻³, $Z_f=1$, and $A=9.012$ amu is $N=n_e V=N_A(Z/A)\rho V=6 \times 10^{18}$. Here $N_A=6.022 \times 10^{23}$ mol⁻¹ is the Avogadro constant (or Loschmidt's number). To heat this sample requires that 10 J of energy deposited resulting in a total energy density of 2×10^5 J cm⁻³, thus requiring a high energy density physics facility.

In experiments at the Omega or Titan laser, a uniform plasma of 50 μ m scale length to about 1 mm has been produced. Shields have been applied to define the scattering volume and to avoid scattering from the nonuniform part of the target. In addition, they also prevent a direct view of the x-ray probe plasma by the detector. At Omega, up to 1 J of x-ray energy has been applied for probing, which itself heat the sample; experiments have observed heating up to about 2 eV. With the use of focused x-ray beams (e.g., from FELs), these volume and heating restrictions for probing the dense plasma sample will be mitigated by achieving a scattering volume as small as 2 μ m in diameter, while the length of the scattering volume can be chosen to achieve the required scattering fraction. Thus, these x-ray sources will allow a lower energy driver for producing a smaller scale-length plasma sample.

The first angularly resolved x-ray diffraction experiments on dense plasmas by Riley *et al.* (2000) and Riley, Weaver, *et al.* (2002) employed two apertures to collimate the incident x rays and to observe scattering from a free-standing shocked foil at different angles on multiple shots. The x-ray Thomson scattering experiments of Glenzer, Gregori, Lee, *et al.* (2003), Glenzer, Gregori, Rogers, *et al.* (2003), Gregori *et al.* (2004), and Glenzer, Landen, *et al.* (2007) used shields to restrict the field of view of the spectrometer to measure scattering spectra

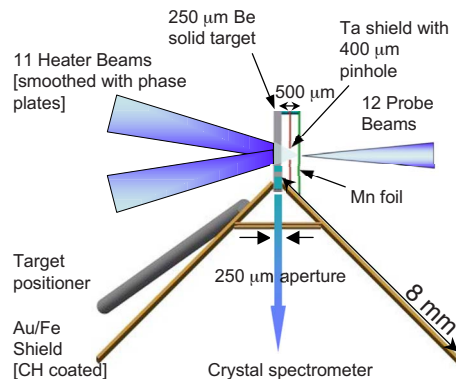


FIG. 14. (Color online) Schematic of x-ray scattering target after Sawada *et al.* (2007) and Lee *et al.* (2009). A pinhole is used for collimating the x-ray probe radiation. Shields and a 250 μ m aperture limit the field of view of the x-ray spectrometer to the compressed material.

from the isochorically heated beryllium. In recently designed experiments, these techniques have been combined.

Figure 14 shows the scattering target developed by Sawada *et al.* (2007) for x-ray Thomson scattering measurements on shock-compressed matter. This target platform has been subsequently employed by Lee *et al.* (2009) for use with different sample materials and scattering angles. A Ta shield with a pinhole restricts the solid angle to $d\Omega_{x \text{ ray}} \approx 2$ sr so that the x rays interact with a sample surface area of 0.005 cm⁻² and a volume of $V \approx 10^{-4}$ cm³. The 8 mm-long Au/Fe shields restrict the field of view of the x-ray spectrometer to the beryllium sample and prevent the Mn plasma from moving into the field of view at the time when the scattering spectrum is measured with a gated detector.

Because of the relatively small scattering signals, it is important to avoid the x-ray fluorescence of filters and shields (Tertian and Claisse, 1982) induced by direct bremsstrahlung emission or high energy electrons from laser-plasma interactions. Fluorescence by inner-shell $K\text{-}\alpha$ and $K\text{-}\beta$ transitions has been investigated by Kyrala and Workman (2001). The incident spectral photon flux density $I_\lambda(0)$ is measured in units of photons per unit bandwidth interval per unit area and are attenuated at a depth x according to Beer's law $I_\lambda(0)d\lambda e^{-\mu_\lambda \rho x}$. Here $\mu_\lambda = \mu_\lambda^s + \mu_\lambda^p + \mu_\lambda^\pi$ is the total absorption coefficient at the wavelength λ due to scattering, photoelectric effect, and pair production. At the depth x the photons in the beam are further depleted in a sheet dx , $I_\lambda(0) d\lambda e^{-\mu_\lambda \rho x} \nu_\lambda \rho dx$. Only photons absorbed by the photoelectric effect described by μ_λ^p lead to fluorescence, and the fraction of vacancies in the K shell that subsequently lead to K shell fluorescence is determined by the jump factor in the photoelectric absorption coefficient at the K edge, r_k . This leads to the fluorescence of a filter of thickness h in direction of the detector of

$$B_K(h)d\lambda = \left[\frac{r_k - 1}{r_k} \right] c\omega_k \left[\frac{\mu_\lambda^p}{\mu_\lambda - \mu_k} \right] \times [1 - e^{-\rho h(\mu_\lambda - \mu_k)}] I_\lambda(0) d\lambda e^{-\mu_k \rho h}. \quad (55)$$

The fluorescence at the wavelength of the K lines is denoted by μ_k . With absorption coefficients from [Henke et al. \(1982, 1993\)](#), estimates by [Kyrala and Workman \(2001\)](#) showed that the flux in high- Z filters can be significant reaching up to the same order of magnitude as the incident radiation. In scattering experiments where the photon flux is of order 10^{-6} of the primary x-ray probe radiation, this signal would be a significant source of high background and noise levels. Target shields with coatings of low- Z plastic as well as alternating materials with appropriate K edges have been shown to be effective for avoiding fluorescence radiation. In addition, free-standing crystals have been applied by [Kritcher, Neumayer, Castor, et al. \(2008\)](#) to avoid fluorescence in the spectrometer housing material.

Collimating the probe x rays and restricting the scattering volume is also important for accurately defining the scattering angle, to avoid sampling a large spread of \mathbf{k} vectors and to achieve partial spatial coherence of the source ([Wolf, 1987](#)). In noncollective scattering experiments, broadening of spectral features has been kept small compared to the thermal broadening of the Compton line by choosing $\Delta k/k < 0.2$; cf. Eqs. (11) and (14). For collective scattering experiments, [Gregori, Tommasini, et al. \(2006\)](#) estimated the effect of an extended source.

The coherence length in the plasma defined by Eq. (4), λ^* , will be decreased due to additional path length from light rays on opposite ends of the source. Thus, the scattering angle in Eq. (4) must be replaced by $\theta + \Delta\theta/2$ with $\Delta\theta$ the angular extent of the source as seen by each point in the scattering volume. The coherence length at the sample from an extended source of length L_S can then be estimated from the condition $\Delta L_S \Delta k \sim 1$ with $\Delta k_0 = k_0 \Delta\theta/2$. These geometric considerations lead to

$$\alpha \geq 1 + \frac{\Delta\theta}{2\theta} \quad (56)$$

to observe collective scattering features.

Finally, the size of the scattering volume determines the amount of bremsstrahlung emission from the dense plasma measured by the x-ray scattering detector. The emitted power by (free-free) bremsstrahlung emission $P_{ff}(\hbar\omega)$, at radiation energy $\hbar\omega$ into the energy bandwidth $d(\hbar\omega)$, solid angle $d\Omega$, and volume V has been discussed by [Griem \(1997\)](#), and assuming radiation transport effects not to be important

$$P_{ff}(\hbar\omega)d(\hbar\omega) = \frac{32}{3} \left(\frac{\pi}{3} \right)^{1/2} r_0 c \left(\frac{E_H}{k_B T_e} \right)^{1/2} \times Z^2 n_i n_e g e^{-\hbar\omega/k_B T_e} d(\hbar\omega) \quad (57)$$

with E_H the ionization energy of hydrogen. High density corrections by [Fortmann et al. \(2006\)](#) showed that the gaunt factor g varies by factors of 2–3 for the dense

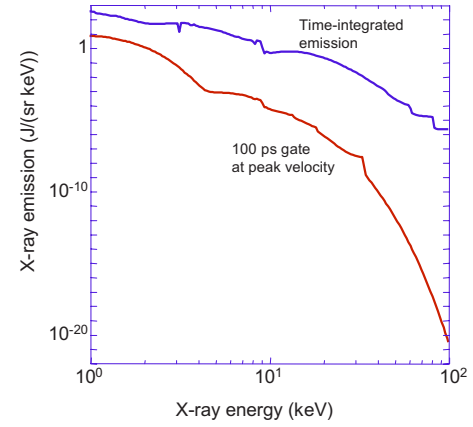


FIG. 15. (Color online) X-ray bremsstrahlung emission as function of radiation energy from dense capsule implosion conditions. The time-integrated emission is compared with the emission during a 100 ps time interval at maximum implosion velocity.

plasmas of interest. Thus, for plasma samples with increasingly higher densities and temperatures, x-ray sources with higher flux or energy are required to penetrate through the dense matter and to obtain larger scattering signals compared to the bremsstrahlung emission.

Equation (57) further indicates that bremsstrahlung emission in the x-ray region has to be accounted for in conditions with high electron temperatures. For dense hydrogen plasmas, [Fortmann et al. \(2006\)](#) showed that a free-electron laser source at 80 eV provides a factor of ten larger scattering signal above the bremsstrahlung emission. On the other hand, for high temperature gas-bag plasmas, [Gregori, Glenzer, Chung, et al. \(2006\)](#) chose a high energy x-ray probe, the Zn He- α probe radiation at 9 keV, to obtain a larger signal from x-ray scattering than from bremsstrahlung emission.

Figure 15 shows the calculated bremsstrahlung emission from an inertial confinement fusion capsule implosion experiment by [Hatchett \(2008\)](#). This calculation includes radiation transport and assumes a field of view of 300 μm in diameter as well as a low concentration of deuterium (H:D:T=1:0.0025:1) to limit the neutron yield. These experiments will allow probing extremely dense conditions. The time-integrated emission is shown together with the emission gated over 100 ps at about peak implosion velocity. Quantitative estimates provided in Sec. IV.E indicate that a gated detector enables measurements in this regime using a powerful x-ray source as described in Sec. II.

B. X-ray probe requirements

For x-ray Thomson scattering experiments with laser-produced x-ray sources, it is important to develop conditions with high x-ray conversion efficiency. In this section, the x-ray yield Y of a laser source is defined as the number of photons that are produced per 1 J of incident laser energy and in the full sphere. With E_L the total

laser energy on target the total number of photons produced is YE_L . The x-ray conversion efficiency is then defined as $\eta_x = Yh\nu$, and is a dimensionless parameter. The important quantity is the number of x-ray photons in a single x-ray spectral line produced in a single laser shot. In most cases, the source size is sufficiently small to fulfill the requirements outlined in Sec. IV.A. These sources must further provide a narrow bandwidth of $\Delta E/E \approx 0.01$ for noncollective scattering (Landen, Glenzer, *et al.*, 2001) and $\Delta E/E \approx 0.002$ for collective scattering (Urry *et al.*, 2006), respectively. While FEL x-ray sources are designed *ab initio* to provide optimum spectral and temporal properties with fixed photon numbers for x-ray Thomson scattering applications, laser-produced plasmas require development to obtain the desired properties.

For example, probing solid-density beryllium plasmas at temperatures of 50 eV and electron density of $n_e = 3 \times 10^{23} \text{ cm}^{-3}$ in backscatter geometry, $\theta = 125^\circ$, and with a moderate x-ray energy source such as titanium He- α at $E_0 = 4.75 \text{ keV}$ will access a scattering vector of $|\mathbf{k}| = 4 \times 10^{-10} \text{ m}^{-1}$; cf. Eq. (4). In this case, with $\alpha = 0.3$ the experiment results in noncollective scattering. The Compton feature will be shifted from E_0 to $\Delta E_C = \hbar^2 k^2 / 2m_e = 70 \text{ eV}$, and the spectral broadening by thermal motion will result in a width of 200 eV. To resolve this feature, an x-ray probe bandwidth of 40 eV such as provided by the titanium He- α spectrum is sufficient. Specifically, the He- α probe spectrum consists of the resonance, intercombination, and dielectronic satellite lines. On the other hand, for forward scattering measurements on plasmons, a spectral resolution of 6 eV is necessary and has been provided, e.g., by the chlorine Ly- α doublet or titanium K- α transitions.

Plasmon measurements suffer from the fact that these features are weak and, when using He- α or Ly- α probes, elastically scattered dielectronic satellite lines can blend with the plasmon signal. Temporal gating is required to minimize the satellite signal which is typically emitted late in time during the plasma evolution after the laser beams that produce the x-ray probe are turned off. When applying a gated detector, the contributions from these unwanted spectral features have been shown to be $\leq 5\%$ of the main chlorine Ly- α transitions; cf. Fig. 22. In addition, measurements at high density, such as performed by Lee *et al.* (2009), are advantageous providing plasmon features separated sufficiently from the He- α or Ly- α probe energy where no satellite features exist. Thus, for collective scattering, short-pulse laser-produced K- α radiation has the advantage over long-pulse laser-produced He- α or Ly- α transitions because no spectral features exist on the red wing of the K- α spectral line.

A large body of experimental and theoretical studies has investigated the x-ray conversion efficiency from laser to x-ray photons by laser-irradiating solid targets with nanosecond pulses. He- α and Ly- α x rays are emitted by highly ionized heliumlike and hydrogenlike atoms in ablation plasmas that are heated by inverse brems-

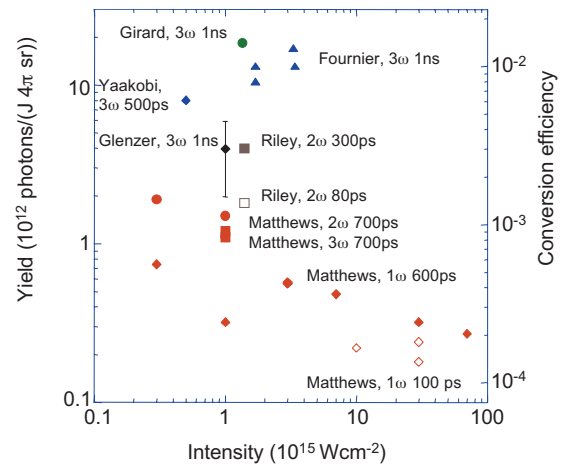


FIG. 16. (Color) X-ray yield and x-ray conversion efficiency for the titanium He- α x-ray emission at 4.75 keV as function of laser intensity from various studies (see text). A typical error bar of 50% in conversion efficiency due to uncertainties of the absolute detector calibration, crystal reflectivity, and shot-to-shot reproducibility is shown.

strahlung absorption. These studies have been reviewed by Kauffman (1991). They are aimed primarily at developing x-ray backlighter sources for radiography (Molitoris *et al.*, 1992; Hammel *et al.*, 1993) where the requirements on x-ray bandwidth and spectral purity is less stringent than for scattering applications. Yaakobi *et al.* (1981), Matthews *et al.* (1983), Kodama *et al.* (1986), Philion and Hailey (1986), and Urry *et al.* (2006) studied the dependence of the number of x-ray photons on laser color, pulse length, intensity, and energy. In addition, effects of polarization and angle of incidence have been studied by Tallents *et al.* (1990) and Kyrala *et al.* (1992). For 4–10 keV He- α and Ly- α x rays, a conversion efficiency of $0.0005 < \eta_x < 0.01$ has been measured.

Figure 16 shows the dependence of the conversion efficiency and x-ray yield on laser intensity for the titanium He- α transition. The experiments on solid-density disk targets by Matthews *et al.* (1983) showed $\eta \approx 10^{-3}$, roughly corresponding to 10^{12} titanium He- α (4.75 keV) x-ray photons per 1 J of incident laser energy and into 4π sr. These data have been reproduced by Yaakobi *et al.* (1981), Riley, Woolsey, *et al.* (2002), and Glenzer, Gregori, Rogers, *et al.* (2003) to within about a factor of 2–5. Furthermore, a linear scaling with laser energy and weak dependence on pulse length has been measured. The latter has also been observed by Riley, Woolsey, *et al.* (2002); they reported a factor of 2 variation in conversion efficiency when increasing the laser pulse width from 80 to 300 ps. While some discrepancies exist among the various studies, a strong dependence on laser frequency for low energy x rays ($< 4 \text{ keV}$) has been observed with up to an order of magnitude higher conversion efficiency measured with 351 nm (3ω) compared to 1053 nm (1ω) laser irradiation.

Girard *et al.* (2005) showed further improvements in conversion efficiency, reaching values in excess of 10^{-2} by employing a laser prepulse to generate an extended

ablation plasma before heating with a high intensity pulse. Extended plasma sources such as under dense aerogels (Fournier *et al.*, 2004, 2006), gas targets (Back *et al.*, 2001, 2003), and gas jets (Kugland *et al.*, 2008) have also been shown to improve the x-ray conversion efficiency. For titanium He- α emission, Fournier *et al.* (2004) reported a conversion efficiency of about 1%. Further, recent studies on under dense targets indicate agreement with radiation-hydrodynamic modeling. To date, extended under dense sources have not been tested for scattering experiments; x-ray scattering probes have been solely produced by laser-foil interactions.

A threshold for the onset of x-ray yield has been measured depending on the x-ray transition and energy. For example, the threshold intensity for 4.75 keV titanium He- α is $I = 2 \times 10^{14} \text{ W cm}^{-2}$, increasing to $I \approx 10^{16} \text{ W cm}^{-2}$ for 9 keV Zn He- α radiation. As shown in Fig. 16, further increasing the laser intensity results in decreasing x-ray yield due to decreased coupling with the onset of laser-plasma interaction instabilities. This trend has been reproduced for other elements emitting below 10 keV up to the Zn He- α line (Workman and Kyrala, 2001). Generally, all studies of thermal He- α or Ly- α sources with laser-irradiated foils show a strong reduction with increasing x-ray energy. For example, Workman and Kyrala (2001) and Ruggles *et al.* (2003) showed a conversion efficiency of (0.01–0.2)% for 9 keV Zn He- α radiation compared to a range of (0.1–1)% for Ti radiation at 4.75 keV.

In contrast to these He- α and Ly- α sources, irradiating targets with $Z > 20$ with short-pulse lasers results in K - α conversion efficiencies that are almost constant or slightly increasing with increasing K - α x-ray energy. With increasing Z , radiation processes dominate over nonradiative Auger processes and fluorescence x rays are emitted by inner-shell transitions in relatively cold atoms where the electron holes are created by interactions with fast electrons from short-pulse laser interactions with the solid target. These studies have been reviewed by Park *et al.* (2006). In general, after optimization of laser energy, power, polarization, prepulse, angle of incidence, and spot size on target, these sources yield $10^{-5} < \eta_x < 10^{-4}$.

Figure 17 shows the dependence of the conversion efficiency and x-ray yield on laser intensity for titanium K - α radiation with data from Jiang *et al.* (1995), Reich *et al.* (2003), Riley *et al.* (2005), Khattak *et al.* (2006), and Kritcher, Neumayer, Castor, *et al.* (2008). The results are reproducible to within a factor of 2–5 with laser energy and power varying from <1 to 300 J and 30 to 200 TW. However, comparison with the theory developed by Salzmann *et al.* (2002) has shown that these data are a factor of 5–10 smaller than calculations indicating that full optimization of laser and target parameters are challenging.

Improvements of conversion efficiency values have been reported. Rousse *et al.* (1994) and Bastiani *et al.* (1999) showed high x-ray yield with production of a preplasma. Ziener *et al.* (2002) independently showed that

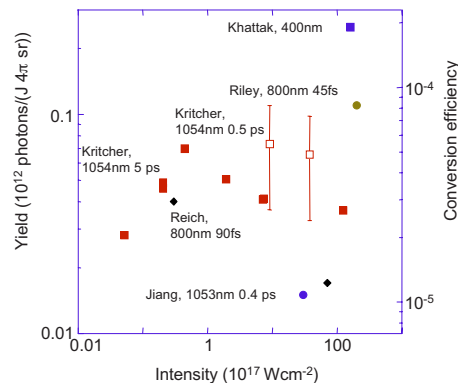


FIG. 17. (Color online) The x-ray conversion efficiency, along with a typical error bar of 50%, for the titanium K - α x-ray emission at 4.5 keV as function of the short-pulse laser intensity.

the K - α yield varied by a factor of 1.8 for different laser intensities, while the variation in the density scale length has been observed to provide a gain factor up to 4.6. Kritcher *et al.* (2007) showed moderate enhancement with perylene coatings. Khattak *et al.* (2006) showed a factor of 4 enhancement using frequency-doubled radiation compared to Riley *et al.* (2005). However, because of the lack of efficient frequency conversion, this improvement in conversion efficiency is often canceled by the use of smaller laser energy on target. Similarly, high conversion efficiencies with shorter pulse length observed by Kritcher, Neumayer, Lee, *et al.* (2008) do not lead to more powerful x-ray probes because of restrictions of laser energy at high power operations.

Other studies have developed improved target configurations such as nanostructured velvet targets (Kulcsar *et al.*, 2000), or cones (van Woerkom *et al.*, 2008) enhancing laser absorption. Improved conversion efficiencies by more than one order of magnitude have been reported, suggesting that ongoing developments in this area will provide very efficient and versatile x-ray sources.

Future x-ray FELs are expected to provide a peak brilliance of 10^{32} – 10^{34} photons per second mrad^2 , mm^2 , and 0.1% bandwidth for photon energies of 10^2 – 10^4 eV [see Ackermann *et al.* (2007)]. Although the laser energy can be tuned and highly focussed, the number of x-ray photons available for probing is smaller compared to laser sources. For present single-shot x-ray scattering applications (Ackermann *et al.*, 2007), a total of 10^{12} probe x rays can be provided at the dense plasma for x-ray energies up to 92 eV within a bandwidth of $\Delta E/E \leq 0.5\%$ and in a 20 fs long pulse. At lower x-ray energies, the number of photons available is slightly higher with total energy deliverable on target being constant. At the future FEL (Akre, 2008), a total of 10^{12} probe x rays are projected at an energy of up to 8.5 keV.

Figure 18 compares the x-ray probe energy from plasma and FEL sources as function of x-ray probe energy. Data for thermal He- α or Ly- α sources are taken from Workman and Kyrala (2001), the chlorine data are

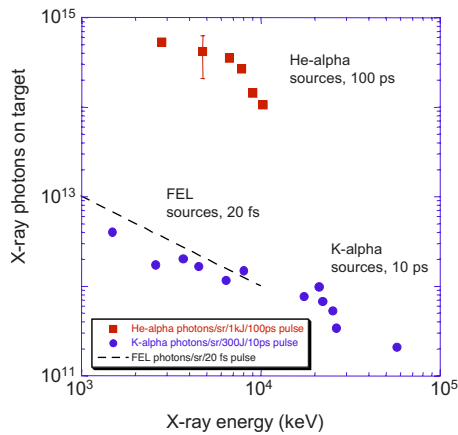


FIG. 18. (Color online) X-ray photons available for x-ray scattering experiments from laser-produced plasmas sources, along with a typical error bar of 50%, as function of x-ray energy. For He- α sources data produced with frequency-tripled (3ω) lasers were chosen while K- α data are taken from experiments without frequency conversion. The dashed line indicates the photon numbers expected from future x-ray free-electron lasers.

from Urry *et al.* (2006), and the titanium data from Riley, Woolsey, *et al.* (2002) and Glenzer, Georgi, Rogers, *et al.* (2003). High energy ($E > 50$ keV) K- α conversion efficiencies are from Schnurer *et al.* (1996) and Tillman *et al.* (1997), medium energy K- α conversion efficiencies (10 keV $< E < 50$ keV) are from Beg *et al.* (1997), Yasuike *et al.* (2001), and Park *et al.* (2004), and low energy conversion efficiencies are from Rousse *et al.* (1994) and Wharton *et al.* (1998). The chlorine data are from Urry *et al.* (2006) and the titanium data from Kritcher, Neumayer, Castor, *et al.* (2008).

Thermal He- α foil sources provide a conversion efficiency of $\eta_x \approx 0.004$ at 4.75 keV into a bandwidth of $\Delta E/E = 0.5\%$, providing a total photon number of 5×10^{12} photons per 1 J of incident laser energy and into a solid angle of 4π sr. Assuming laser pulses with total energy of 1 kJ per 100 ps and laser intensities of 10^{15} W cm $^{-2}$ giving a surface area of 1 mm 2 . As outlined above the probe x rays will interact with the dense plasma subtending a solid angle of $d\Omega = 1$ sr. This will yield a peak x-ray brilliance of $B(4.75 \text{ keV}) = 5 \times 10^{12}$ photons $\times 10^3 \times (4\pi)^{-1} = 4 \times 10^{14}$ photons/100 ps (0.5% bw/sr) at the dense plasma in a single shot.

At 4.5 keV, K- α sources provide two orders of magnitude smaller photon numbers in approximately 10 ps x-ray pulses; this pulse length has been measured by Chen *et al.* (2007) for picosecond laser irradiation. In the present experiments, 300 J of short-pulse laser energy has been routinely delivered on target with $B(4.75 \text{ keV}) = 1.7 \times 10^{12}$ photons/10 ps (0.5% bw/sr), to be substantially improved with more energetic short-pulse laser systems. Therefore, with increasing x-ray energy, K- α sources become more favorable providing roughly the same x-ray probe energy as thermal He- α or Ly- α sources at about 22 keV, the probe energy pres-

ently being considered to probe the final stages of imploding capsule conditions. On the other hand, 10 keV x-ray probes are largely sufficient to probe the imploding shell for studies of the assembly of thermonuclear fuel. Free-electron lasers provide 10^{12} photons on target for energies of about 92 eV in a 20 fs long pulse. Although the solid angle can be made very small by tightly focussing the beam, the total number of x-ray photons available for scattering does not change. At future free electron laser facilities, x-ray probes with an order of magnitude more photons are expected.

C. Spectrometers

Measuring the x-ray Thomson scattering signal requires highly efficient spectrometers as well as moderate spectral resolution to discriminate between the elastic and inelastic scattering components. For free-electron or soft x-ray laser experiments in the vacuum-ultraviolet spectral range, $6.7 < \lambda < 32$ nm, reflection grating spectrometers fielded by Nakano *et al.* (1984), Beiersdorfer *et al.* (1999), and Harada *et al.* (1999) are available. They are advantageous compared to transmission grating spectrometers (Jasny *et al.*, 1994) because they are highly reflective and further do not show ghosts that occur due to the support structure of transmission gratings.

For x-ray wavelength below 6.5 nm, crystals with high reflectivity are available (Beiersdorfer *et al.*, 2004). In x-ray scattering experiments in the range $3 < E < 9$ keV, Bragg crystals in the mosaic focusing mode (Yaakobi and Burek, 1983) have been employed to spectrally disperse the scattered photons onto an efficient detector, cf. Sec. IV.D. The crystals intersect a solid angle of $0.1 \text{ rad} \times 3 \text{ mrad} / 4\pi$ to measure the spectrum for a defined \mathbf{k} vector (Pak *et al.*, 2004). Alternatively, a wide angle spectrometer with a highly oriented pyrolytic graphite (HOPG) crystal has been developed by Garcia Saiz *et al.* (2007) to measure the energy-resolved spectrum of scattered x rays from a dense plasma over a wide range of angles in a single shot.

The ideal mosaic crystal consists of mosaic blocks with slightly different orientation of the reflecting planes characterized by the mosaic spread γ . These blocks must individually fulfill the Bragg condition $n\lambda = 2d \sin \theta_B$, where n is the diffraction order, λ is the x-ray wavelength, and θ_B is the Bragg angle. This property leads to a broad rocking curve as shown in Fig. 19. In addition, the mosaic crystal should be thick enough so that it is almost completely reflective in the middle of the mosaic distribution; a reflectivity of 2–9 mrad has been reported by Marshall and Oertel (1997) and Pak *et al.* (2004) for HOPG crystals with a $\gamma = 0.4^\circ$ and $\gamma = 3.5^\circ$. These measurements have been performed in first and second order and with x-ray energies in the range $4.5 < E < 9$ keV. For the 12.6 keV Kr K- α line, Döppner *et al.* (2008) have shown that the reflectivity of HOPG drops by nearly 2 orders of magnitude from 4 mrad to 0.07 mrad when going from first to fourth diffraction order. The reflectivity for the 22 keV Ag K- α line is

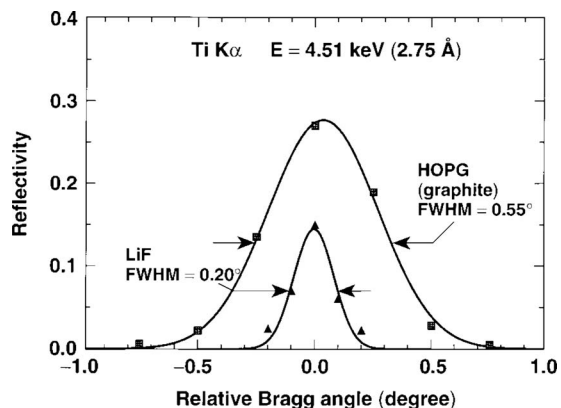


FIG. 19. Rocking curves for HOPG and LiF crystals at 4.51 keV. From Marshall and Oertel, 1997.

about a factor of 3 smaller than at 12.6 keV with a smaller reduction in reflectivity for higher diffraction orders

By differentiating the Bragg law, we obtain a simple estimate of the crystal dispersion $\Delta\lambda/\lambda = \Delta E/E = \Delta\theta/\tan\theta_B$, where E is the x-ray energy and $\Delta\theta$ is the angular spread of the incident x rays. On the other hand, the spatial distribution of energies (i.e., the dispersion) at a normal image plane is

$$\frac{\Delta E}{\Delta x} = \frac{E}{2F \tan\theta_B}, \quad (58)$$

with $\Delta x = 2F\Delta\theta$ and F the focal length (source-to-crystal distance). To obtain optimum signal collection, crystals curved along the sagittal (i.e., nondispersive) plane with a radius of curvature of $R = 115$ mm have been fielded by Urry *et al.* (2006). Best focusing in both the dispersive and sagittal directions is thus achieved when the source-to-crystal and crystal-to-image distances are given by $F = R/\sin\theta_B$.

According to Ice and Sparks (1990), the resolution in the dispersive direction is determined by geometric aberrations with $\Delta x_a \approx \Delta\theta^2 F/2 \tan\theta_B$ (angles in radians). These aberrations result in negligible broadening. Other broadening mechanisms which affect the focus and resolution of the emission lines have been considered by Pak *et al.* (2004). Estimates for 4.51 keV (Ti $K\alpha$) up to 8.64 keV (Zn $K\alpha$) indicate that finite source size and natural linewidth result in $\Delta E/E < 5 \times 10^{-4}$ while intrinsic defocusing accounts for $\Delta E/E \approx 2 \times 10^{-4}$. Volume (depth) broadening, however, appears to be significant resulting in $\Delta E/E \approx 1 \times 10^{-3}$. The latter also induces an asymmetry enhancing the high energy wing of the spectral feature. On the other hand, in the sagittal direction the mosaic broadening of $\Delta y_m = 2\gamma F \sin\theta_B$ is the dominant mechanism severely limiting the spatial resolution. In case of a curved HOPG crystal, the aberrations in the sagittal and dispersive direction mix, thus limiting the spectral resolution to $\Delta E \approx 10$ eV. The use of a mosaic crystal further results in a nonuniform intensity distribution in the focal plane that need to be corrected by flat-fielding the spectrometers, e.g., with *in situ* measurements of bremsstrahlung emission.

Figure 20 shows the results of the spectral resolution measurement of the graphite crystal using a titanium $K\alpha$ x-ray source at 4.5 keV. When the distance between the source and the crystal equals the distance between the crystal and the detector plane, a focussed image (mosaic focusing) with a spectral resolution of $\Delta\lambda/\lambda = 0.003$ has been observed. If this ratio deviates significantly from 1, the mosaic structure of the crystal is observed, resulting in a rather poor spectral resolution. These tests have further confirmed that the graphite crystal has a high reflectivity, a factor of 3 larger than LiF, and more than 1 order of magnitude larger than PET or KAP crystals.

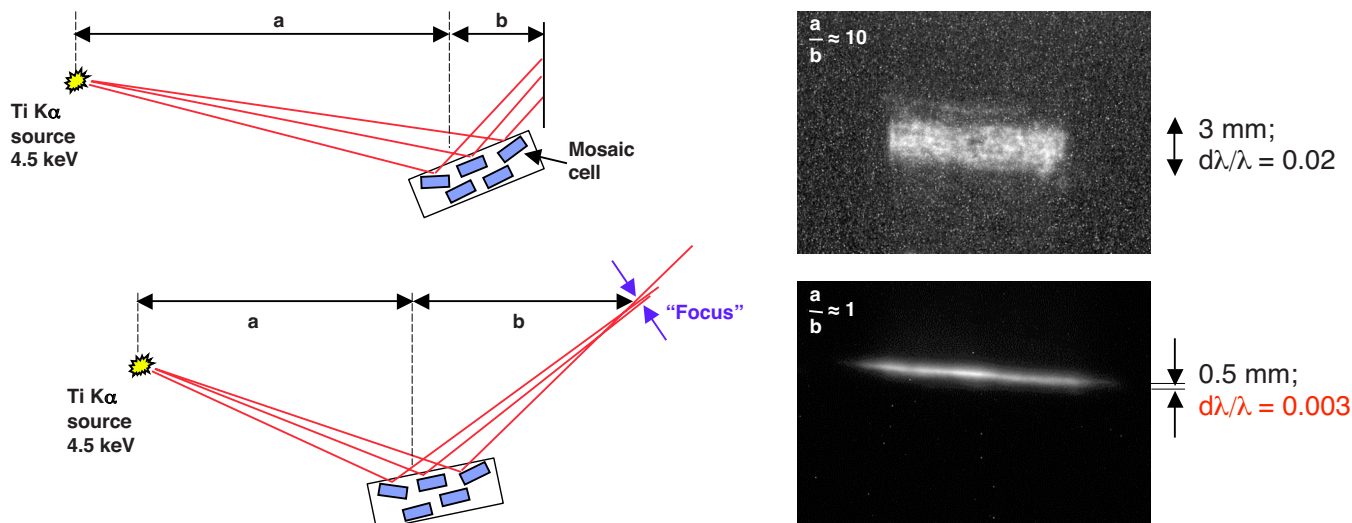


FIG. 20. (Color online) Demonstration of mosaic focusing mode using a HOPG Bragg crystal. This configuration provides simultaneously a high reflectivity from the carbon crystal and a sufficient wavelength resolution of $\Delta\lambda/\lambda = 0.003$ for spectrally resolved x-ray Thomson scattering measurements. From Glenzer, Gregori, Rogers, *et al.*, 2003.

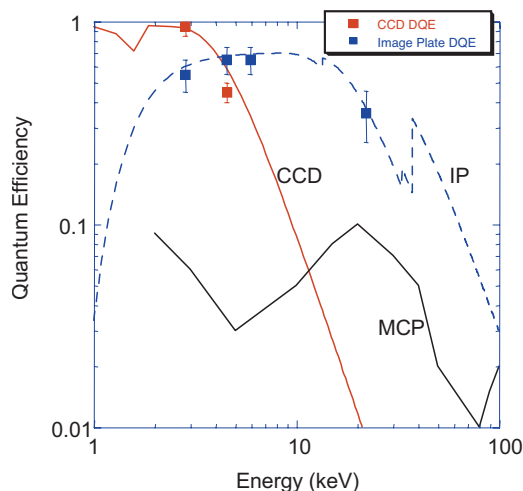


FIG. 21. (Color) Quantum efficiency of CCD (back illuminated) and MCP detectors (Bateman, 1977) as function of x-ray energy. Measured detection quantum efficiency data of CCD and IP detectors from Neumayer (2008) and Izumi (2008) shown together with the IP calculated absorption scaled to the measured data at 3 and 4.5 keV.

D. Detectors

In the x-ray energy range of <10 keV, charged coupled device (CCD) cameras are routinely used for detection, primarily because of their high detection efficiency and versatility. The CCD linearity is $\pm 0.25\%$ for signals between $<0.5\%$ and $>80\%$ of the full dynamic range. Also important for quantitative measurements, the CCD readout noise of <5 electrons is advantageous when compared to charge injection device (CID) cameras that show a linearity of $\pm 3\%$ and a readout noise of <240 electrons. Multiple readouts can partly improve readout noise, but the number of readouts is limited by dark current. To measure scattering spectra temporally resolved with a resolution of ≈ 100 ps, microchannelplate (MCP) detectors combined with CCD cameras have been successfully fielded.

Figure 21 shows the quantum efficiency (QE) for CCD, MCP, and image plate (IP) detectors (Bentley, 1977; Meadowcroft *et al.*, 2008). Generally, the signal-to-noise ratio of the detected signal relates to the signal-to-noise ratio of the input signal via the detective quantum efficiency (DQE), $SNR_{\text{out}} = \sqrt{DQE} SNR_{\text{in}} = (DQE N_{\text{photons}})^{1/2}$, with $N_{\text{photons}}^{1/2}$ the statistical quantum noise (Zanella 2002). In case that other additional noise sources are negligible (e.g., readout noise or experimental fluorescence noise), we have $DQE = QE$, otherwise $DQE < QE$.

CCD cameras show a high QE approaching 1 for x rays with energies $E < 4$ keV and becoming insensitive for energies $E > 20$ keV. For higher x-ray energies and also in high *emp*, neutron, and high gamma flux environments, film has traditionally been the alternative to CCD cameras, and is now being replaced by IP [see Izumi *et al.* (2006)]. These x-ray detectors are sensitive

up to x-ray energies of about 100 keV, and less sensitive than CCD cameras for $E < 4$ keV.

The DQE of IP detectors has been estimated by Amemiya *et al.* (1988) to be 80% for x-rays with energies 8–20 keV. The high values are explained by high absorption efficiency of the phosphor and 1/300 lower background levels than film. The fading time constants have been measured by Meadowcroft *et al.* (2008) to be sufficiently large for applications with high power lasers. The CCD and IP data shown in Fig. 21 have been obtained in laser-produced $K\text{-}\alpha$ experiments by Neumayer (2008), where the DQE of IP is less than ideal due to additional noise from the short-pulse laser experiment. According to Amemiya and Miyahara (1988) a higher DQE is possible in more ideal conditions. The dynamic range of $1\text{--}10^5$ with a high linearity and the spatial resolution of $150\ \mu\text{m}$ (full width at half maximum) match well for measuring the scattering features described in Sec. III and from plasma samples considered in Sec. IV.A.

Significantly higher efficiency of gated detectors than the values indicated in Fig. 21 with data by Bateman (1977) appears possible. A larger DQE of CsI photocathodes by at least one order of magnitude has been reported by Lowney *et al.* (2004) for use with grazing incidence x rays with energies $E \leq 1$ keV. For pulsed microchannelplate detectors, the dependence on the angle of incidence has been investigated by Landen, Lobban, *et al.* (2001). A factor of about 3 improvement can be achieved when applying grazing incidence detection at $\sim 3^\circ$ as opposed to the configuration in present experiments at the Omega laser that have been performed at $\sim 8^\circ$.

In the future, complementary metal oxide semiconductor (CMOS) image sensors may be also applied. The quantum efficiency is comparable to front illuminated CCD detectors but with a fill factor of 65%. Their readout noise as well as gain nonuniformity is significantly larger than for CCD cameras; the noise is 200 electrons per pixel with 3.6 eV per electron hole pair. The CMOS development is directed toward smaller features and lower voltage both affecting imaging performance, but these factors also imply less sensitivity to neutron-induced noise. For neutron energies of 3–10 MeV, CMOS detectors have $< 2 \times 10^{-10}$ damage sites per pixel and per incident neutron. CCDs have 4×10^{-8} damage sites per pixel and per incident neutron, two orders of magnitude more than for CMOS. These features indicate that strong shielding is required in a neutron environment and will likely limit routine scattering experiments with these detectors to neutron flux environments of $< 10^{14}/4\pi$ neutrons.

E. Photometrics

In x-ray Thomson scattering experiments, the intense x-ray source, the closely coupled geometry, and the high detection efficiency result in a substantial fraction of scattered photons. For $n_e = 3 \times 10^{23}\ \text{cm}^{-3}$, the Thomson

scattering cross section, and a path length of $\ell=0.1$ cm, the scattering fraction is $n_e\sigma\ell=0.02$, close to the maximum desirable for avoiding multiple scattering. Coupled with a source solid angle of 1 sr, the scattered efficiency is 10^{-3} , which is substantially larger than that available for optical Thomson scattering experiments, allowing single-shot experiments with 10^{12} photons at the plasma sample.

The total number of the detected photons $N_{\text{ph},d}$, is estimated from Eq. (10),

$$N_{\text{ph},d} = \left(\frac{E_L}{h\nu} \eta_x \right) \left(\frac{\Omega_{\text{plasma}}}{4\pi} \eta_{\text{att}} \right) \left(\frac{n_e\sigma_{\text{Th}}\ell}{(1+\alpha)^2} \right) \times \left(\frac{\Omega_{\text{det}}}{4\pi} R_{\text{crystal}} \eta_d \right), \quad (59)$$

where E_L is the laser energy, η_x is the conversion efficiency from the laser energy into the probe x rays, η_{att} is the attenuation of the probe x rays through the dense plasma, Ω_{plasma} is the solid angle that the plasma subtends with respect to the x-ray source, Ω_{det} is the solid angle subtended by the detector as determined by the crystal and detector size and distance from the plasma, R_{crystal} is the integrated reflectivity of the crystal, and η_d is the efficiency of the detector including the MCP efficiency and filter transmission. The factor $(1+\alpha)^{-2}$ applies for estimates of the inelastic scattering signal.

With $\eta_{\text{att}} \approx 1/e$, a He- α source at 4.75 keV effectively scatters $(E_L/h\nu)\eta_x(\Omega_{\text{plasma}}/4\pi)\eta_{\text{att}} \approx 2 \times 10^{14}$ photons at the target (Sec. IV.B). The collection efficiency of $0.1\text{rad} \times 3\text{mrad}/4\pi \approx 3 \times 10^{-5}$ (Sec. IV.C) and a detection efficiency for a MCP detector plus filter of $\eta_d \approx 0.01$ (Sec. IV.D) result in a collection fraction of 3×10^{-7} . Combined with a scattering fraction of 0.02, the total number of collected photons is 10^6 for the experiments of Glenzer, Gregori, Lee, *et al.* (2003), Glenzer, Gregori, Rogers, *et al.* (2003), Gregori *et al.* (2004), Gregori, Glenzer, Chung, *et al.* (2006), Glenzer, Landen, *et al.* (2007), and Lee *et al.* (2009).

The detection efficiency has been substantially improved for experiments with $K\text{-}\alpha$ sources. A curved crystal improved the collection efficiency by a factor of 2 (Urry *et al.*, 2006) and use of a IP detector improved the detection efficiency by a factor of about 50. At 4.5 keV, the $K\text{-}\alpha$ source provides 2×10^{12} photons into 1 sr. For the experiments of Kritcher, Neumayer, Castor, *et al.* (2008), the target subtends 0.25 sr and $\ell=0.01$ cm yielding $N_{\text{photons}} \approx 3 \times 10^3$ photons collected in a single shot.

For use with a CCD camera with a gain of $g_{\text{CCD}}=3.5$ eh/count (electron holes per count) and $g_{\text{eh}}=3.6\text{eV/eh}$ is the energy required to liberate an electron hole (eh) pair per incident photon of energy E , a total number of counts of $N_{\text{photons}} \times E/g_{\text{CCD}}g_{\text{eh}}$ is expected. Experiments by Kritcher, Neumayer, Castor, *et al.* (2008, 2009) and Kritcher, Neumayer, Lee, *et al.* (2008) have employed curved HOPG crystal spectrometers illuminating about 50×20 pixels. Thus, the collected photons are distributed over 10^3 pixels resulting in a scattering signal of about 1000 counts.

Photometrics sets the practical limits on the temporal and spatial resolution of x-ray Thomson scattering measurements. Scattering experiments with future x-ray FELs will provide single-shot detection signals comparable to Kritcher, Neumayer, Castor, *et al.* (2008, 2009) with the added benefit of 20 fs temporal resolution and possible spatial resolution of order $1 \mu\text{m}$. In addition, high repetition rate capability will provide spectra with signal-to-noise ratios of >100 compared to 10–20 in single-shot experiments.

For future experiments on NIF, a suitable x-ray probe at energies of 22 keV where x rays penetrate through the dense capsule with $\eta_{\text{att}} \approx 1/e$, must overcome bremsstrahlung emission of $10^{-7} \text{J(eV sr)}^{-1}$ corresponding to 10^4 detected photons per eV; cf. Fig. 15. In this case, more than 2 orders of magnitude higher electron densities than the experiment by Kritcher, Neumayer, Castor, *et al.* (2008, 2009) will result in acceptable signal-to-noise ratio using the short-pulse laser capability on the NIF. With these $K\text{-}\alpha$ x-ray sources, a temporal resolution of 10 ps and a scattering volume with scale length of $100 \mu\text{m}$ single have been achieved in single-shot experiments.

V. X-RAY THOMSON SCATTERING EXPERIMENTS

A. Isochorically heated matter

Figure 22 shows a schematic of backward and forward scattering experiments on isochorically heated solid-density beryllium. The beryllium is homogeneously and isochorically heated by $L\text{-shell}$ x rays from a mid- Z foil (1–2 μm thick Mg, Rh, or Ag foils wrapped around the Be). The dense plasma is probed after $t=0.5$ ns with the narrowband x-ray probe from titanium or chlorine He- α or Ly- α radiation. The high laser energy for producing the narrow band x-ray probe and the broadband heating radiation provides sufficient photons for producing homogeneous HEDP states of matter and probing in single-shot experiments. The same target platform has been subsequently employed by Gregori *et al.* (2004) and Gregori, Glenzer, Chung, *et al.* (2006) to probe isochorically heated carbon. Results for carbon are presented in Sec. V.B. Isochoric heating of experiments has the advantage that the mass density is known *a priori* so that the electron density can be directly inferred if the ionization state is known or vice versa.

Figure 23 shows an example of a backscattering spectrum from heated beryllium. Elastic scattering from both the titanium He- α radiation at 4.75 keV and Ly- α radiation at 4.96 keV is observed together with the downshifted Compton scattering feature. The Compton scattering feature shows significant broadening due to the thermal motion of the electrons resulting in factor of >2 larger width than scattering spectra from cold beryllium, i.e., no heater laser beams (see Glenzer, Gregori, Lee, *et al.*, 2003). The spectrum is fitted by theoretical spectra, employing the measured spectrum of the titanium probe x rays, spectrometer resolution, and the dy-

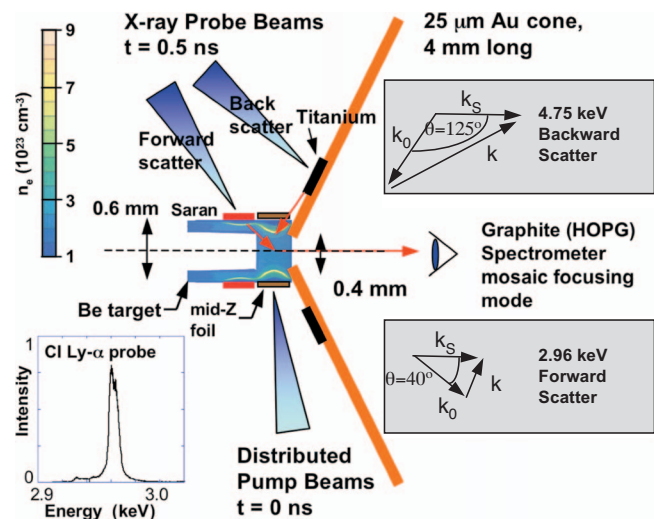


FIG. 22. (Color) Schematic of scattering experiments employing the titanium He- α spectral line in backscattering at $\theta = 125^\circ$ or the chlorine Ly- α line in forward scattering at $\theta = 40^\circ$. The inset shows a Ly- α source spectrum with an intensity contrast of dielectronic satellites to Ly- α of $\leq 5\%$ for up to 7 kJ of laser energy to produce the narrowband x-ray probe radiation. The k-vector diagrams show the averaged scattering vectors in both geometries yielding noncollective or collective scattering. Up to 15 kJ of laser energy has been used for producing the broadband L -shell heating radiation for isochorically heating the target. A density contour plot from radiation-hydrodynamic modeling using the code LASNEX has been overlaid on the Be target, indicating that only homogeneously and isochorically heated beryllium is in the field of view of the spectrometer at the time of the measurements. Note that the color map of the density contour is displayed. From [Glenzer, Gregori, Lee, et al., 2003](#) and [Glenzer, Landen, et al., 2007](#).

dynamic structure factor of Sec. III, providing temperatures and densities from the broadening of the Compton downshifted line and from the intensity ratio of elastic to inelastic scattering components, respectively. The figure also shows the sensitivity of the shape of the red Compton scattering wing to the electron temperature. The latter is inferred from these data with an accuracy of about 10%.

A similar analysis has been performed when inferring the ionization state and the electron density from the intensity ratio of elastically to inelastically scattered radiation. With these conditions with large values of k and where the contribution of weakly bound electrons to the intensity of the inelastic scattering component is small, the intensity of the elastic scattering feature approaches f^2 ([Peyrusse, 1990](#)). For the data in Fig. 23 the ratio yields the density with accuracy of about 15%. For lower temperature conditions, however, where bound electrons scatter nonelastically, the contributions from free and weakly bound electrons blend. Nonetheless, the bound-free spectrum is well known and can be distinguished from the Compton scattering spectrum of the free electrons yielding temperature and density information with slightly larger error bars.

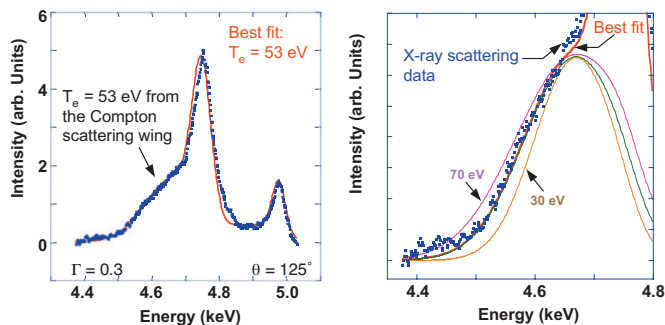


FIG. 23. (Color) Scattering spectrum (blue dots) from isochorically heated beryllium. Elastic and inelastic (Compton) scattering components are observed from both the titanium He- α and Ly- α probe x rays (left). The spectrum is well fitted with theoretical scattering spectra employing the dynamic structure factor of Sec. III (red line). The fit to the red wing of the Compton scattering spectrum is sensitive to the temperature (right). These data provide temperatures of $T_e = 53$ eV and densities of $n_e = 3.3 \times 10^{23} \text{ cm}^{-3}$ characterizing the solid density plasma regime with an error bar of about 10%. From [Glenzer, Gregori, Lee, et al., 2003](#).

To access collective scattering, in a weakly degenerate solid-density beryllium plasma with electron temperature of the order of the Fermi temperature, $T_e \approx T_F = 15$ eV, requires forward scattering with $\theta = 40^\circ$ and x-ray probe energies of order $E_0 = 3$ keV ($\lambda \approx 0.4$ nm). With these conditions, the scattering is predominantly probing \mathbf{k} vectors with $k = 1 \text{ \AA}^{-1}$. Calculating the screening length at the effective temperature results in $\alpha = 1.6$. In this regime, the scattered light spectrum shows collective effects corresponding to scattering resonances off ion acoustic waves and off electron plasma waves, i.e., plasmons.

Figure 24 shows experimental scattering spectra from

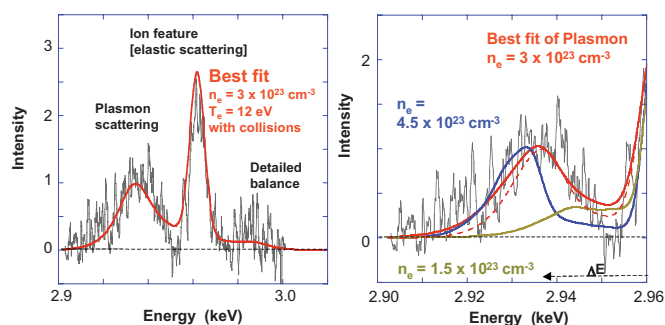


FIG. 24. (Color) Scattering spectrum (gray line) from isochorically heated beryllium. Plasmon scattering downshifted and upshifted in energy is observed, where the intensity of the upshifted plasmon is reduced according to detailed balance, cf. Eq. (18). The spectrum is best fit with theoretical scattering spectra of Sec. III for $T_e = 12$ eV and $n_e = 3 \times 10^{23} \text{ cm}^{-3}$ (left). Also shown is the comparison of the plasmon spectrum with calculations for two different densities, $n_e = 4.5 \times 10^{23}$ and $1.5 \times 10^{23} \text{ cm}^{-3}$, indicating that the spectrum is best fit for $n_e = 3 \times 10^{23} \text{ cm}^{-3}$. The dashed curve represents a calculation for a density of $n_e = 3 \times 10^{23} \text{ cm}^{-3}$ that is neglecting collisions (right). From [Glenzer, Landen, et al., 2007](#).

isochorically heated beryllium measured in forward scattering of the chlorine Ly- α line at 2.96 keV. To resolve the plasmon frequency shift and damping in forward scattering, the x-ray bandwidth has to be smaller compared to Compton scattering measurements. In Fig. 24, the plasmon shift of $E=28$ eV was resolved by the chlorine Ly- α probe radiation with an effective bandwidth of 7.7 eV and no significant dielectronic satellite radiation on the red wing of the Ly- α doublet (see inset in Fig. 22). Also shown are theoretical scattering profiles that represent a convolution of the theoretical form factor $S(\mathbf{k}, \omega)$, calculated for the range of \mathbf{k} vectors of the experiment, with the spectral resolution of 7.7 eV.

The ion feature is observed as an elastic scattering peak at $E_0=2.96$ keV that is not resolved in this experiment. On the lower energy wing of the ion feature, we observe a strong plasmon resonance at 2.93 keV. On the higher energy wing with nearly the same frequency shift, the data show a weak up shifted plasmon signal. Compared to the intensity of the down-shifted plasmon, the intensity is reduced by the Bose function [cf. Eq. (18)] reflecting the principle of detailed balance. The intensity ratio of these plasmon features is thus sensitive to the temperature. In this experiment, the signal-to-noise ratio only allows deducing an upper limit from the intensity ratio of $T_e < 25$ eV.

Collision effects on plasmons in $S(\mathbf{k}, \omega)$ are accounted for in the BMA which also incorporates degeneracy effects. While the frequency shift is not affected, collisional damping cannot be neglected. The fit provides a temperature of $T_e=12$ eV and density of $n_e=3 \times 10^{23}$ cm $^{-3}$. Figure 24 (right) indicates that the density is accurately determined by the shift of the plasmon. For the small \mathbf{k} vectors probed in the present experiment, significant deviations from the random phase approximation are not expected (see also Fig. 5) yielding an error bar in density that is solely determined by the signal-to-noise ratio and the quality of the fit. The calculations for densities of $n_e=4.5 \times 10^{23}$ and 1.5×10^{23} cm $^{-3}$ indicate that the error bar in density is of order 20%; a value that has been improved with better signal-to-noise ratio; cf. Sec. V.C.

Inferring the temperature from the collective scattering spectrum requires accurate measurements of the up-shifted plasmon and the application of detailed balance, or alternatively the width of the plasmon may be used. The latter is determined by Landau damping and collisional damping. For the conditions in isochorically heated beryllium, collisions account for an additional broadening of approximately 5 eV. The difference can be as large as a factor of 1.5 for scattering spectra when \mathbf{k} -vector blurring is negligible. Scattering experiments in a regime where damping by collisions dominates the broadening of plasmons are of interest to test models of the collisionality and conductivity in dense plasmas. Including the corrections due to collisions provides a good fit of the plasmon spectrum for a temperature of 12 eV and with the dynamic collision frequency calculated in the Born approximation.

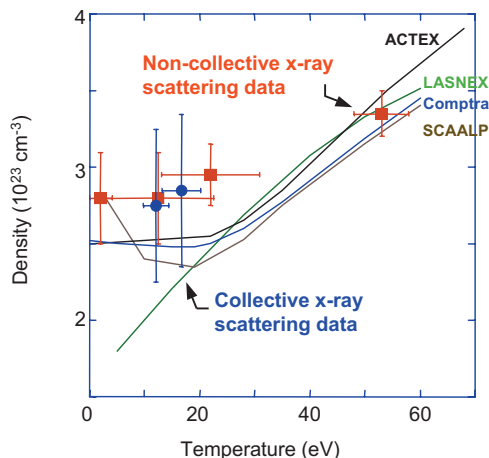


FIG. 25. (Color) The measured densities from noncollective and collective x-ray Thomson scattering experiments shown as functions of the measured electron temperature together with calculations from the codes ACTEX, LASNEX, COMPTRA, and SCAALP. The error bars in electron density are larger for the collective scattering data because of noise.

In experiments, the temperature of the beryllium plasma has been varied using different mid-Z foils, i.e., Mo, Rh, and Ag, to convert the laser energy to L -shell heating x rays. In addition, on some shots only half of the laser energy per beam has been applied, probing a temperature range of up to $T_e=53$ eV. Figure 25 shows the comparison between experimental data and calculations of densities and temperatures using various chemical and physical picture models.

At the highest temperatures, the measured electron density agrees with various ionization balance models, i.e., the codes ACTEX from Rogers and Young (1997) and Rogers (2000) using the activity expansion method, the code COMPTRA from Kuhlbrodt *et al.* (2005) using the partially ionized plasma model, LASNEX from Zimmerman and Kruer (1975), and SCAALP from Renaudin *et al.* (2002) using a density-functional plasma model. On the other hand, at lower electron temperatures, the role of delocalized electrons requires the calculation of all possible interactions between the plasma constituents including the screening of the bound states. For large densities, the classical Debye-Hückel (Yukawa) potential needs to be replaced by quantum interaction potentials that approach the thermal de Broglie wavelength. This allows the calculation of the number of electrons that are no longer bound to a single ion. These electrons are free or weakly bound like the conduction electrons in a metal and are accounted for in ACTEX. On the other hand, LASNEX calculations that use interpolation functions between the zero and high temperature conductivity limits from Desjarlais (2000); Desjarlais *et al.* (2002) showed deviations from the measured data at small temperatures.

For plasmon measurements, temperatures up to 15 eV have been accessed compared to the noncollective scattering data because (1) the detector was gated earlier during the heating of the plasma, (2) fewer laser

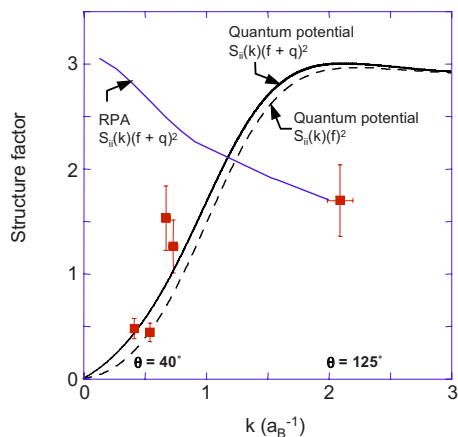


FIG. 26. (Color online) Elastic scattering amplitude data are shown that have been measured as function of the scattering angle from isochorically heated beryllium for a density of $n_e = 3 \times 10^{23} \text{ cm}^{-3}$ and temperature of $T_e = 12 \text{ eV}$. Also shown are calculations using HNC with quantum potential models of Schwarz *et al.* (2007) and the analytical RPA model of Arkhipov and Davletov (1998).

beams have been used to illuminate the L -shell converter, and (3) a higher- Z element was used, i.e., Ag compared to the higher temperature experiments. Calculations for Ag show 20–30 % lower conversion efficiency into L -shell radiation than for Rh or Mo. For these studies, the experimental temperature data agree well with radiation hydrodynamic simulations (Glenzer, Landen, *et al.*, 2007), but the densities are underestimated because the role of delocalized electrons is not accounted for in integrated radiation-hydrodynamic modeling with the code LASNEX.

The data in Fig. 25 show that the plasma parameters inferred from the plasmon spectrum measured in forward scattering are consistent with the data from the Compton scattering spectrum measured in backscattering. In this regime, the plasmon spectrum provides a robust density diagnostic. Nonetheless, future measurements of the plasmon dispersion at large \mathbf{k} will be of interest to test the theory of local field corrections (Gregori, Glenzer, and Landen, 2003; Tauschwitz *et al.*, 2007) and may directly lead to precision measurements of detailed balance, collisions, and quantum diffraction.

Figure 26 shows the experimental elastic scattering amplitude for various scattering angles from isochorically heated beryllium. The absolute values for the amplitude have been calculated from the inelastic scattering feature, namely, the plasmon intensity for measurements at $\theta = 40^\circ$ and the intensity of the Compton scattering feature at $\theta = 125^\circ$. The HNC calculations with the quantum potential of Klimontovich and Kraeft (1974) suggest that the increase in elastic scattering is primarily dominated by the \mathbf{k} -vector dependence of the structure factor, with the q factor a small correction.

The experimental data of Fig. 26 for $k < 1/a_B$ are consistent with HNC calculations by Schwarz *et al.* (2007) with weak quantum potentials [see, e.g., Klimontovich and Kraeft (1974)], which is leading to OCP-like depen-

dence. On the other hand, for $k > 2/a_B$, the HNC calculation overestimates the measured intensity of the elastic scattering signal. Calculations by Gregori, Glenzer, Rozmus, *et al.* (2003) using the analytical structure factor by Arkhipov and Davletov (1998) agree with the data at this \mathbf{k} vector, but the \mathbf{k} dependence is not reproduced. The apparent agreement appears to be due to the fact that the simple long \mathbf{k} -vector limit is correctly obtained. Future calculations employing physical picture modeling of the electron-ion interaction will be needed to obtain a more complete theoretical description of the observations that include the known limits for small k .

B. Matter heated by supersonic heat waves

Back *et al.* (2000), Edwards *et al.* (2000), and Constantin *et al.* (2005) studied matter heated by supersonic heat waves for testing different opacity models and to develop efficient x-ray sources [see Sec. IV.B and works by Back *et al.* (2001) and Fournier *et al.* (2004)]. In particular, the hydrodynamic efficiency of CH capsule ablators and the growth of the Rayleigh-Taylor hydrodynamic instability for ICF studies depend on the soft x-ray opacity and the number of remaining bound carbon K -shell electrons at temperatures of 200–300 eV. In this area, x-ray Thomson scattering measurements are important since they provide data at the required accuracy to critically test kinetics calculations. Moreover, target geometries that make use of hohlraum radiation to drive a heat wave are advantageous because radiation heating can be accurately characterized.

The experiments of Gregori *et al.* (2008) have employed 1.2 mm long, 1.2 mm diameter gold hohlraums heated through a laser entrance hole with 6.2 or 8.5 kJ of laser energy at 351 nm in a 1 ns square pulse. The hohlraum produces a relatively uniform soft x-ray field that is emitted through the laser entrance hole and measured with DANTE, an absolutely calibrated diode array broadband x-ray flux detector, providing a time dependent radiation temperature with maximum drive of $T_{\text{RAD}} = 270 \text{ eV}$. On the other end of the hohlraum, the radiation field drives a supersonic ionization wave into a 300 μm thick carbon foam. The experiments employed the titanium He- α line scattered off the heated foam providing temporally resolved temperature and ionization state data.

These measurements have provided electron temperatures inside the heated foam of $T_e = 130 \text{ eV}$ and indicating rapid heating and cooling of 100 eV/ns. The dynamics of the supersonic heat waves driven by the hohlraum radiation field at radiation temperature T_R has been successfully modeled with a radiation flux model, where the incident radiation flux is balanced by absorption, re-emission, and convection. In particular, applying the measured temperatures results in a correct description of heat wave propagation and burn through time.

The complete ionization balance has been measured in isochorically heated carbon by Gregori, Glenzer, Chung, *et al.* (2006) employing a variety of target plat-

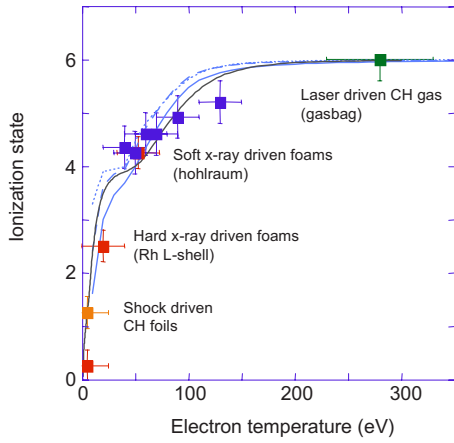


FIG. 27. (Color online) The measured ionization state of carbon is shown as function of the measured electron temperature (Gregori, Glenzer, Chung, *et al.* 2006). These experiments employ noncollective x-ray Thomson scattering experiments on various target platforms. The experimental data points correspond to laser driven gas bag experiments, soft x-ray driven carbon foams, hard x-ray driven carbon foams, and cold plastic foils. Also shown are calculations from kinetic calculations using the code FLYCHK for densities of 10^{21} cm^{-3} (dotted line), 10^{22} cm^{-3} (dashed line), and 10^{23} cm^{-3} (solid line) and COMPTRA for carbon at 0.2 g cm^{-3} (solid dark line).

forms that span electron temperatures from cold to fully ionized carbon at 280 eV. For this purpose, Gregori, Glenzer, Chung, *et al.* (2006) extended the expressions in Sec. III to calculate the x-ray scattering form factor in multicomponent plasmas. Figure 27 shows experimental data from various experiments. The mid-to-high T_e data points were obtained on low density (0.2 g cm^{-3}) carbon foam targets driven by hohlraum soft x rays (Gregori *et al.*, 2008), while the mid-to-low T_e points correspond to hard x rays isochorically heated higher density (0.7 g cm^{-3}) carbon foams (Gregori *et al.*, 2004). A low temperature data point on cold CH plastic foils (1 g cm^{-3}) from Sawada *et al.* (2007) and a high temperature data point from a fully ionized gas bag plasma (MacGowan *et al.*, 1996; Glenzer *et al.*, 1997) are also shown in the figure. The complete data set presents the full ionization balance curve for carbon over a large range of electron temperatures in the range $2 < T_e < 300 \text{ eV}$ and densities in the range $10^{21} < n_e < 10^{23} \text{ cm}^{-3}$.

Comparison with ionization balance calculations is given in Fig. 27 for the COMPTRA (Kuhlbrodt *et al.*, 2005) and FLYCHK (Chung *et al.*, 2003) codes. The calculation reported in the figure for COMPTRA corresponds to the case of solid density carbon at 0.2 g cm^{-3} . The model shows good agreement with the data except in the 120–170 eV range, which is near the transition from heliumlike to hydrogenlike carbon. Similar behavior is also shown by FLYCHK for which three calculations are shown with densities of 10^{21} cm^{-3} (dotted line), 10^{22} cm^{-3} (dashed line), and 10^{23} cm^{-3} (full line). From Saha equilibrium, the calculations for higher densities result in a smaller ionization states. With exception of

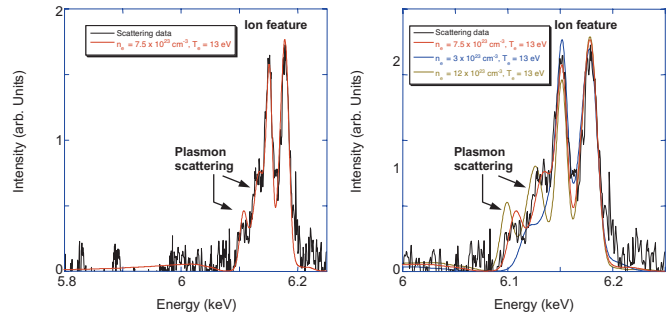


FIG. 28. (Color) Experimental and theoretical scattering spectra are shown from shock-compressed Be at 25° scattering angle (Lee *et al.*, 2009). The best fit to the data yields $n_e = 7.5 \times 10^{23} \text{ cm}^{-3}$, $Z_f = 2$, and $T_e = 13 \text{ eV}$ (left). The plasmon energy is a sensitive measure of the electron density (right).

the transition region between heliumlike to hydrogenlike carbon, the ionization balance calculations agree well with the experiments. These results warrant future work on kinetics collisional radiative modeling to improve the accuracy of the calculations in the aforementioned transition region.

C. Shock-compressed matter

Fermi-degenerate dense plasmas are accessed in laser shock-compressed foils using the target platform shown in Fig. 14. The laser beams directly illuminate the foil with intensities in the range $10^{14} < I < 10^{15} \text{ W cm}^{-2}$ compressing the foil by ablation pressure in the range 20–60 Mbar. In the experiments by Lee *et al.* (2009), beryllium was employed and x-ray Thomson scattering measurements at various times during the drive resulted in electron densities of $n_e = 8 \times 10^{23} \text{ cm}^{-3}$ and temperatures of 13 eV. The experiments by Lee *et al.* (2009) established x-ray Thomson scattering as a direct diagnostic for characterizing compressed states of matter.

Figures 28 and 29 show the experimental scattering data for 25° and 90° scattering angle accessing the collective and noncollective regimes, respectively. Also

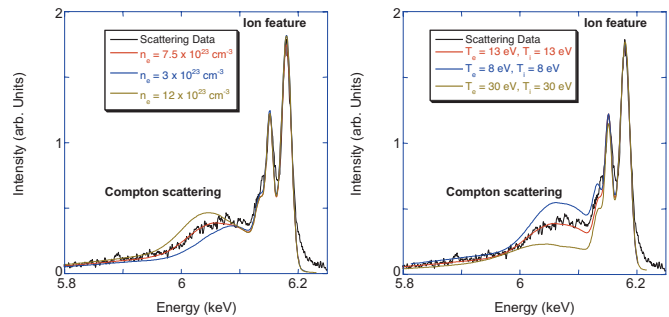


FIG. 29. (Color) Experimental and theoretical scattering spectra are shown from shock-compressed Be at 90° scattering angle (Lee *et al.*, 2009). The best fit to the data yields $n_e = 7.5 \times 10^{23} \text{ cm}^{-3}$, $Z_f = 2$, and $T_i = 13 \text{ eV}$. The width of the Compton energy is a sensitive measure of the electron density (left) and the intensity ratio of elastic to inelastic scattering is sensitive to the ion temperature (right).

shown are corresponding theoretical spectra. In these experiments, the 6.2 keV He- α x-ray spectrum has been used for probing the compressed beryllium with the advantage that these x rays are of sufficiently high energy to penetrate through the high density plasma, and with the disadvantage that the probe consists of two spectral features of comparable intensity, namely, the 6.181 keV Mn He- α and 6.153 keV intercombination x-ray probe lines. Gaussian convolution has been performed with FWHM=11 eV in the case of the intercombination line and FWHM=14 eV for the He- α spectral feature, respectively. Three weak satellite lines whose intensities relative to the main spectral features have also been determined with direct measurements of the x-ray probe spectrum have been included in the fit.

For forward scattering at an angle of 25° , the collective scattering regime has been accessed with $\alpha \approx 1.6$. Two plasmons have been observed, one corresponding to the He- α and one to the intercombination line. The plasmons are downshifted in energy by 50 eV, indicating an electron density of $n_e = 7.5 \times 10^{23} \text{ cm}^{-3}$. Assuming an ionization state of $Z_f = 2$ consistent with simulations and temperature measurements in the noncollective regime (cf. Fig. 29) results in a compression of 3.3 for a laser drive intensity of $3 \times 10^{14} \text{ W cm}^{-2}$ and a calculated pressure of 28 Mbar.

Also shown in Fig. 28 are theoretical spectra for two electron densities, i.e., noncompressed and approximately five times compressed beryllium indicating that the electron density is accurately measured from the frequency shift of the plasmons. Calculating the standard deviation between the data and theoretical spectra for variety of conditions shows that the error bar is approximately 10%.

These densities result in a Fermi energy of $\epsilon_F = 30 \text{ eV}$. With these conditions, the Compton scattering spectrum of the He- α and intercombination x-ray probe lines measured in non-collective scattering with $\alpha \approx 0.5$ at a scattering angle of 90° on a separate shot and with the same laser drive shows a paraboliclike spectrum. As expected for a Fermi-degenerate plasma, the width of the Compton spectrum provides the Fermi energy. In addition, the intensity ratio of the elastic to inelastic scattering feature from Fermi-degenerate plasmas is sensitive to the ion temperature because elastic scattering is dependent on the ion-ion structure factor.

For the theoretical scattering spectra the electron density and the temperature have been varied. For the analysis, $T_e = T_i$ and $Z = 2$ have been assumed consistent with calculations and with observations from isochorically heated Be. Density and temperature obtained in this way are $n_e = 7.5 \times 10^{23} \text{ cm}^{-3}$ and $T = 13 \text{ eV}$. The error bar due to noise for these measurements is of order 5–10%. The agreement between the density inferred from the plasmon and Compton data indicate good shot-to-shot reproducibility. Moreover, the results are consistent with the structure factors used at large k and with the bound-free contributions to the Compton line shape that result in low energy wings. For compressed states of

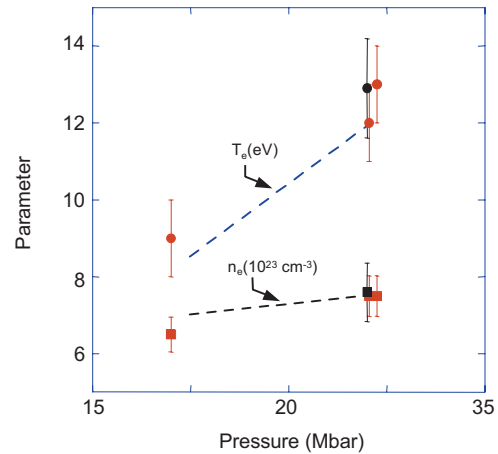


FIG. 30. (Color) Comparison between modeled and measured densities (in units of 10^{23} cm^{-3}) and temperatures (in units of eV) from x-ray Thomson scattering measurements shown as functions of pressure. Black square and black circle symbols represent densities and electron temperatures from plasmon scattering. Red squares and red circles represent the densities and ion temperatures inferred from Compton scattering. Also shown as dashed lines are the results from radiation-hydrodynamic modeling.

matter these contributions become important due to the lowering of the ionization energy.

Figure 30 shows the measured densities and temperatures as function of the pressure. The Compton scattering data are consistent with the plasmon data with the inclusion of bound-free transitions using the model of Schumacher *et al.* (1975). Without bound-free transitions, the density inferred from the tail of the Compton line is larger than obtained from the plasmon frequency shift. For these compressed states of matter, Eq. (44) indicates about 20 eV additional lowering of the ionization energy when compared to isochorically heated matter. This observation indicates that future measurements of the ionization energy lowering in compressed matter at densities beyond the Inglis-Teller limit will be accessible. The experimental data are also consistent with radiation-hydrodynamic simulations of this experiment with the code HELIOS (MacFarlane *et al.*, 2006) indicating that density and temperature are modeled to accuracy of order 10%. These findings demonstrate that conditions reached in ICF capsule implosion experiments can be directly measured with x-ray Thomson scattering.

Generally shock-compressed matter experiments have begun delivering data, indicating that critical tests of collisions, bound-free contributions, ionization energy lowering, and ion-ion structure factor calculations are accessible. For example, the plasmon spectra of Fig. 28 are well fitted with the theory presented in Sec. III. However, data with higher spectral resolution and less noise will be needed to test the different calculations for the collision integral and the plasmon width as presented in Fig. 8; while none of these calculations can be ruled out, the calculation using TCS provides a consistent fit to the data.

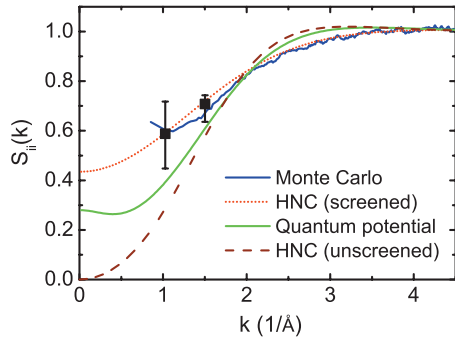


FIG. 31. (Color) Elastic scattering amplitude data shown as function of the scattering angle from shock-compressed Li by Garcia Saiz, Gregori, Gericke, *et al.*, 2008. Also shown are calculations using various HNC models together with DFT Monte Carlo simulations.

Measurements in laser shocked aluminum by Riley *et al.* (2007) attempted modeling of bound-free contributions to the scattering spectra. Initial results indicate that the data are bound by the impulse approximation of Holm and Ribberfors (1989) and the form factor approximation of Schumacher *et al.* (1975). However, more accurate data and characterization of plasma temperature, density, and ionization state such as obtained in beryllium will be required to obtain a critical comparison with modeling.

Experiments by Garcia Saiz, Gregori, Gericke, *et al.* (2008) on shocked lithium allowed inferring the ion-ion static structure factor when calibrating the measured elastic scattering amplitude with the measured signal from free electrons; the latter is determined by the f -sum rule [see Eq. (21)]

$$\int_{-\infty}^{\infty} \left(\frac{d^2\sigma}{d\Omega d\omega} \right)_{\text{free}} \omega d\omega = \frac{Z\hbar k^2}{2m_e}. \quad (60)$$

Figure 31 shows the ion-ion structure factor data together with calculations using DFT for all electrons coupled with molecular dynamics for the ions. Also shown are HNC calculations with various interaction potentials. Within the error bars, these models describe the experimentally observed relative reduction in scattering for small \mathbf{k} . However, in contrast to isochorically heated beryllium, unscreened HNC calculations that essentially use OCP-like behavior underestimate the total structure factor, indicating that screening effects are more important in lithium. The HNC calculations that use the potential inferred from the DFT simulations show good agreement with the data while calculations using the quantum potential of Deutsch (1977) are marginal. A similar conclusion has recently been reached for shocked plastic by Barbrel *et al.* (2009).

A reduction in the elastic scattering features has also been reported from shocked aluminum by Ravasio *et al.* (2007), and interpreted as a Debye-Waller-like correction due to high coupling parameters. These effects may be expected when transitioning from a solid to a liquid state; observations for lithium are reported by Sinn and

Burkel (1996). The scattering experiments on isochorically heated beryllium and carbon, on the other hand, showed strong elastic scattering peaks as described by Peyrusse (1990). Scattering from shocked CH-foils by Sawada *et al.* (2007) also showed elastic scattering consistent with Eq. (32), and when adding bromide impurities to the CH-foil, the elastic scattering amplitude has been observed to increase accordingly. To test the structure of correlated systems, future work employing angularly resolved scattering from states of matter spanning high coupling and high densities will be of great interest.

D. Coalescing shocks

In pump-probe experiments on the medium-size Titan laser, Kritcher, Neumayer, Castor, *et al.* (2008) investigated lithium-hydride plasmas employing a nanosecond laser beam to shock compress the solid target. Density and temperature conditions have been measured with x-ray Thomson scattering from a short-pulse laser-produced 10 ps $K\text{-}\alpha$ source. The power of the nanosecond laser beam was shaped with a 4 ns long foot at $10^{13} \text{ W cm}^{-2}$ and a 2 ns long peak at $3 \times 10^{13} \text{ W cm}^{-2}$, launching two shock waves into the target. Radiation-hydrodynamic simulations with LASNEX showed that the shock waves coalesce and compress the target by a factor of three over the 600 μm focal spot area at 7 ns after the beginning of the laser drive.

The conditions before and during coalescence are directly measured by varying the delay between the nanosecond laser beam and the short-pulse laser produced $K\text{-}\alpha$ x rays. The x rays penetrate the dense material and measurements of the elastic and inelastic scattering components at different times during the shock evolution are observed with a HOPG crystal spectrometer at a scattering angle of about 40° .

Figure 32 shows the scattering spectra at $t=4$ and 7 ns along with the $K\text{-}\alpha$ source spectrum measured with the same spectrometer. Also shown are theoretical fits to the measured scattering data using the theoretical form factor, Eq. (32), convoluted with a Gaussian profile that accounts for both the measured source width and crystal resolution.

At $t=7$ ns, a plasmon is observed that is downshifted in energy by about 25 eV. The shift is dominated by the plasma frequency, i.e., by the electron density, while quantum diffraction results in a correction of order 7 eV. For the low temperatures and high densities in the shock wave, the system is degenerate with $\alpha \approx 1$ and in this case the width and shift of the plasmon yields the electron density of $n_e = 1.7 \times 10^{23} \text{ cm}^{-3}$. Due to noise, the error bar for the density is about 20%.

A temperature history of shock progression through the compressed material has been extracted from the relative intensities of the elastic scattering components; see Fig. 33. The intensity is calibrated by the inelastic scattering component for data at $t=7$ ns. This fact allows inferring ion temperatures from the elastic scattering intensity earlier in the experiment when the inelastic scat-

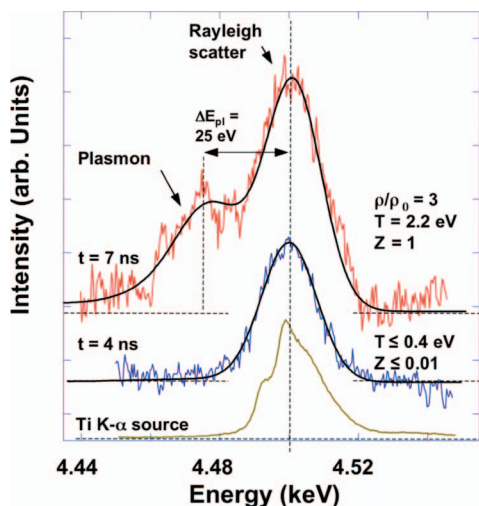


FIG. 32. (Color) Experimental and theoretical scattering spectra from shock-compressed LiH shown at various times. At $t = 7$ ns, the scattering parameter is $\alpha \approx 1$ and the inelastic scattering component shows a plasmon downshifted by 25 eV from the $K\text{-}\alpha$ energy. At $t = 4$ ns, the lack of inelastic scattering indicates small temperatures and negligible ionization. Also shown is the $K\text{-}\alpha$ x-ray probe spectrum. From Kritcher, Neumayer, Castor, *et al.*, 2008.

tering component is weak. In particular, the dynamic structure factor provides the electron temperature assuming $T_e = T_i$. In addition, the intensity of the elastic scattering is insensitive to density. At early times, $t < 6$ ns, the lack of inelastic scattering is a strong indication of low ionization states, $Z < 0.1$, and simultaneously low temperatures, $T_e < 0.5$ eV. Although this procedure relies on knowledge of the structure factor in the range of small \mathbf{k} vectors, weak interaction potentials consistent with Fig. 26 have been employed, and the error bar is expected to be dominated by noise and has been estimated to be 20%.

At shock coalescence, rapid heating to temperatures of 25 000 K is observed when the scattering spectra show the collective plasmon oscillations that indicate the transition to the dense metallic plasma state. At peak temperature, the calculations indicate pressures in the range of $P = 300\text{--}420$ GPa. With $Z = 1$ as determined from the shape of the plasmon with an error bar of 10% and the electron density from the plasmon shift yields a mass density of $\rho = 2.25$ g/cm³, corresponding to three times compression in excellent agreement with the calculations. This value is consistent with the equation of state (EOS) data obtained from density functional perturbation theory by Yu *et al.* (2007), and approach conditions at which Wang *et al.* (2003) predicted the insulator-metal phase transition.

The range of temperatures shown in Fig. 33 are from calculations that include various amounts of impurities and oxide layers consistent with target characterization. The quotidian equation of state model is consistent with the wide range of temperatures accessed in this experiment. The SESAME EOS includes atomic structure based

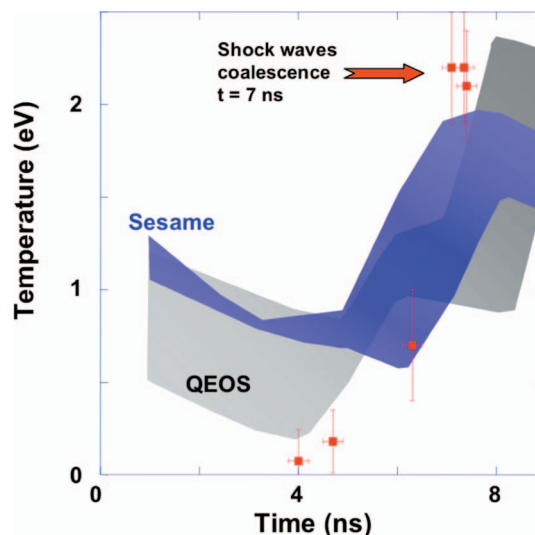


FIG. 33. (Color) The temperature of shocked LiH shown as function of time from x-ray Thomson scattering measurements and from radiation-hydrodynamic modeling using different EOS models (Kritcher, Neumayer, Castor, *et al.*, 2008). The range of temperatures for each model is accounting for LiOH surface impurities (lower bounds) to no impurities (upper bounds). The experiments and calculations demonstrate efficient heating to 2.2 eV by shock coalescence with small differences in shock timing resolved by the short $K\text{-}\alpha$ x-ray pulse.

on solutions of the single-particle quantum levels in the self-consistent field of an atom. The peak temperature and the experimentally observed coalescence time are in good agreement with modeling that uses the SESAME EOS. These results demonstrate the capability to measure the temperature and density in dense matter during shock compression with 10 ps temporal resolution and to resolve small differences in coalescence time predicted by modeling.

The experiments have shown the transition to a metallic plasma state in the solid phase resulting in the observation of plasmons. This feature has further allowed testing of radiation-hydrodynamic calculations with different EOS models for shock-compressed matter. This technique is opportune for HEDP experiments that will achieve extreme densities, e.g., on the National Ignition Facility. In addition, with future x-ray FELs, high repetition experiments will provide the same photons for scattering experiments as employed in these studies, and data with high accuracy will be possible due to reduced noise levels from multiple shots.

VI. SUMMARY AND OUTLOOK

X-ray Thomson scattering has been developed to provide accurate characterization of high energy density plasmas. The interpretation of the inelastic scattering results from low to moderately coupled systems are based on first principles. In particular, x-ray Thomson scattering allows noninvasive probing of the plasma conditions and properties of dense and optically opaque matter. Results from forward and backward scattering measure-

ments in isochorically heated as well as shock-compressed matter have been shown to yield mutually consistent results.

In particular, the electron density inferred from the frequency shift of plasmons agrees with the ionization balance measurements from the intensity ratio of the Compton scattering to elastic scattering component. Moreover, the electron temperature is inferred from the spectrum of the Compton downshifted line that is directly reflecting the electron velocity distribution providing temperatures.

These results show that the x-ray scattering technique can be applied to measure the compressibility of dense matter from the plasmon frequency shift, or in case of a degenerate system, from the Compton scattering feature that will reflect the Fermi temperature. Future applications will include measurements of the conductivity from the collisional damping of plasmons and investigations of the validity of the random phase approximations at large values of the scattering vector \mathbf{k} .

In addition, it is expected that the x-ray Thomson scattering technique will find new applications with the development of target platforms for testing important physics processes in dense or strongly coupled plasmas. While first results on transitions to dense metallic plasma states have been obtained, future studies are expected that will range from stopping power measurements to fast ignition studies and laboratory astrophysics experiments. An important application for measurements of the temperature and density include inertial confinement fusion capsule implosions. Accurate data will allow testing the fuel adiabat, i.e., the ratio of electron to Fermi temperature, and assess assembly of the fuel. First assessments have indicated that the scattering will be dominated by the dense capsule fuel, thus, characterizing the conditions most wanted for measuring the assembly of thermonuclear fuel.

Experiments to determine the physical properties of these dense states of matter have begun to measure the effects of collisions to yield the conductivity in high density and strongly coupled plasmas. Since plasmons will be observed simultaneously with the elastically scattered ion feature, these studies will also determine the structure factor in two component plasmas.

Measurements of structure factors in addition to a direct measure of density and ionization state in shocked matter further indicate that scattering experiments can provide new insights in the ongoing controversy about the equation of state of deuterium. The studies will go beyond testing the equation of state models in integrated radiation-hydrodynamic calculations by yielding directly compression or Hugoniot data when combined with a shock velocity measurement.

X-ray FEL facilities will allow experiments with 20 fs resolution and with much higher repetition rate. Future x-ray Thomson scattering experiments will be aimed to perform high precision measurements and, in particular, to determine thermodynamic properties and equilibration in high energy density plasmas.

LIST OF ACRONYMS AND DEFINITIONS

ARC	Advanced radiographic capability
BMA	Born-Mermin approximation
CCD	Charge coupled device
CID	Charge injection device
DFT	Density-functional theory
DH	Debye-Hückel
DQE	Detective quantum efficiency
EOS	Equation of state
FEL	Free-electron laser
GDW	Gould-DeWitt
HEDP	High energy density physics
HNC	Hypernetted chain
HOPG	Highly oriented pyrolytic graphite
ICF	Inertial confinement fusion
IP	Image plate
LB	Lenard-Balesen approximation
LFC	Local field corrections
MCP	Microchannelplate
NIF	National Ignition Facility
OCP	One component plasma
QE	Quantum efficiency
QEOS	Quotidian equation of state
RPA	Random phase approximation
TCS	Two component screening
TM	T matrix

ACKNOWLEDGMENTS

This work was performed under the auspices of the U.S. Department of Energy by Lawrence Livermore National Laboratory under Contract No. DE-AC52-07NA27344. The work of S.H.G. was also supported by Laboratory Directed Research and Development Grants No. 08-ERI-002 and No. 08-LW-004, and the Alexander-von-Humboldt Foundation. The work of R.R. was supported by the Helmholtz association VH-VI-104 and by the Deutsche Forschungsgemeinschaft SFB 652. We thank O. L. Landen and G. Gregori for their important contributions to the physics of x-ray Thomson scattering. We further thank P. Beiersdorfer, Th. Bornath, D. Bradley, L. Cao, J. Castor, H.-K. Chung, C. Constantin, J. K. Crane, M. P. Desjarlais, L. Divol, T. Döppner, R. W. Falcone, G. Faussurier, R. Fäustlin, E. Förster, C. Fortmann, D. H. Froula, D. O. Gericke, F. Girard, S. Haan, B. A. Hammel, J. Hastings, S. Hatchett, A. Höll, B. Holst, N. Izumi, M. Koenig, W. D. Kraeft, A. Kritcher, N. Kugland, H.-J. Kunze, H. J. Lee, R. W. Lee, B. J. MacGowan, A. J. Mackinnon, K.-H. Meiwes-Broer, D. D. Meyerhofer, E. Morse, D. H. Munro, P. Neumayer, A. Ng, C. Niemann, A. Pak, A. Pelka, S. W. Pol-laine, A. Przystawik, S. Regan, H. Reinholz, D. Riley, H. F. Robey, F. J. Rogers, G. Röpke, M. Roth, W. Rozmus, M. Schollmeier, V. Schwarz, B. Spears, R. Thiele, J. Tiggesbäumker, S. Toleikis, R. Tommasini, T. Tschentscher, M. Urry, I. Uschmann, J. Vorberger, S. Weber, K. Widmann, and U. Zastra for many valuable discussions related to this work.

REFERENCES

- Ackermann, W., *et al.*, 2007, *Nat. Photonics* **1**, 336.
- Akre, R., 2008, *Phys. Rev. ST Accel. Beams* **11**, 030703.
- Amemiya, Y., T. Matsushita, A. Nakagawa, Y. Satow, J. Miyahara, and J. Chikawa, 1988, *Nucl. Instrum. Methods Phys. Res. A* **266**, 645.
- Amemiya, Y., and J. Miyahara, 1988, *Nature (London)* **336**, 89.
- Arista, N. R., and W. Brandt, 1984, *Phys. Rev. A* **29**, 1471.
- Arkhipov, Y. V., and A. E. Davletov, 1998, *Phys. Lett. A* **247**, 339.
- Azechi, H., and F. A. Project, 2006, *Plasma Phys. Controlled Fusion* **48**, B267.
- Back, C. A., J. D. Bauer, O. L. Landen, R. E. Turner, B. F. Lasinski, J. H. Hammer, M. D. Rosen, L. J. Suter, and W. H. Hsing, 2000, *Phys. Rev. Lett.* **84**, 274.
- Back, C. A., J. Davis, J. Grun, L. J. Suter, O. L. Landen, W. W. Hsing, and M. C. Miller, 2003, *Phys. Plasmas* **10**, 2047.
- Back, C. A., J. Grun, C. Decker, L. J. Suter, J. Davis, O. L. Landen, R. Wallace, W. W. Hsing, J. M. Laming, U. Feldman, M. C. Miller, and C. Wuest, 2001, *Phys. Rev. Lett.* **87**, 275003.
- Bai, B., J. Zheng, W. D. Liu, C. X. Yu, X. H. Jiang, X. D. Yuan, W. H. Li, and Z. J. Zheng, 2001, *Phys. Plasmas* **8**, 4144.
- Baldis, H. A., J. Dunn, M. E. Foord, and W. Rozmus, 2002, *Rev. Sci. Instrum.* **73**, 4223.
- Barbrel, B., M. Koenig, A. Benuzzi-Mounaix, E. Brambrink, C. R. D. Brown, D. O. Gericke, B. Nagler, M. Rabec le Gloahec, D. Riley, C. Spindloe, S. M. Vinko, J. Vorberger, J. Wark, K. Wünsch, and G. Gregori, 2009, *Phys. Rev. Lett.* **102**, 165004.
- Barty, C. P. J., *et al.*, 2004, *Nucl. Fusion* **44**, S266.
- Bastiani, S., P. Audebert, J. P. Geindre, T. Schlegel, J. C. Gauthier, C. Quiox, G. Hamoniaux, G. Grillon, and A. Antonetti, 1999, *Phys. Rev. E* **60**, 3439.
- Bateman, J. E., 1977, *Nucl. Instrum. Methods* **144**, 537.
- Beg, F. N., A. R. Bell, A. E. Dangor, C. N. Danson, A. P. Fews, M. E. Glinsky, B. A. Hammel, P. Lee, P. A. Norreys, and M. Tatarakis, 1997, *Phys. Plasmas* **4**, 447.
- Beiersdorfer, P., G. V. Brown, R. Goddard, and B. J. Wargelin, 2004, *Rev. Sci. Instrum.* **75**, 3720.
- Beiersdorfer, P., J. R. C. Lopez-Urrutia, P. Springer, S. B. Utter, and K. L. Wong, 1999, *Rev. Sci. Instrum.* **70**, 276.
- Bethe, H. A., and A. H. Guth, 1994, *O. Klein and Y. Nishina, On the Scattering of Radiation by Free Electrons According to Dirac's New Relativistic Quantum Dynamics* (World Scientific, Singapore).
- Beule, D., W. Ebeling, A. Förster, H. Juranek, R. Redmer, and G. Röpke, 1999, *Contrib. Plasma Phys.* **39**, 21.
- Beule, D., W. Ebeling, A. Förster, H. Juranek, R. Redmer, and G. Röpke, 2001, *Phys. Rev. E* **63**, 060202.
- Blue, B. E., *et al.*, 2005, *Phys. Rev. Lett.* **94**, 095005.
- Boehly, T., *et al.*, 1997, *Opt. Commun.* **133**, 495.
- Bohm, D., and E. P. Gross, 1949, *Phys. Rev.* **75**, 1851.
- Bohm, D., and D. Pines, 1953, *Phys. Rev.* **92**, 609.
- Bonev, S. A., B. Militzer, and G. Galli, 2004, *Phys. Rev. B* **69**, 014101.
- Bonev, S. A., E. Schwegler, T. Ogitsu, and G. Galli, 2004, *Nature (London)* **431**, 669.
- Cavailler, C., 2005, *Comments Plasma Phys. Controlled Fusion* **47**, B389.
- Chandrasekhar, S., 1929, *Proc. R. Soc. London, Ser. A* **125**, 231.
- Chen, H., *et al.*, 2007, *Phys. Rev. E* **76**, 056402.
- Chihara, J., 1987, *J. Phys. F: Met. Phys.* **17**, 295.
- Chihara, J., 2000, *J. Phys.: Condens. Matter* **12**, 231.
- Chung, H. K., W. L. Morgan, and R. W. Lee, 2003, *J. Quant. Spectrosc. Radiat. Transf.* **81**, 107.
- Collins, G. W., L. B. Da Silva, P. Celliers, D. M. Gold, M. E. Foord, R. J. Wallace, A. Ng, S. V. Weber, K. S. Budil, and R. Cauble, 1998, *Science* **281**, 1178.
- Compton, A. H., 1923, *Phys. Rev.* **21**, 483.
- Constantin, C., C. A. Back, K. B. Fournier, G. Gregori, O. L. Landen, S. H. Glenzer, E. L. Dewald, and M. C. Miller, 2005, *Phys. Plasmas* **12**, 063104.
- Desjarlais, M. P., 2000, *Contrib. Plasma Phys.* **41**, 267.
- Desjarlais, M. P., J. D. Kress, and L. A. Collins, 2002, *Phys. Rev. E* **66**, 025401.
- Deutsch, C., 1977, *Phys. Lett.* **60A**, 317.
- Dewald, E. L., *et al.*, 2005, *Comments Plasma Phys. Controlled Fusion* **47**, B405.
- Dharma-wardana, M. W. C., and F. Perrot, 2000, *Phys. Rev. Lett.* **84**, 959.
- Dixit, S., M. Feit, M. Perry, and H. Powell, 1996, *Opt. Lett.* **21**, 1715.
- Döppner, T., O. L. Landen, H. J. Lee, P. Neumayer, S. P. Regan, and S. H. Glenzer, 2009, *High Energy Density Phys.* **5**, 182.
- Döppner, T., P. Neumayer, F. Girard, N. L. Kugland, O. L. Landen, C. Niemann, and S. H. Glenzer, 2008, *Rev. Sci. Instrum.* **79**, 10E311.
- Dougherty, J. P., and D. T. Farley, 1960, *Proc. R. Soc. London, Ser. A* **259**, 79.
- Drake, R. P., 2006, *High-Energy-Density Physics* (Springer, Berlin).
- Drude, P., 1890, *Ann. Phys.* **39**, 504.
- Du Mond, J. W. M., 1929, *Phys. Rev.* **33**, 643.
- Edwards, J., *et al.*, 2000, *Phys. Plasmas* **7**, 2099.
- Eisenberger, P., and P. M. Platzman, 1970, *Phys. Rev. A* **2**, 415.
- Evans, D. E., and J. Katzenstein, 1969, *Rep. Prog. Phys.* **32**, 207.
- Eyharts, P., J. M. Di-Nicola, C. Feral, E. Germain, H. Graillet, F. Jequier, E. Journot, X. Julien, M. Luttmann, O. Lutz, and G. Thiell, 2006, *J. Phys. I* **133**, 727.
- Fejer, J. A., 1960, *Can. J. Phys.* **38**, 1114.
- Fortmann, C., R. Redmer, H. Reinholz, G. Röpke, A. Wierling, and W. Rozmus, 2006, *High Energy Density Phys.* **2**, 57.
- Fortov, V. E., R. I. Ilkaev, V. A. Arinin, V. V. Burtzev, V. A. Golubev, I. L. Iosilevskiy, V. V. Khurstalev, A. L. Mikhailov, M. A. Mochalov, V. Y. Ternovoi, and M. V. Zhernokletov, 2007, *Phys. Rev. Lett.* **99**, 185001.
- Fournier, K., C. Constantin, C. Back, L. Suter, H. Chung, M. Miller, D. Froula, G. Gregori, S. Glenzer, E. Dewald, and O. Landen, 2006, *J. Quant. Spectrosc. Radiat. Transf.* **99**, 186.
- Fournier, K. B., C. Constantin, J. Poco, M. C. Miller, C. A. Back, L. J. Suter, J. Satcher, J. Davis, and J. Grun, 2004, *Phys. Rev. Lett.* **92**, 165005.
- Froula, D. H., L. Divol, and S. H. Glenzer, 2002, *Phys. Rev. Lett.* **88**, 105003.
- Funfer, E., B. Kronast, and H. J. Kunze, 1963, *Phys. Lett.* **5**, 125.
- Garcia Saiz, E., G. Gregori, G. O. Gericke, J. Vorberger, B. Barbrel, R. Clarke, R. R. Freeman, S. H. Glenzer, F. Y. Khatkhat, M. Koenig, O. L. Landen, D. Neely, P. Neumayer, M. M. Motley, A. Pelka, D. Price, M. Roth, M. Schollmeier, C. Spindloe, R. L. Weber, L. Van Woerkom, J. Kohanoff, K. Wünsch, and D. Riley, 2008, *Nat. Phys.* **4**, 940.

- Garcia Saiz, E., G. Gregori, F. Y. Khattak, J. Kohanoff, S. Sahoo, G. Shabbir Naz, S. Bandyopadhyay, M. Notley, R. L. Weber, and D. Riley, 2008, *Phys. Rev. Lett.* **101**, 075003.
- Garcia Saiz, E., F. Y. Khattak, G. Gregori, S. Bandyopadhyay, R. J. Clarke, B. Fell, R. R. Freeman, J. Jeffries, D. Jung, M. M. Notley, R. L. Weber, L. van Woerkom, and D. Riley, 2007, *Rev. Sci. Instrum.* **78**, 09519.
- Girard, F., J. P. Jadaud, M. Naudy, B. Villette, D. Babonneau, M. Primout, M. C. Miller, R. L. Kauffman, L. J. Suter, J. Grun, and J. Davis, 2005, *Phys. Plasmas* **12**, 092705.
- Glenzer, S. H., W. E. Alley, K. G. Estabrook, J. S. De Groot, M. G. Haines, J. H. Hammer, J. P. Jadaud, B. J. MacGowan, J. D. Moody, W. Rozmus, L. J. Suter, T. L. Weiland, and E. A. Williams, 1999, *Phys. Plasmas* **6**, 2117.
- Glenzer, S. H., C. A. Back, K. G. Estabrook, B. J. MacGowan, D. S. Montgomery, R. K. Kirkwood, J. D. Moody, D. H. Munro, and G. F. Stone, 1997, *Phys. Rev. E* **55**, 927.
- Glenzer, S. H., D. H. Froula, L. Divol, M. R. Dorr, R. L. Berger, S. Dixit, B. A. Hammel, C. Haynam, J. A. Hittinger, J. P. Holder, O. S. Jones, D. H. Kalantar, O. L. Landen, A. B. Langdon, S. Langer, B. J. MacGowan, A. J. Mackinnon, N. Meezan, E. I. Moses, C. Niemaan, C. H. Still, L. J. Suter, R. J. Wallace, E. A. Williams, and B. K. F. Young, 2007, *Nat. Phys.* **3**, 716.
- Glenzer, S. H., G. Gregori, R. W. Lee, F. J. Rogers, S. W. Pollaine, and O. L. Landen, 2003, *Phys. Rev. Lett.* **90**, 175002.
- Glenzer, S. H., G. Gregori, F. J. Rogers, D. H. Froula, S. W. Pollaine, R. S. Wallace, and O. L. Landen, 2003, *Phys. Plasmas* **10**, 2433.
- Glenzer, S. H., O. L. Landen, P. Neumayer, R. W. Lee, K. Widmann, S. W. Pollaine, R. J. Wallace, G. Gregori, A. Höll, T. Bornath, R. Thiele, V. Schwarz, W.-D. Kraeft, and A. Redmer, 2007, *Phys. Rev. Lett.* **98**, 065002.
- Glenzer, S. H., W. Rozmus, B. J. MacGowan, K. G. Estabrook, J. D. De Groot, G. B. Zimmerman, H. A. Baldis, J. A. Harte, R. W. Lee, E. A. Williams, and B. G. Wilson, 1999, *Phys. Rev. Lett.* **82**, 97.
- Glenzer, S. H., *et al.*, 2004, *Nucl. Fusion* **44**, S185.
- Gregori, G., S. Glenzer, H. Chung, D. Froula, R. Lee, N. Meezan, J. Moody, C. Niemann, O. Landen, B. Holst, R. Redmer, S. Regan, and H. Sawada, 2006, *J. Quant. Spectrosc. Radiat. Transf.* **99**, 225.
- Gregori, G., S. H. Glenzer, K. B. Fournier, K. M. Campbell, E. L. Dewald, O. S. Jones, J. H. Hammer, S. B. Hansen, R. J. Wallace, and O. L. Landen, 2008, *Phys. Rev. Lett.* **101**, 045003.
- Gregori, G., S. H. Glenzer, and O. L. Landen, 2003, *J. Phys. A* **36**, 5971.
- Gregori, G., S. H. Glenzer, and O. L. Landen, 2006, *Phys. Rev. E* **74**, 026402.
- Gregori, G., S. H. Glenzer, F. J. Rogers, S. M. Pollaine, O. L. Landen, C. Blancard, G. Faussurier, P. Renaudin, S. Kuhlbrodt, and R. Redmer, 2004, *Phys. Plasmas* **11**, 2754.
- Gregori, G., S. H. Glenzer, W. Rozmus, R. W. Lee, and O. L. Landen, 2003, *Phys. Rev. E* **67**, 026412.
- Gregori, G., R. Tommasini, O. L. Landen, R. W. Lee, and S. H. Glenzer, 2006, *EPL* **74**, 637.
- Griem, H. R., 1997, *Principles of Plasma Spectroscopy*, Cambridge Monographs on Plasma Physics (Cambridge University Press, Cambridge).
- Haas, F., G. Manfredi, and M. Feix, 2000, *Phys. Rev. E* **62**, 2763.
- Hammel, B. A., D. Griswold, O. L. Landen, T. S. Perry, B. A. Remington, P. L. Miller, T. A. Peyser, and J. D. Kilkenny, 1993, *Phys. Fluids B* **5**, 2259.
- Hansen, J.-P., and I. R. McDonald, 2006, *Theory of Simple Liquids*, 3rd ed. (Elsevier, Amsterdam).
- Harada, T., K. Takahashi, H. Sakuma, and A. Osyczka, 1999, *Appl. Opt.* **38**, 2743.
- Hatchett, S. P., 2008, private communication.
- Henke, B. L., E. M. Gullikson, and J. C. Davis, 1993, *At. Data Nucl. Data Tables* **54**, 181.
- Henke, B. L., P. Lee, T. J. Tanaka, R. L. Shimabukuro, and B. K. Fujikawa, 1982, *Ann. Phys. (N.Y.)* **27**, 3.
- Höll, A., R. Redmer, G. Röpke, and H. Reinholz, 2004, *Eur. Phys. J. D* **29**, 159.
- Höll, A., *et al.*, 2007, *High Energy Density Phys.* **3**, 120.
- Holm, P., and R. Ribberfors, 1989, *Phys. Rev. A* **40**, 6251.
- Hubbard, J., 1958, *Proc. R. Soc. London, Ser. A* **243**, 336.
- Ice, G. E., and C. J. Sparks, 1990, *Nucl. Instrum. Methods Phys. Res. A* **291**, 110.
- Ichimaru, S., 1973, *Basic Principles of Plasma Physics* (Addison, Reading, MA).
- Ichimaru, S., 1994, *Statistical Plasma Physics* (Addison, New York).
- Ichimaru, S., H. Iyetomi, and K. Utsumi, 1982, *Phys. Rev. B* **25**, 1374.
- Ichimaru, S., S. Tanaka, and H. Iyetomi, 1984, *Phys. Rev. A* **29**, 2033.
- Issolah, A., Y. Garreau, B. Levy, and G. Louprias, 1991, *Phys. Rev. B* **44**, 11029.
- Izumi, N., 2008, private communication.
- Izumi, N., R. Snavely, G. Gregori, J. A. Koch, H. S. Park, and B. A. Remington, 2006, *Rev. Sci. Instrum.* **77**, 10E325.
- James, R. W., 1962, *The Optical Properties of Diffraction of X-Rays* (Ox Bow, Woodbridge, CT).
- Jasny, J., U. Teubner, W. Theobald, C. Wulker, J. Bergmann, and F. P. Schafer, 1994, *Rev. Sci. Instrum.* **65**, 1631.
- Jiang, Z., J. C. Kieffer, J. P. Matte, M. Chaker, O. Peyrusse, D. Gilles, G. Korn, A. Maksimchuk, S. Coe, and G. Mourou, 1995, *Phys. Plasmas* **2**, 1702.
- Kauffman, R. L., 1991, in *Handbook of Plasma Physics*, edited by A. Rubenchik and S. Witkowski (Elsevier, Amsterdam), Vol. 3, p. 111.
- Khattak, F. Y., O. A. M. B. P. du Sert, D. Riley, P. S. Foster, E. J. Divall, C. J. Hooker, A. J. Langley, J. Smith, and P. Gibson, 2006, *Phys. Rev. E* **74**, 027401.
- Klimontovich, Y. L., and W.-D. Kraeft, 1974, *High Temp.* **12**, 212.
- Klisnick, A., *et al.*, 2006, *J. Quant. Spectrosc. Radiat. Transf.* **99**, 370.
- Kodama, R., K. Okada, N. Ikeda, M. Mineo, K. A. Tanaka, T. Mochizuki, and C. Yamanaka, 1986, *J. Appl. Phys.* **59**, 3050.
- Kodama, R., *et al.*, 2001, *Nature (London)* **412**, 798.
- Kohn, W., and L. J. Sham, 1965, *Phys. Rev.* **140**, A1133.
- Kremp, D., M. Schlanges, and W.-D. Kraeft, 2005, *Quantum Statistics of Nonideal Plasmas* (Springer, Berlin).
- Kritcher, A. L., P. Neumayer, J. Castor, T. Döppner, R. W. Falcone, O. L. Landen, H. J. Lee, R. W. Lee, B. Holst, R. Redmer, E. C. Morse, A. Ng, S. W. Pollaine, D. Price, and S. H. Glenzer, 2009, *Phys. Plasmas* **16**, 056308.
- Kritcher, A. L., P. Neumayer, J. Castor, T. Döppner, R. W. Falcone, O. L. Landen, H. J. Lee, R. W. Lee, E. C. Morse, A. Ng, S. W. Pollaine, D. Price, and S. H. Glenzer, 2008, *Science* **322**, 69.
- Kritcher, A. L., P. Neumayer, H. J. Lee, T. Döppner, R. W.

- Falcone, S. H. Glenzer, and E. C. Morse, 2008, *Rev. Sci. Instrum.* **79**, 10E739.
- Kritcher, A. L., P. Neumayer, M. K. Urry, H. Robey, C. Niemann, O. L. Landen, E. Morse, and S. H. Glenzer, 2007, *High Energy Density Phys.* **3**, 156.
- Kubo, R., 1966, *Rep. Prog. Phys.* **29**, 255.
- Kugland, N. L., C. G. Constantin, P. Neumayer, H. K. Chung, A. Collette, E. L. Dewald, D. H. Froula, S. H. Glenzer, A. Kemp, A. L. Kritcher, J. S. Ross, and C. Niemann, 2008, *Appl. Phys. Lett.* **92**, 241504.
- Kuhlbrodt, S., B. Holst, and R. Redmer, 2005, *Contrib. Plasma Phys.* **45**, 73.
- Kulcsar, G., D. AlMawlawi, F. W. Budnik, P. R. Herman, M. Moskovits, L. Zhao, and R. S. Marjoribanks, 2000, *Phys. Rev. Lett.* **84**, 5149.
- Kunze, H.-J., 1968, *The Laser as a Tool for Plasma Diagnostics* (North-Holland, Amsterdam).
- Kunze, H. J., E. Funfer, B. Kronast, and W. H. Kegel, 1964, *Phys. Lett.* **11**, 42.
- Kyrala, G. A., R. D. Fulton, E. K. Wahlin, L. A. Jones, G. T. Schappert, J. A. Cobble, and A. J. Taylor, 1992, *Appl. Phys. Lett.* **60**, 2195.
- Kyrala, G. A., and J. B. Workman, 2001, *Rev. Sci. Instrum.* **72**, 682.
- Landen, O. L., D. R. Farley, S. G. Glendinning, L. M. Logory, P. M. Bell, J. A. Koch, F. D. Lee, D. K. Bradley, D. H. Kalantar, C. A. Back, and R. E. Turner, 2001, *Rev. Sci. Instrum.* **72**, 627.
- Landen, O. L., S. H. Glenzer, M. J. Edwards, R. W. Lee, G. W. Collins, R. C. Cauble, W. W. Hsing, and B. A. Hammel, 2001, *J. Quant. Spectrosc. Radiat. Transf.* **71**, 465.
- Landen, O. L., A. Lobban, T. Tutt, P. M. Bell, R. Costa, D. R. Hargrove, and F. Ze, 2001, *Rev. Sci. Instrum.* **72**, 709.
- Landen, O. L., *et al.*, 2006, *J. Phys. IV* **133**, 43.
- Lee, H. J., P. Neumayer, J. Castor, T. Döppner, R. W. Falcone, C. Fortmann, B. A. Hammel, A. L. Kritcher, O. L. Landen, R. W. Lee, D. D. Meyerhofer, D. H. Munro, R. Redmer, S. P. Regan, S. Weber, and S. H. Glenzer, 2009, *Phys. Rev. Lett.* **102**, 115001.
- Lee, R. W., *et al.*, 2003, *J. Opt. Soc. Am. B* **20**, 770.
- Lindl, J. D., P. Amendt, R. L. Berger, S. G. Glendinning, S. H. Glenzer, S. W. Haan, R. L. Kauffman, O. L. Landen, and L. J. Suter, 2004, *Phys. Plasmas* **11**, 339.
- Lowney, D. P., P. A. Heimann, H. A. Padmore, E. M. Gullikson, A. G. MacPhee, and R. W. Falcone, 2004, *Rev. Sci. Instrum.* **75**, 3131.
- MacFarlane, J. J., I. E. Golovkin, and P. R. Woodruff, 2006, *J. Quant. Spectrosc. Radiat. Transf.* **99**, 381.
- MacGowan, B., *et al.*, 1996, *Phys. Plasmas* **3**, 2029.
- Maiman, T. H., 1960, *Nature (London)* **187**, 493.
- Marshall, F. J., and J. A. Oertel, 1997, *Rev. Sci. Instrum.* **68**, 735.
- Matthews, D. L., E. M. Campbell, N. M. Ceglie, G. Hermes, R. Kauffman, L. Koppel, R. Lee, K. Manes, V. Rupert, V. W. Slivinsky, R. Turner, and F. Ze, 1983, *J. Appl. Phys.* **54**, 4260.
- Matzen, M. K., *et al.*, 2005, *Phys. Plasmas* **12**, 055503.
- Meadowcroft, A. L., C. D. Bentley, and E. N. Stott, 2008, *Rev. Sci. Instrum.* **79**, 113102.
- Mermin, N. D., 1970, *Phys. Rev. B* **1**, 2362.
- Mima, K., *et al.*, 2007, *Eur. Phys. J. D* **44**, 259.
- Molitoris, J. D., M. M. Morin, D. W. Phillion, A. L. Osterheld, R. E. Stewart, and S. D. Rothman, 1992, *Rev. Sci. Instrum.* **63**, 5104.
- Montgomery, D. S., R. J. Focia, H. A. Rose, D. A. Russell, J. A. Cobble, J. C. Fernández, and R. P. Johnson, 2001, *Phys. Rev. Lett.* **87**, 155001.
- Morozov, I., H. Reinholz, G. Röpke, A. Wierling, and G. Zwicknagel, 2005, *Phys. Rev. E* **71**, 066408.
- Moses, E. I., and C. R. Wuest, 2005, *Fusion Sci. Technol.* **47**, 314.
- Nakano, N., H. Kuroda, T. Kita, and T. Harada, 1984, *Appl. Opt.* **23**, 2386.
- Neumayer, P., 2008, private communication.
- Neumayer, P., *et al.*, 2005, *Laser Part. Beams* **23**, 385.
- Niemann, C., S. H. Glenzer, J. Knight, L. Divol, E. A. Williams, G. Gregori, B. I. Cohen, C. Constantin, D. H. Froula, D. S. Montgomery, and R. P. Johnson, 2004, *Phys. Rev. Lett.* **93**, 045004.
- Pak, A., G. Gregori, J. Knight, K. Campbell, D. Price, B. Hammel, O. L. Landen, and S. H. Glenzer, 2004, *Rev. Sci. Instrum.* **75**, 3747.
- Park, H. S., N. Izumi, M. H. Key, J. A. Koch, O. L. Landen, P. K. Patel, T. W. Phillips, and B. B. Zhang, 2004, *Rev. Sci. Instrum.* **75**, 4048.
- Park, H. S., *et al.*, 2006, *Phys. Plasmas* **13**, 056309.
- Pauling, L., and J. Sherman, 1932, *Z. Kristallogr.* **81**, 1.
- Peacock, N. J., D. C. Robinson, M. J. Forrest, P. D. Wilcock, and V. V. Sannikov, 1969, *Nature (London)* **224**, 488.
- Peyrusse, O., 1990, *J. Quant. Spectrosc. Radiat. Transf.* **43**, 397.
- Phillion, D. W., and C. J. Hailey, 1986, *Phys. Rev. A* **34**, 4886.
- Pines, D., and D. Bohm, 1952, *Phys. Rev.* **85**, 338.
- Pines, D., and P. Nozieres, 1990, *The Theory of Quantum Fluids* (Addison-Wesley, Redwood City, CA).
- Rambo, P. K., *et al.*, 2005, *Appl. Opt.* **44**, 2421.
- Ravasio, A., G. Gregori, A. Benuzzi-Mounaix, J. Daligault, A. Delserieys, A. Y. Faenov, B. Loupias, N. Ozaki, M. R. le Gloahec, T. A. Pikuz, D. Riley, and M. Koenig, 2007, *Phys. Rev. Lett.* **99**, 135006.
- Redmer, R., H. Juranek, S. Kuhlbrodt, and V. Schwarz, 2003, *Z. Phys. Chem.* **217**, 783.
- Redmer, R., H. Reinholz, G. Röpke, R. Thiele, and A. Höll, 2005, *IEEE Trans. Plasma Sci.* **33**, 77.
- Redmer, R., G. Röpke, F. Morales, and K. Kilimann, 1990, *Phys. Fluids B* **2**, 390.
- Reich, C., I. Uschmann, F. Ewald, S. Düsterer, A. Lübcke, H. Schwoerer, R. Sauerbrey, E. Förster, and P. Gibbon, 2003, *Phys. Rev. E* **68**, 056408.
- Reinholz, H., 2005, *Ann. Phys. (Paris)* **30**, 1.
- Reinholz, H., R. Redmer, G. Röpke, and A. Wierling, 2000, *Phys. Rev. E* **62**, 5648.
- Remington, B., R. P. Drake, and D. Ryutov, 2006, *Rev. Mod. Phys.* **78**, 755.
- Renau, J., 1960, *J. Geophys. Res.* **65**, 3631.
- Renaudin, P., C. Blancard, G. Faussurier, and P. Noiret, 2002, *Phys. Rev. Lett.* **88**, 215001.
- Riley, D., J. J. Angulo-Gareta, F. Y. Khattak, M. J. Lamb, P. S. Foster, E. J. Divall, C. J. Hooker, A. J. Langley, R. J. Clarke, and D. Neely, 2005, *Phys. Rev. E* **71**, 016406.
- Riley, D., F. Y. Khattak, E. G. Saiz, G. Gregori, S. Bandyopadhyay, M. Notley, D. Neely, D. Chambers, A. Moore, and A. Comley, 2007, *Laser Part. Beams* **25**, 465.
- Riley, D., I. Weaver, D. McSherry, M. Dunne, D. Neely, M. Notley, and E. Nardi, 2002, *Phys. Rev. E* **66**, 046408.
- Riley, D., N. C. Woolsey, D. McSherry, F. Y. Khattak, and I. Weaver, 2002, *Plasma Sources Sci. Technol.* **11**, 484.
- Riley, D., N. C. Woolsey, D. McSherry, I. Weaver, A. Djaoui,

- and E. Nardi, 2000, Phys. Rev. Lett. **84**, 1704.
- Rogers, F. J., 2000, Phys. Plasmas **7**, 51.
- Rogers, F. J., H. C. Graboske, and D. J. Harwood, 1970, Phys. Rev. A **1**, 1577.
- Rogers, F. J., and D. A. Young, 1997, Phys. Rev. E **56**, 5876.
- Röpke, G., 1998, Phys. Rev. E **57**, 4673.
- Röpke, G., and R. Der, 1979, Phys. Status Solidi B **92**, 501.
- Röpke, G., A. Selchow, A. Wierling, and H. Reinholz, 1999, Phys. Lett. A **260**, 365.
- Röpke, G., and A. Wierling, 1998, Phys. Rev. E **57**, 7075.
- Rousse, A., P. Audebert, J. P. Geindre, F. Fallies, J. C. Gauthier, A. Mysyrowicz, G. Grillon, and A. Antonetti, 1994, Phys. Rev. E **50**, 2200.
- Ruggles, L. E., J. L. Porter, P. K. Rambo, W. W. Simpson, M. F. Vargas, G. R. Bennett, and I. C. Smith, 2003, Rev. Sci. Instrum. **74**, 2206.
- Rus, B., *et al.*, 2007, J. Mod. Opt. **54**, 2571.
- Salpeter, E. E., 1960, Phys. Rev. **120**, 1528.
- Salzmann, D., C. Reich, I. Uschmann, E. Forster, and P. Gibbon, 2002, Phys. Rev. E **65**, 036402.
- Sawada, H., *et al.*, 2007, Phys. Plasmas **14**, 122703.
- Schnurer, M., P. V. Nickles, M. P. Kalachnikov, W. Sandner, R. Nolte, P. Ambrosi, J. L. Miquel, A. Dulieu, and A. Jolas, 1996, J. Appl. Phys. **80**, 5604.
- Schülke, W., 1991, *Handbook on Synchrotron Radiation* (Elsevier, Amsterdam), Vol. 3.
- Schumacher, M., F. Smend, and I. Borchert, 1975, J. Phys. B **8**, 1428.
- Schwarz, V., T. Bornath, W. D. Kraeft, S. H. Glenzer, A. Höll, and R. Redmer, 2007, Contrib. Plasma Phys. **47**, 324.
- Seidel, J., S. Arndt, and W. D. Kraeft, 1995, Phys. Rev. E **52**, 5387.
- Selchow, A., G. Röpke, and A. Wierling, 2002, Contrib. Plasma Phys. **42**, 43.
- Selchow, A., G. Röpke, A. Wierling, H. Reinholz, T. Pschiwul, and G. Zwicknagel, 2001, Phys. Rev. E **64**, 056410.
- Sheffield, J., 1975, *Plasma Scattering of Electromagnetic Radiation* (Academic, New York).
- Singwi, K. S., M. P. Tosi, R. H. Land, and A. Sjölander, 1968, Phys. Rev. **176**, 589.
- Sinn, H., and E. Burkel, 1996, J. Phys.: Condens. Matter **8**, 9369.
- Snavely, R. A., *et al.*, 2007, Phys. Plasmas **14**, 092703.
- Soures, J. M., *et al.*, 1993, Laser Part. Beams **11**, 317.
- Stewart, J. C., and K. D. Pyatt, 1966, Astrophys. J. **144**, 1203.
- Stoeckl, C., *et al.*, 2006, Fusion Sci. Technol. **49**, 367.
- Strickland, D., and G. Mourou, 1985, Opt. Commun. **56**, 219.
- Tallents, G. J., M. H. Key, A. Ridgeley, W. Shaikh, C. L. S. Lewis, D. O'Neill, S. J. Davidson, N. J. Freeman, and D. Perkins, 1990, J. Quant. Spectrosc. Radiat. Transf. **43**, 53.
- Tauschwitz, A., J. A. Maruhn, D. Riley, G. Shabbir Naz, F. B. Rosmej, S. Borneis, and A. Tauschwitz, 2007, Ward's Auto World **3**, 371.
- Tertian, R., and F. Claisse, 1982, *Principles of Quantitative X-ray Fluorescence Analysis* (Heyden, Philadelphia).
- Thiele, R. T., Bornath, F. C., A. Höll, R. Redmer, H. Reinholz, G. Röpke, A. Wierling, S. H. Glenzer, and G. Gregori, 2008, Phys. Rev. E (to be published).
- Thiele, R., R. Redmer, H. Reinholz, and G. Röpke, 2006, J. Phys. A **39**, 4365.
- Thomson, J. J., 1906, *Conductivity of Electricity through Gases* (Cambridge University Press, Cambridge).
- Tillman, C., S. A. Johansson, B. Erlandsson, M. Gratz, B. Hemdal, A. Almen, S. Mattsson, and S. Svanberg, 1997, Nucl. Instrum. Methods Phys. Res. A **394**, 387.
- Tonks, L., and I. Langmuir, 1929, Phys. Rev. **33**, 195.
- Tschentscher, T., and S. Toleikis, 2005, Eur. Phys. J. D **36**, 193.
- Urry, M. K., G. Gregori, O. L. Landen, A. Pak, and S. H. Glenzer, 2006, J. Quant. Spectrosc. Radiat. Transf. **99**, 636.
- van Woerkom, L., K. Akli, T. Bartal, F. N. Beg, and S. Chawla, 2008, unpublished.
- Wang, Y., R. Ahuja, and B. Johansson, 2003, Phys. Status Solidi B **235**, 470.
- Wharton, K. B., S. P. Hatchett, S. C. Wilks, M. H. Key, J. D. Moody, V. Yanovsky, A. A. Offenberger, B. A. Hammel, M. D. Perry, and C. Joshi, 1998, Phys. Rev. Lett. **81**, 822.
- Wolf, E., 1987, Nature (London) **326**, 363.
- Workman, J., and G. A. Kyrala, 2001, Rev. Sci. Instrum. **72**, 678.
- Wünsch, K., P. Hilse, M. Schlanges, and D. O. Gericke, 2008, Phys. Rev. E **77**, 056404.
- Wünsch, K., J. Vorberger, and D. O. Gericke, 2009, Phys. Rev. E **79**, 010201.
- Yaakobi, B., P. Bourke, Y. Conturie, J. Delettrez, J. M. Forsyth, R. D. Frankel, L. M. Goldman, R. L. Mccrory, W. Seka, J. M. Soures, A. J. Burek, and R. E. Deslattes, 1981, Opt. Commun. **38**, 196.
- Yaakobi, B., and A. J. Burek, 1983, IEEE J. Quantum Electron. **19**, 1841.
- Yasuike, K., M. H. Key, S. P. Hatchett, R. A. Snavely, and K. B. Wharton, 2001, Rev. Sci. Instrum. **72**, 1236.
- Young, D. A., and E. M. Corey, 1995, J. Appl. Phys. **78**, 3748.
- Yu, W., C. Q. Jin, and A. Kohlmeier, 2007, J. Phys.: Condens. Matter **19**, 086209.
- Zanella, G., 2002, Nucl. Instrum. Methods Phys. Res. A **481**, 691.
- Ziener, C., I. Uschmann, G. Stobrawa, C. Reich, P. Gibbon, T. Feurer, A. Morak, S. Düsterer, H. Schwoerer, E. Förster, and R. Sauerbrey, 2002, Phys. Rev. E **65**, 066411.
- Zimmerman, R., 1987, *Many-Particle Theory of Highly Excited Semiconductors* (Teubner, Leipzig).
- Zimmermann, R., K. Kilimann, W. D. Kraeft, D. Kremp, and G. Röpke, 1978, Phys. Status Solidi B **90**, 175.
- Zimmerman, G. B., and W. L. Kruer, 1975, Comments Plasma Phys. Controlled Fusion **2**, 51.
- Zwicknagel, G., C. Toepffer, and P. G. Reinhard, 1999, Phys. Rep., Phys. Lett. **309**, 117.